

ABSTRACT

ACHARYA, PINAKI. Temperature Abatement using Spray Injection in Liquid Piston Compressors for Ocean Compressed Air Energy Storage Systems. (Under the direction of Dr. Paul I. Ro).

The objective of this thesis is to analyze the effect of spray cooling in a liquid piston compressor during the compression of air. A liquid piston compressor can be used in the application of Ocean Compressed Air Energy Storage Systems (OCAES). The liquid piston can effectively cover any irregular containers making its surface area to volume ratio better than conventional reciprocating pistons. This plays a key role in increased heat transfer to the outer surface resulting in improved efficiency. As the compression process has the minimum work input during an isothermal compression, the process path needs to shift from the polytropic curve towards the isothermal curve for higher efficiency. Recently, various methodologies have been tested in the liquid piston for increasing heat transfer from the chamber such as optimal compression trajectories, placing porous media inserts into the chamber, and introducing hollow spheres in the chamber. Also, several studies have presented spray cooling as a practical option for heat transfer enhancement in compressors due to its high specific heat and fine atomization. In this study, to shift the compression trajectory towards an isothermal curve, spray cooling is investigated for a compression ratio of 2.5 in a liquid piston compressor.

Experiments are performed in the liquid piston setup with water as the medium and a plastic chamber for a compression ratio set at 2.5. A low-flow full cone nozzle was used for the experiments with different experimental parameters such as nozzle spray angle and spray injection pressure which are studied for compression stroke times. With the injection of spray during the compression process, the temperature of air dropped around 10-15 K compared to compression without spray injection. Higher injection pressures result in a greater temperature drop because of

higher mass loading and finer droplet diameters, however higher injection pressures also need a higher pump work. The polytropic index of compression changed approximately from 1.20 - 1.25 without spray injection to 1.03 – 1.05 when spray cooling was introduced. This corresponded to a 9 – 20 % improvement in the compression efficiency. By incorporating water spray injection, the compression efficiency of the liquid piston compressor improved significantly.

Further, numerical simulations of a liquid piston compressor are performed in a 2D and 3D computational domain to characterize the flow-field during the compression process. The numerical simulations are performed on ANSYS Fluent. For liquid piston compression, the numerical simulations matched reasonably well with the experimental results. Numerical simulations for spray injection in a liquid piston compressor were also performed to observe the droplets characteristics during the process. The droplet distribution plays a significant role in the simulations as the droplet diameter characterizes the spray parameters. The temperature drop with spray injection was observed to have temperature profiles similar to the experimental observations. Overall, spray cooling proved to be an effective heat transfer mechanism for improving the compression efficiency of the liquid piston compressor.

© Copyright 2018 by Pinaki Acharya

All Rights Reserved

Temperature Abatement using Spray Injection in Liquid Piston Compressors for Ocean
Compressed Air Energy Storage Systems.

by
Pinaki Acharya

A thesis submitted to the Graduate Faculty of
North Carolina State University
in partial fulfillment of the
requirements for the degree of
Master of Science

Mechanical Engineering

Raleigh, North Carolina

2018

APPROVED BY:

Dr. Alexei Saveliev

Dr. Stephen D. Terry

Dr. Paul I. Ro
Committee Chair

DEDICATION

To my family for their unconditional love and support

And

In memory of Ayush Agrawal

BIOGRAPHY

Pinaki Acharya was born on November 19th, 1993 to Dr. Shankar Acharya and Dr. Anita Acharya. He graduated with a Bachelor's degree in Mechanical Engineering from Birla Institute of Technology and Science - Pilani in 2016. He moved to Raleigh, NC in the fall of 2016 to pursue his Master's at North Carolina State University.

ACKNOWLEDGMENTS

I would like to take this opportunity to express my deepest gratitude to my advisor Dr. Paul I. Ro, for his continuous guidance and support during my thesis. I am grateful for his constant encouragement and for providing me the opportunity to present my work at various platforms.

I would also like to thank Dr. Alexei Saveliev and Dr. Stephen Terry for their support and for being a part of my thesis committee.

I am thankful to Vikram Patil, my lab mate for his wonderful suggestions and help in running the experiments. I also sincerely appreciate Sriram, Kishore, Abhimanyu, and Rishabh for their assistance in the numerical simulations.

Special thanks to my friends Ayaan, Saurabh, Saif, Adithya, Nikhil, Joy, and Ayush for making this place feel like home away from home, for teaching me about enjoying life and making these two years memorable, and most importantly for their comradery and lively banter.

Last but not least, I am eternally grateful to my parents and my brother for their love and support and for always being there for me.

TABLE OF CONTENTS

| | |
|---|------|
| LIST OF TABLES | vii |
| LIST OF FIGURES | viii |
| | |
| CHAPTER 1: Introduction | 1 |
| 1.1 Compressors | 7 |
| 1.2 Liquid Piston Compressor | 9 |
| 1.3 Heat Transfer Enhancement Techniques | 10 |
| CHAPTER 2: Liquid Piston Compression with Spray Injection..... | 14 |
| CHAPTER 3: Experimental Setup..... | 24 |
| 3.1 Liquid Piston Compressor Setup | 24 |
| 3.2 Spray Injection Setup..... | 26 |
| 3.3 Measurement Equipment..... | 28 |
| 3.4 Range of Experiments | 31 |
| 3.5 Results | 32 |
| 3.5.1 Effect of Injection Pressure | 32 |
| 3.5.2 Effect of Stroke Time of Compression..... | 45 |
| 3.5.3 Effect of Spray Angle | 47 |
| CHAPTER 4: Numerical Simulations | 52 |
| 4.1 2D Simulation Setup..... | 53 |
| 4.2 3D Simulation Setup..... | 57 |
| CHAPTER 5: CFD Validation and Results | 62 |
| 5.1 Liquid Piston Compression-Numerical Validation | 62 |
| 5.2 Grid Independence Study of 3D Mesh | 64 |
| 5.3 Comparison of 2D and 3D Simulations for Liquid Piston Compression | 67 |
| 5.4 Numerical Simulation Validation without Spray Injection | 69 |

| | |
|---|----|
| 5.5 Computational Results for Liquid Piston Compression with Spray Injection..... | 72 |
| CHAPTER 6: Numerical Simulation Results and Discussion..... | 79 |
| CHAPTER 7: Conclusions and Future Work | 83 |
| 7.1 Conclusions | 83 |
| 7.2 Future Work..... | 85 |
| Appendix A..... | 92 |

LIST OF TABLES

| | |
|---|----|
| Table 3. 1: Measurement devices and corresponding uncertainties | 31 |
| Table 3. 2: Polytropic Index and Spray work with different injection pressure | 43 |
| Table 3. 3: Polytropic Index of Compression | 51 |
| Table 4. 1: Mesh Specifications..... | 58 |
| Table 4. 2: Droplet parameters for numerical simulations | 61 |
| Table 5. 1: Droplet Properties for Fluent Simulation | 73 |
| Table 5. 2: Droplet Summary at end of compression process (3.1s) | 78 |

LIST OF FIGURES

| | | |
|---------------|---|----|
| Figure 1.1: | Schematic diagram of a CAES plant/facility[35]..... | 3 |
| Figure 1.2: | CAES Configurations[1] | 5 |
| Figure 2. 1: | Gas Control Volume in Liquid Piston Compressor..... | 14 |
| Figure 2. 2: | A model of spray-droplets in liquid piston using ANSYS-Fluent. | 15 |
| Figure 2. 3: | Droplet Volume distribution as a function of droplet diameter | 20 |
| Figure 2. 4: | Droplet Cumulative Volume distribution as a function of diameter | 21 |
| Figure 2. 5: | Rosin-Rammler distribution for 90 degree spray angle, 10 psi injection pressure..... | 22 |
| Figure 2. 6: | Various types of droplet spray patterns..... | 23 |
| Figure 3. 1: | A table-top setup of Liquid piston compressor with spray cooling | 24 |
| Figure 3. 2: | Spray Injection Setup | 26 |
| Figure 3. 3: | Full-cone nozzle (Bete WL ¼)..... | 27 |
| Figure 3. 4: | Pressure Transducer and Solenoid Valves | 29 |
| Figure 3. 5: | Chamber used for liquid piston compression experiments | 29 |
| Figure 3. 6: | Pressure-time plot without spray injection..... | 33 |
| Figure 3. 7: | Pressure time plot for different spray injection pressures | 34 |
| Figure 3. 8: | Pressure-time plot for a single cycle | 35 |
| Figure 3. 9: | Pressure-volume plot..... | 36 |
| Figure 3. 10: | Zoomed view of Pressure- volume plot | 36 |
| Figure 3. 11: | Temperature – plot for a single compression cycle..... | 37 |
| Figure 3. 12: | Temperature-pressure plot during compression..... | 38 |
| Figure 3. 13: | Flow rate from spray nozzle during continuous cycle operation | 39 |
| Figure 3. 14: | Flowrate of spray water for different injection pressures during compression..... | 40 |
| Figure 3. 15: | Isothermal efficiency of compression for different spray injection pressures | 42 |
| Figure 3. 16: | Comparison of Reduced Work and Spray Work for different injection pressures | 44 |
| Figure 3. 17: | Temperature-pressure plot for different compression stroke times..... | 45 |
| Figure 3. 18: | Temperature –time plot for different compression stroke times | 46 |
| Figure 3. 19: | Pressure-time plots for different spray angles..... | 48 |
| Figure 3. 20: | Temperature-Pressure data for compression with different spray angles | 49 |
| Figure 3. 21: | Pressure- volume plot with different spray angles | 50 |
| Figure 3. 22: | Zoomed view of pressure- volume plot with different spray angles..... | 50 |
| Figure 4. 1: | Mesh of 2D Geometry..... | 53 |
| Figure 4. 2: | Mesh at Time T=0.885s and at T=0.913s..... | 55 |

| | | |
|---------------|---|----|
| Figure 4. 3: | Velocity Profile for 5s compression stroke time (30 psi air source pressure)..... | 56 |
| Figure 4. 4: | Velocity Profile for 4s compression stroke time (50 psi air source pressure)..... | 56 |
| Figure 4. 5: | Velocity Profile for 3s compression stroke time (80 psi air source pressure)..... | 57 |
| Figure 4. 6: | 3D Cylinder Geometry at the start of compression..... | 58 |
| Figure 4. 7: | 3D Cylinder Geometry at the end of compression..... | 58 |
| Figure 4. 8: | Injection properties for DPM for 90° spray angle and 10 psi injection pressure..... | 60 |
| | | |
| Figure 5. 1: | Computational Domain for 2D Axisymmetric Mesh [22] | 62 |
| Figure 5. 2: | Temperature - volume plot..... | 63 |
| Figure 5. 3: | Wall Heat Flux- time plot..... | 64 |
| Figure 5. 4: | Pressure - time plot for 2D and 3D simulations for 4.7 s compression..... | 65 |
| Figure 5. 5: | Volume-averaged temperature– time plot for 2D and 3D simulations for 4.7 s compression..... | 66 |
| Figure 5. 6: | Vertex-averaged temperature – time plot for 2D and 3D simulations for 4.7 s compression..... | 67 |
| Figure 5. 7: | Pressure-time plot for 3.6s compression for 2D and 3D simulations..... | 68 |
| Figure 5. 8: | Temperature–time plot for 3.6s compression for 2D and 3D simulations | 68 |
| Figure 5. 9: | Temperature–time plot for 3.1s compression for 2D and 3D simulations | 68 |
| Figure 5. 10: | Pressure –time plot for 3.1s compression for 2D and 3D simulations | 68 |
| Figure 5. 11: | Comparison of experimental and computational pressure results for a 3.13s (fast) compression cycle | 69 |
| Figure 5. 12: | Comparison of experimental and computational temperature results for a 3.13s (fast) compression cycle | 70 |
| Figure 5. 13: | Temperature contours for a 3.13s (fast) compression cycle in (a) 2D simulation and (b) 3D simulation..... | 71 |
| Figure 5. 14: | Comparison of experimental and computational pressure results for a fast (3s) compression cycle | 74 |
| Figure 5. 15: | Comparison of experimental and computational temperature results for a fast (3s) compression cycle | 74 |
| Figure 5. 16: | Residence time of droplets in the chamber at the end of compression | 76 |
| Figure 5. 17: | Droplet temperature (K) in the liquid piston chamber at the end of compression..... | 77 |
| | | |
| Figure 6. 1: | Wall heat flux for different injection pressures..... | 79 |
| Figure 6. 2: | Total heat transfer rate for different injection pressures | 80 |
| Figure 6. 3: | Evaporation rate during compression process for different injection pressures | 81 |

CHAPTER 1: Introduction

Renewable energy resources play an important role in reducing the energy dependency from fossil fuels. Rising energy demands across the world have necessitated research into renewable energy resources, energy conservation, and energy storage measures. Various electrical energy storage methods such as high power density batteries, fuel cells, hydroelectric storage, and compressed air energy storage (CAES) systems have been explored. Apart from hydroelectric power storage, energy storage is not widely present in the energy utility grid scale. An important issue with renewable energy resources is the variation in the energy supply to the grid. Renewable energy sources such as wind, wave, and tidal energy have significant day-to-day fluctuations. Typically, to counter these fluctuations between demand and energy available, backup power plants are installed that use natural gas turbine generators consuming fossil fuels in the process. To minimize the fluctuations and reduce energy losses, CAES systems can provide a viable alternative to serve as large-scale energy storage systems. Efficient energy storage systems facilitate effective utilization of intermittent renewable energy sources. To achieve commercially viable energy storage systems, CAES systems need to be highly efficient and have high power density at the same time.

In a CAES plant air is used as an energy storage medium by compressing it using an electric compressor and then expanding it at peak time over a gas turbine to generate electricity. The concept of CAES systems started in the early 1960s due to the need for storing off-peak power from the baseline power generation capacities. CAES systems can store energy for a significantly long time-frame in terms of weeks or months while having a large-scale energy storage capacity. Budt, Wolf, Span, & Yan, (2016) reviewed the development, basic principles and the challenges faced for CAES applications. They concluded that the development of CAES systems faced

considerable competition from a mix of hybrid power plants, grid-connected photovoltaics, and the general decrease of peak/off-peak electricity costs. Further research into the technical and economic aspects of CAES plants was required for viable CAES systems. Currently, two CAES plants are in operation around the world. The first CAES plant was set up in Huntorf, Germany in the 1970s, initially with a 290 MW capacity which was later expanded to 321 MW in 2006([2]). With the Huntorf plant in operation and growing research into CAES systems, the US Department of Energy (DOE) started R&D into developing CAES plant with the objectives of long-term reservoir stability and development of second generation CAES plants with an adiabatic storage.

The second CAES plant was built in McIntosh, Alabama in 1991 for a 110 MW capacity[3]. Both the plants use solution-mined salt caverns as the compressed air storage units and are used during full-load operations of the expander/turbine. CAES systems store energy in the form of high pressure compressed air and can be utilized at the peak demand requirement. A traditional approach for CAES plants is to store energy in the storage units at night during low-peak electricity hours and supply the electricity during the daytime. Several studies have been carried out to improve the overall efficiency of CAES systems for improvement in controls and operation of the plant, compressor optimization, efficient storage units etc. To further improve the efficiency of CAES systems, understanding the thermodynamics is one of the most important aspects.

A typical CAES system consists of the following:

1. Compressor
2. Motor/Generator unit
3. Turbine/ Expander
4. Compressed air storage unit

A schematic of a CAES facility showing its various components is presented in figure 1.1. The compressor is run using the motors at off-peak hours to compress air to a high pressure. The high-pressure air is then sent to an underground air storage unit. The storage unit can be natural caverns or artificial storage units. When the electricity demands exceed the supply, additional

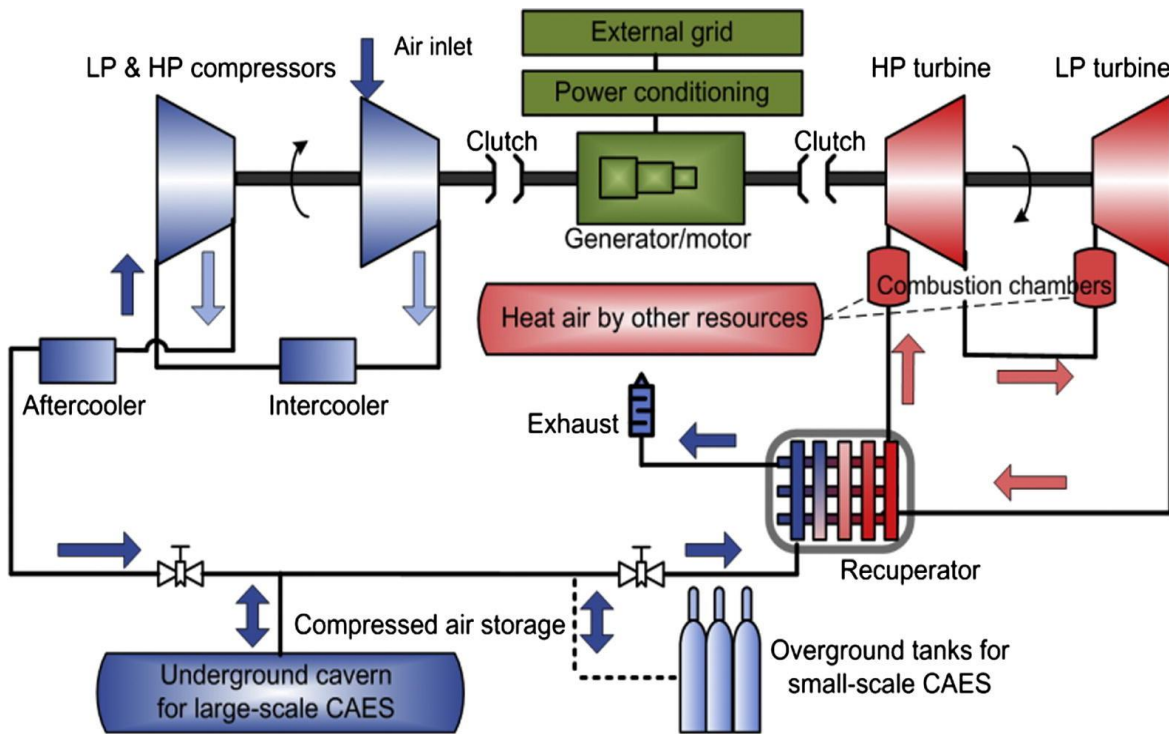


Figure 1.1: Schematic diagram of a CAES plant/facility[35]

energy is supplied by passing compressed air through a gas turbine or an expander which then runs the generator to provide additional electricity. The compressor and expander are the key components in a compressed air energy storage plant. Development of an efficient compressor and expander would make compressed air energy storage systems economical and competent.

Another important component of the CAES system is the compressed air storage unit. The storage unit can either be constant volume storage or constant pressure storage. This affects the

performance of the expander/turbine as with a constant volume unit the pressure of the delivered air reduces during the expansion to the turbine.

Conventionally the storage vessels are kept above ground or are utilized in the form of naturally occurring caverns. A novel idea was discussed by Lim, Mazzoleni, Park, Ro, & Quinlan, (2012) to place the compressed air storage unit in the ocean and to utilize the high-pressure water as the surrounding environment for the compressed air. They considered a conceptual design for an OCAES system with a thermal energy storage unit. A thermodynamic analysis was presented based on adiabatic CAES system which showed the overall efficiency of 65.9%. During the expansion process when the air is drawn from the storage unit and the mass of air reduces, the pressure of air for a typical vessel reduces as well and creates fluctuations in the generated electricity. By placing the storage unit on the ocean bed, the hydrostatic water pressure can maintain the air pressure as constant during the release of air and the additional fluctuations can be eliminated. Using this technique, the Ocean Compressed Air Energy Storage (OCAES) system can be further combined with off-shore wind energy to create a highly efficient energy storage unit. [5].

CAES configurations can be broadly classified on the basis of the energy and exergy analysis of the system. The CAES configurations are distinguished on the heat transfer during the process of compression and prior to the air expansion process. Several studies have discussed the potential and drawbacks of CAES system based on exergy analysis such as diabatic CAES, adiabatic CAES, isothermal CAES, micro-CAES with thermal energy storage (TES), etc [6], [7].

However, the CAES system can be broadly classified into three main categories which are discussed further and depicted in figure 1.2.

1. Diabatic CAES

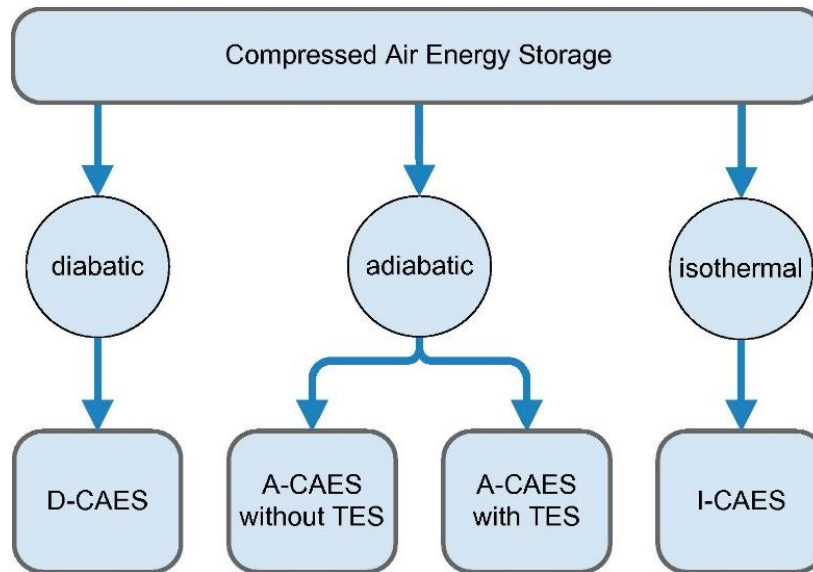


Figure 1.17: CAES Configurations[1]

In a diabatic CAES system, the air is compressed conventionally and at the end of the compression the high pressure, high temperature air is cooled to ambient storage unit temperatures before sending it to the air storage unit. In this mode of operation, there is a loss of thermal energy while cooling. This heat loss has to be compensated at the time of energy recovery by preheating the air using fossil fuels before it is sent to the turbine for combustion. For a conventional gas turbine, the electrical output from the turbine is used to compress the air to a high pressure and high temperature medium, while for a CAES system the compressor is decoupled from the turbine thereby utilizing its maximum capacity[8]. As the compression stage can take up to two-thirds of turbine capacity, decoupling it can allow the turbine to run at a higher capacity for the same gas input. This increases the specific gas output while reducing the associated CO₂ emissions. By

decoupling the compressor, it can instead be run by using the off-peak lower cost electricity than utilizing high-cost electricity to compress the air. This configuration is being used in the two operational CAES plants at Huntorf, Germany and McIntosh, USA.

2. Adiabatic CAES

For an adiabatic CAES system, no heat is lost or supplied during the compression and expansion processes respectively. The heat of compression is either stored in a separate thermal energy storage (TES) unit or the energy is stored in the compressed air itself. For an adiabatic CAES system, complex design and engineering are required for the design of compressor capable of high temperature delivery at end of compression and pipelines carrying high pressure and high temperature air etc. An adiabatic CAES system with TES eliminates the need for a fuel combustor for pre-heating the air during the expansion process [9]. The heat of combustion is stored in the TES which is then utilized for heating the air inlet to the expander/turbine. Storing the heat energy leads to improvement in the overall efficiency of the CAES system. In practical applications achieving adiabatic compression and storing the heat of compression are challenging aspects, however, research on TES have shown promising results for achieving adiabatic CAES [10].

3. Isothermal CAES

In an isothermal CAES system, the gas is compressed isothermally and expanded isothermally which results in the minimum compression work and maximum expansion work. Isothermal CAES system eliminates the need for fuel and high temperature TES [6] by the means of high heat transfer to the surroundings. Typically for an isothermal compression, the compression process involves a slow pressure change while allowing heat transfer to maintain the isothermal

process. Since in practical industrial applications it is difficult to achieve isothermal compression and expansion, innovative techniques such as liquid piston compressors and heat transfer enhancements have been extensively studied [11]–[13]. Liquid piston gas compression in combination with heat transfer enhancements can achieve near-isothermal gas compression which significantly improves the overall efficiency [14]–[16]. The goal of this thesis is to study liquid piston compression in detail, therefore the next few sections pertain to compressors and liquid piston compressors, and various heat transfer enhancement techniques.

1.1 Compressors

To achieve an isothermal compression process in the CAES/OCAES system a highly efficient compressor is needed. Since compressors and expanders are major components of CAES system, improvements in the energy efficiency of compressed air systems can generate in 20-50% of energy savings[17]. High heat transfer characteristics during the compression process are needed for reaching near-isothermal conditions. Typical air compressors for industrial applications tend towards an adiabatic compression process with high pressure and high temperature gases. This is because a significant proportion of the compression work is utilized in increasing the internal energy of the gas. Reducing the temperature of a gas during the compression process decreases the compression work. Typical gas compression processes operate at a high rpm which result in poor heat transfer characteristics and thus improving the heat transfer during compression would significantly reduce the temperature of the gas. As typical air compressors have rapid compression cycles and do not have adequate heat transfer, the temperature of the compressed air increases. This high pressure compressed air is then stored in pressurized vessels where the compressed gas gradually cools down to ambient conditions. This loss of thermal energy can be

avoided with the use of a liquid piston compressor which improves the heat transfer to the surroundings.

Coney *et al.* (2002) described a reciprocating piston compressor using water spray injection to achieve near-isothermal air compression. They substantially reduce the temperature and compression work by using high mass loading of water. Mass loading is defined as the ratio of the mass of water injected to the mass of air in the compression chamber. Increasing the amount of heat transferred out of the system would result in a near-isothermal process thereby improving the compression efficiency. Several strategies have been researched to achieve near-isothermal gas compression (Heidari *et al.* 2014). To achieve near-isothermal compression, Heidari *et al.* reviewed methods such as liquid piston compressors, dry finned piston compressors, etc. The liquid piston compression system involves compressing the gas using a moving column of liquid to a given pressure. From a single piston geometry multiple columns can be used to compress the gas while approaching a near-isothermal compression. As the surface area increases with use of multiple liquid piston surfaces, the heat transfer increases as well. This is explained in the following sections. Heidari and Rufer [20] proposed a finned piston concept where a number of sliding fins fit between the stator fins during compression process. The sliding fins are connected to shaft which acts as the guiding rod. The additional fins increase the heat transfer area for the compression process. While the finned piston system has its advantages such as elimination of water and equipment complexities, further research in liquid piston compressors along with heat enhancement techniques show significant improvement in the compression efficiency.

1.2 Liquid Piston Compressor

A liquid piston gas compression process was described by Van de Ven and Li (2009). In a liquid piston compressor, a displacing column of liquid is used as a moving piston to compress the gas to required pressures for a given chamber volume. The liquid piston process can be utilized to achieve a near-isothermal compression process with the use of heat transfer enhancement techniques. In a liquid piston compressor, the surface area to volume ratio can be maximized to improve the heat transfer as the liquid can fit any irregular chamber volume. This flexibility allows the liquid piston to be divided into multiple liquid columns with irregular volumes to maximum effective heat transfer area. By increasing the heat transfer, the compression process shifts to a near-isothermal condition with lower temperatures compared to a typical reciprocating compressor and the heat transfer coefficient observed was significantly higher compared to a reciprocating compression process [21]. This results in a lower bulk temperature of the compressed gas. With a near-isothermal compression the compression work required also reduces. The liquid piston compressor can be significantly improved by optimizing its geometrical design, adding cylinders, fins etc. This concept also has significant advantages. The surface area to volume ratio can be increased multi-fold compared to reciprocating compressors by increasing the number of liquid pistons. Additionally, it reduces air leakage from the system. It also replaces sliding friction of the piston rings to viscous friction of the liquid. It is also convenient to accommodate water spray cooling in the chamber as the droplets eventually fall in the liquid surface. In this thesis, water is used as the liquid piston to compress the air to a high pressure. However, different gases can be compressed, and the gas temperature decides the liquid used for compression. There also exist a few challenges for practical liquid piston compressors. Firstly, at high pressures the gas may be soluble in the liquid or at a high frequency operation there might be splashing of the liquid in the

chamber. These issues can be solved by using a low-solubility liquid for the compression and optimizing the design to minimize the splashing of liquid. The liquid may also leave with the compressed gas during the exhaust stroke through the valves [21]. This could be resolved again by improving the design to prevent splashing and by placing a liquid trap at the exit of the exhaust valve. Van de Ven and Li concluded that the liquid piston compression required 19% less energy compared to the reciprocating piston compression and improved the compression efficiency by 13%.

1.2 Heat Transfer Enhancement Techniques

Improving the heat transfer characteristics in a liquid piston compression process plays an important role in increasing the efficiency of the liquid piston compressor. To achieve an isothermal compression or expansion the instantaneous work should be equal to the instantaneous heat transfer rate. It is observed that the heat transfer coefficient is very high at the start of compression as the thermal boundary layer is extremely thin and the temperature difference between the wall and the bulk of the gas is very small. The heat transfer coefficient increases with increase in piston velocity[22].

Heat transfer analysis of liquid piston compression for hydrogen applications was studied by [23]. Their sensitivity analysis suggested that the heat transfer coefficients and compression time were important factors in reducing the hydrogen temperature. Increasing the heat transfer coefficient at the wall by 200 times leads to a 33 % reduction in hydrogen temperature. Piya et. al. performed a numerical study of liquid piston compression to enhance the heat transfer in the system. As industrial compressors run at high pressures close to 200 bar, the effect of moisture content during the compression process plays an important role [24]. Anirudh and Li (2018)

developed a 0-D and 1-D model where they observed that above a compression efficiency of 85-90 % the differences between steam and no steam cases were minimal. Heat transfer enhancement in liquid piston compression can also be achieved by optimizing the trajectories for the compressor [16]. They observed a 10-40 % increase in power density by optimizing the piston profile while also considering the effect of viscous friction.

To improve the heat transfer in the liquid piston compressor, Zhang et al. studied the heat transfer during compression with porous media inserts in the compression chamber[25]. The porous medium allows the gas and liquid to pass through uninterrupted while increasing the surface area available for heat transfer, and thus reducing the temperature rise during the compression process. They studied open-cell metal foams and interrupted plates as porous media inserts. The metal foam has thin filaments which improve the flow mixing while the interrupted plates are designed in a staggered fashion to break up the thermal boundary layers. This allowed for a higher heat transfer coefficient between the gas and the solid plates. Experiments and computational studies were performed for both metal foam and interrupted plate matrices. The models characterized the pressure drop and the thermal dispersion within the inserts. They observed that the bulk temperature remained below 360 K with the metal foam while the adiabatic bulk temperature would reach 575 K without any porous media inserts. By improving the heat transfer through porous media inserts the efficiency of the liquid piston compressor increases and shifts the process towards a near-isothermal condition.

An experimental study was conducted by Yan et al. to study the heat transfer enhancement in a liquid piston using porous media inserts [15]. Similar to Zhang et al. they studied different interrupted cell matrices and metal foams. Using porous media inserts, they quantified the increase in power density and efficiency during the compression and expansion processes. It was observed

that the power density increased by 39 times at 95% efficiency and the efficiency increased by 18% at 100 kW/m^3 for the compression process. The major contributing factor for increasing the heat transfer from the liquid piston compressor/expander was the increase in surface area from the porous media inserts.

A novel technique of using hollow spheres on the surface of the liquid piston was studied with the spheres of different materials[26]. Introducing spheres in the liquid piston chamber increases the surface area available for heat transfer and therefore limits the temperature rise during compression. The spheres absorb the heat via conduction and convect the heat to the liquid. A strong correlation was not observed between the heat transfer and the material of the sphere. Instead, the presence of a solid surface to increase the heat transfer was more important. Similar to using porous media inserts, hollow spheres do not require any additional compression or cooling work during the process.

Another method of improving the heat transfer or reducing the temperature of the compressing gas is to inject water droplets during the compression process[14]. For a liquid piston compressor with water as the compressing liquid, water spray injection is miscible while at the same time it utilizes the high specific heat of water to absorb the heat and reduce the temperature of the gas. Several researchers have studied droplet dynamics and heat transfer between air and water spray [27]. Sureshkumar *et al.* (2008) performed experiments on water spray and ambient air to study evaporative cooling. They investigated spray cooling for parallel flow and counter-flow configurations with different nozzle pressures, nozzle diameters, environmental conditions, and air velocities[29]. Accordingly, they observed that for a given flow-rate, higher injection pressure with a smaller nozzle diameter resulted in a higher temperature drop of air. Since the goal

of water spray injection is to minimize the temperature rise, the amount of water injected and the droplet dynamics are of significant importance.

In this thesis, the effect of spray injection during the liquid piston compression process is investigated. The following chapters contain a detailed introduction of spray cooling in the liquid piston compressor. After the introduction, the experimental setup for liquid piston compressor and spray injection are discussed. For the experimental parameters, the spray injection pressure, compression stroke time, and the angle of the nozzle are studied. The effect of these parameters are discussed in the following subsections. In chapter 4, the numerical setup, and the input parameters for the 2D and 3D simulations are discussed. Chapter 5 contains the validation of the numerical simulations for the liquid piston compression process and the results of the numerical simulations. Chapter 6 discusses the effect of spray injection pressure during a compression process. This is explained in terms of the wall heat flux, total heat transfer rate, and the evaporation rate during compression. Finally, the conclusions and the future work on spray injection in liquid piston compressors are presented in chapter 7.

CHAPTER 2: Liquid Piston Compression with Spray Injection

As mentioned in chapter 1, the liquid piston compression process involves a moving column of liquid that compresses a finite gas volume in a compression chamber. During the compression process, the liquid enters the compression chamber and reduces the volume available for the gas and thereby increases the gas pressure and temperature. Figure 2.1 shows the control volume in the liquid piston compressor. The compressed gas is sent out to the compressed air storage vessel through the outlet port. The inlet port fills the chamber with the gas to the initial conditions while the piston retracts to its original position.

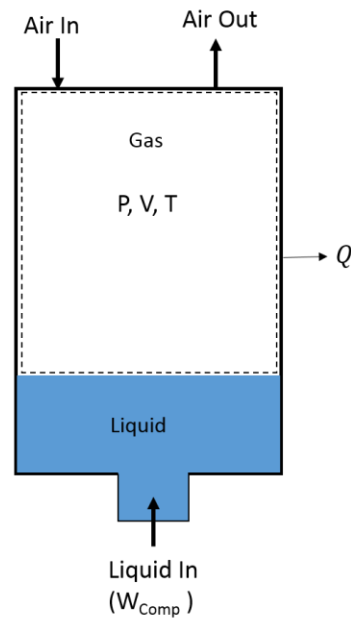


Figure 2. 1: Gas Control Volume in Liquid Piston Compressor

A gas compression process is a polytropic process which follows the relation in eq 2.1.

$$pV^n = C \quad 2.1$$

where p is the pressure, V is the volume. n is the polytropic index, and C is a constant. This thermodynamic process describes the compression and expansion of the gas and includes the work

and heat transfer in the system. The polytropic index provides a reference for various types of processes and also determines how close the process is to an isothermal process. A polytropic index for a compression process close to 1 represents a near-isothermal process with a high compression efficiency. For CAES applications, achieving a high pressure gas without the accompanying high temperature is the primary objective. To do this, high heat transfer is required during the compression process. An isothermal compression process involves conversion of all the compression work into the heat transfer in the system. Improving the heat transfer would shift the polytropic compression process towards a near-isothermal process and increase the compression efficiency. Spray cooling concept can be utilized to increase the heat transfer during the compression process where a high pressure spray of water droplets is injected into the liquid piston compressor. Water droplets can absorb heat from the air during compression. Figure 2.2 depicts the injection of water droplets into a compression chamber and a moving column of the liquid piston.

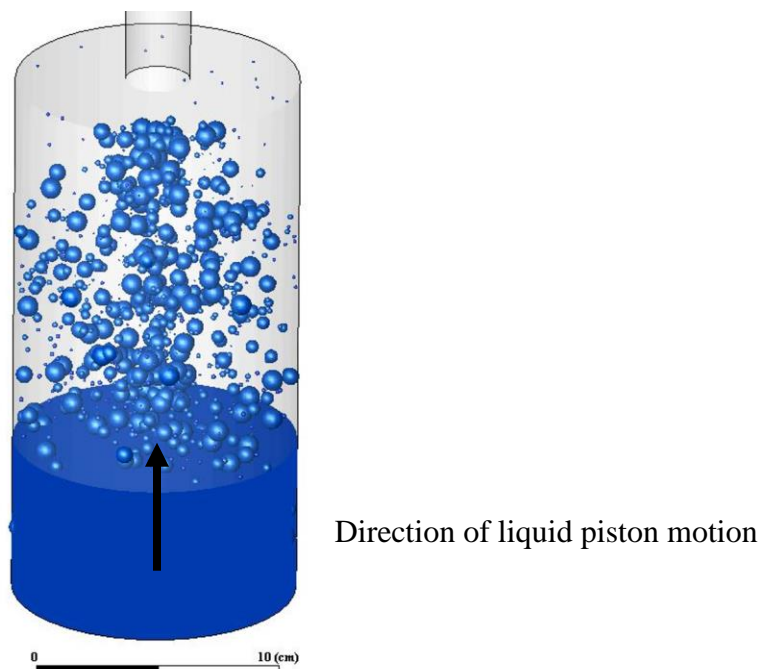


Figure 2. 2: A model of spray-droplets in liquid piston using ANSYS-Fluent.

Qin and Loth [14] explained that a high heat transfer can be achieved with fine droplets and a high mass loading factor as a large surface area is obtained during this setup. Mass loading is defined as the ratio of the mass of water injected to the mass of air in the compression chamber. Increase in the mass of water in the compression chamber allows more heat to be absorbed by the droplets. The spray nozzle can be activated during the expansion stroke as well as during the compression stroke. They studied droplet heat transfer for different droplet diameters, total mass injection, and various methods of injection [14].

Direct injection and premixed injection were the types of injection studied. In premixed injection, the spray is mixed with the inlet air before the intake stroke while in the direct injection process the spray is injected directly into the compression chamber during the expansion and compression strokes. Direct injection had higher heat transfer compared to premixed injection cases due to the fact that the droplets were airborne at the end of compression stroke period. Qin and Loth found that for a constant mass loading, reducing the droplet diameter increased the heat transfer till 20 μm after which no significant improvement was observed. The difference in the temperatures at the end of the adiabatic compression process and isothermal compression process was about 300 K; thus, a significant temperature reduction is required to bring the compression process to near –isothermal conditions. Spray cooling is a highly effective heat transfer mechanism due to a large interfacial surface area with a large number of droplets. Therefore, spray cooling is estimated to show an improvement in the compression efficiency from 71 % for an adiabatic compression to a maximum of 98% with spray cooling for a tenfold pressure ratio.

Investigations by Qin et al. suggested that CAES can be combined with off-shore wind farms to harness the wind energy[5]. They perform simulations over a three-stage compressor with spray cooling as a heat transfer enhancement technique and observed a substantial increase in the

overall compression efficiency compared to the adiabatic compression process. The effect of the spray characteristics in terms of the Sauter Mean Diameter (SMD) and the flow rate are discussed. This increase in efficiency could be used to reduce the capacity of the wind turbines and electrical generators as they do not need to be sized for a maximum output capacity.

Further enhancement in spray cooling characteristics in liquid piston compression can be achieved by optimizing its trajectories. The spray profile and water-air mass ratio can be optimized to obtain maximum isothermal efficiency for a variable flow rate compared to a constant spray flow rate[16].

Spray cooling experiments and simulations have been conducted for applications in high and critical heat flux processes in electronic cooling where droplet dynamics and the heat transfer are studied [27]. Droplet dynamics in spray cooling is an interesting phenomenon where three distinct operational modes exist for spray cooling [30]. The first case is where the surface vaporizes all of the impinging spray which is referred to as the ‘dry-wall’ state. The second situation is when the spray forms a thin liquid film on the hot surface, which is called the ‘flooded’ state. The third is the ‘Leidenfrost’ state where a thin vapor film is created between the impinging spray and the surface. For the liquid piston compression process as the hot air may evaporate the spray or the spray might settle on top of the liquid piston, it creates a flooded state.

Jia and Qiu investigated heat transfer due to spray cooling on a hot surface where a full cone nozzle at high pressure was used to cool a heated copper surface [27]. A lumped capacitance method was assumed for the spray droplets and the behavior of heat flux and expulsion rates were analyzed. The droplet diameters were of the order 1 μm to 100 μm . As the diameter of the droplet is increased for studying sub-millimeter scale, the Reynolds number can be kept the same by reducing the velocity but the Grashof’s number increases leading to an increased effect of

buoyancy; the increase in Webber number also decreases the surface tension which creates a non-spherical shape.

Mathematical modeling and experimental research on spray cooling were conducted by Yuan et al.[31] They studied the film thickness and temperature distribution in the impact area in their models and also considered the micro-scale phenomenon such as velocity slip and the temperature jump. The heat transfer coefficient was calculated and compared to the experimental observations. They observed that the temperature jump had a significantly greater influence on the heat transfer coefficient than the velocity slip boundary conditions and that the heat transfer coefficient decreased with increased flow velocity.

Sureshkumar *et al.* conducted an experiment to study the heat and mass transfer characteristics of a water spray in ambient air [29]. They performed a parallel and counter flow experimental flow while varying the nozzle sizes, water pressures (1, 2, 3 bar) and air velocities (1, 2, 3 m/s). A hollow cone sheet was generated, and the temperatures were compared for change in dry bulb temperatures for different nozzle pressures. From the experiment, it was concluded that for evaporative cooling smaller diameter nozzles at high pressures fared better at reducing dry bulb temperature than large diameter nozzles at low pressure. The drawback was that for high pressures the pump input increased; therefore, an optimum diameter and pressure are required to maximize the cooling.

A CFD simulation was carried out to study evaporative cooling from water spray systems by Montazeri *et al.* [32]. A hollow cone nozzle configuration was considered and a 3D steady RANS simulation was performed. A Lagrangian-Eulerian approach was used for the two-phase flow system with the droplets being modeled on a Rosin-Rammler distribution. This model used an exponential distribution for the droplet diameter and for the mass density distribution. Two

important parameters are presented in the article: Mean diameter D_{10} and Sauter mean diameter D_{32} , which are used in the droplet density distribution. 3% of the droplets evaporated based on the input parameters during the simulation.

The design of the nozzle along with spray angle will affect the heat transfer as different spray patterns on the liquid piston surface and the angle determine the number of droplets that absorb heat versus the droplets that collide with the wall surfaces. Droplet dynamics is in itself a vast field with extensive research being carried out to characterize the droplet physics. During the atomization process from a spray nozzle, the liquid sheet breaks up into droplets which is termed as the primary breakup. When these heavier droplets further break down into finer droplets, this is described as the secondary breakup. The droplet distribution depends on the shape and size of the droplet. The surface tension and aerodynamic forces play an important role in the droplet size and mass distribution. These parameters affect the vaporization, condensation, droplet coalescence, and shattering phenomenon of the droplets. The droplet diameter distribution can be a uniformly distributed domain or can be modeled using semi-empirical models such as Rosin-Rammler distribution. The Rosin-Rammler distribution is commonly used to characterize liquid sprays. These semi-empirical models ‘fit’ the observed droplet data to a mathematical function. The distribution function is based on an exponential relation between the droplet diameter ‘d’ and the mass fraction of droplets with a diameter greater than d that is Y_d which is given in equation 2.2.

$$Y_d = e^{-\left(\frac{d}{\bar{d}}\right)^n} \quad 2.2$$

where \bar{d} is mean diameter and n is the spread parameter which indicates the width of the distribution. The Rosin-Rammler distribution is used in the numerical simulations to describe droplet properties. For the current nozzle, the droplet characteristics are obtained from the manufacturer. They provide the number density distribution, surface area, volume, and the

cumulative volume distribution for different spray angles and different injection pressures. Y_d correlates the mass density distribution. For water droplets with constant density, the cumulative volume distribution can also be used for calculating Y_d . Figures 2.3 and 2.4 show the volume distribution and the cumulative volume density distribution for a 90° spray angle at 10 psi spray injection pressure respectively.

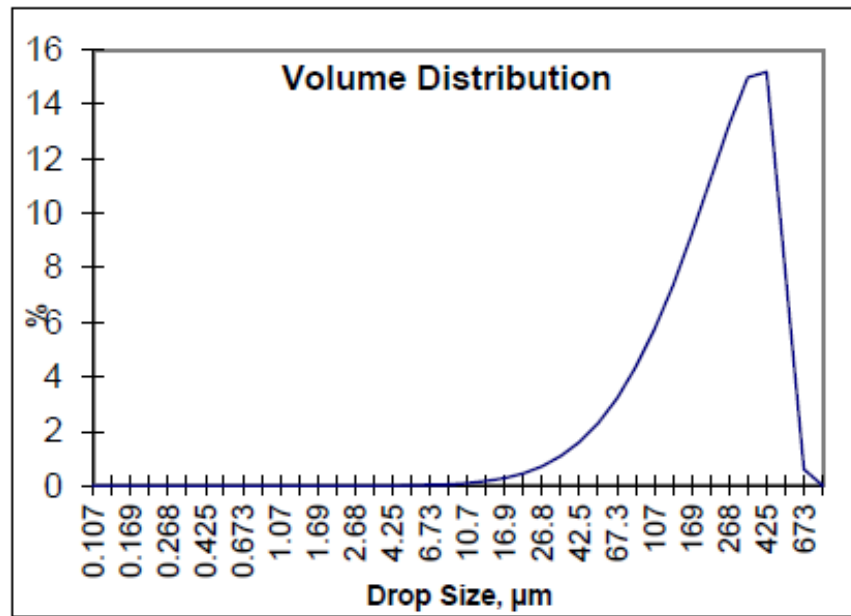


Figure 2. 3: Droplet Volume distribution as a function of droplet diameter

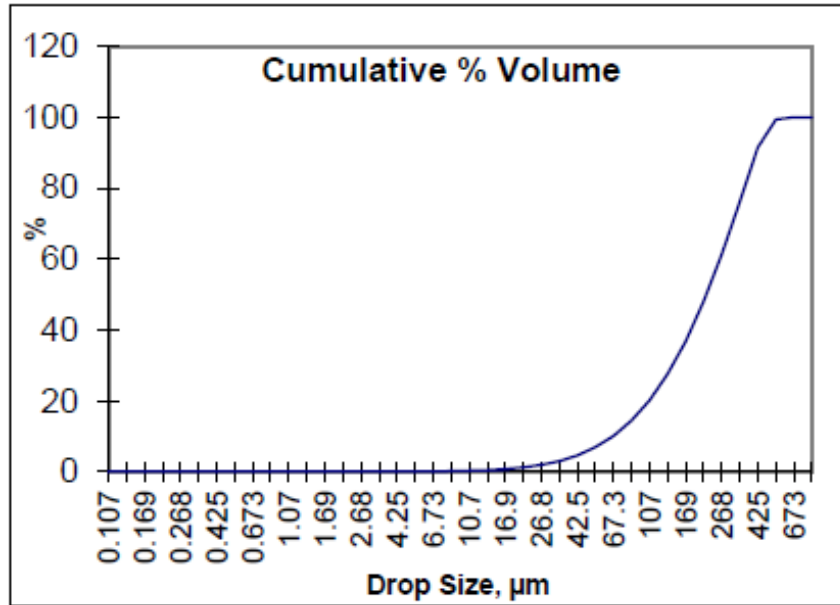


Figure 2. 4: Droplet Cumulative Volume distribution as a function of diameter

Using this distribution the data points were extracted and a model function was created in Matlab. The model function was used to find the value of ‘n’ from the distribution. The function found the value of n by minimizing the squared error between the value of the density distribution Y_d from the data points and the mathematical function. The mean diameter used in the model was Volume mean diameter (VMD or $D_{V0.5}$), which was again obtained from the manufacturer datasheet. The estimated data points and the Model approximation are shown in figure 2.5.

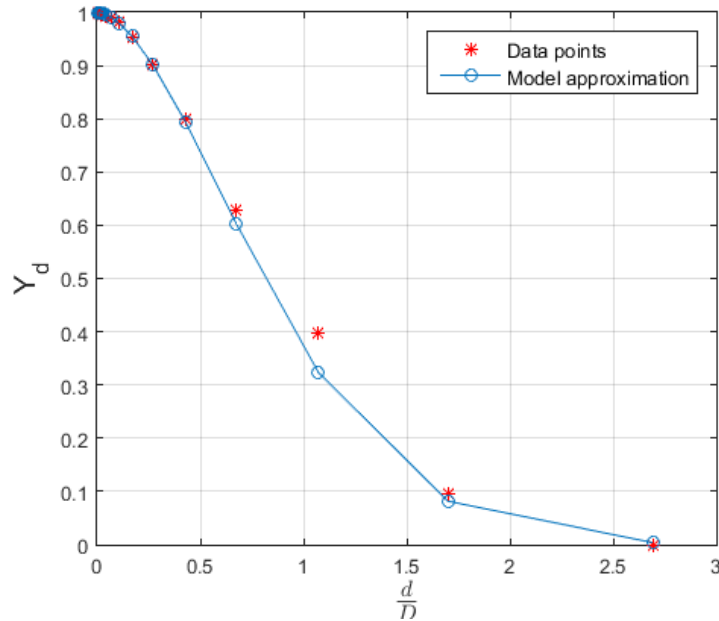


Figure 2. 5: Rosin-Rammler distribution for 90-degree spray angle, 10 psi injection pressure

The droplet distribution in figure 2.2 is plotted on a log-scale which means that fewer data points are available to create the model approximation in figure 2.3 and find the spread parameter of the distribution. To characterize the diameter distribution, the mean diameter was used in the model. The mean droplet diameter is given in equation 2.3

$$\phi_{m,n} = \frac{\int_0^{\infty} f(\phi)\phi^n d\phi}{\int_0^{\infty} f(\phi)\phi^m d\phi} \quad 2.3$$

where ϕ_{32} is used to represent the droplet diameter for a spray. ϕ_{32} is known as the Sauter mean diameter (SMD) and is proportional to the ratio of the volume of liquid droplets to the total surface area of the droplets. The SMD along with the VMD or simply the mean diameter are commonly used to characterize the droplets.

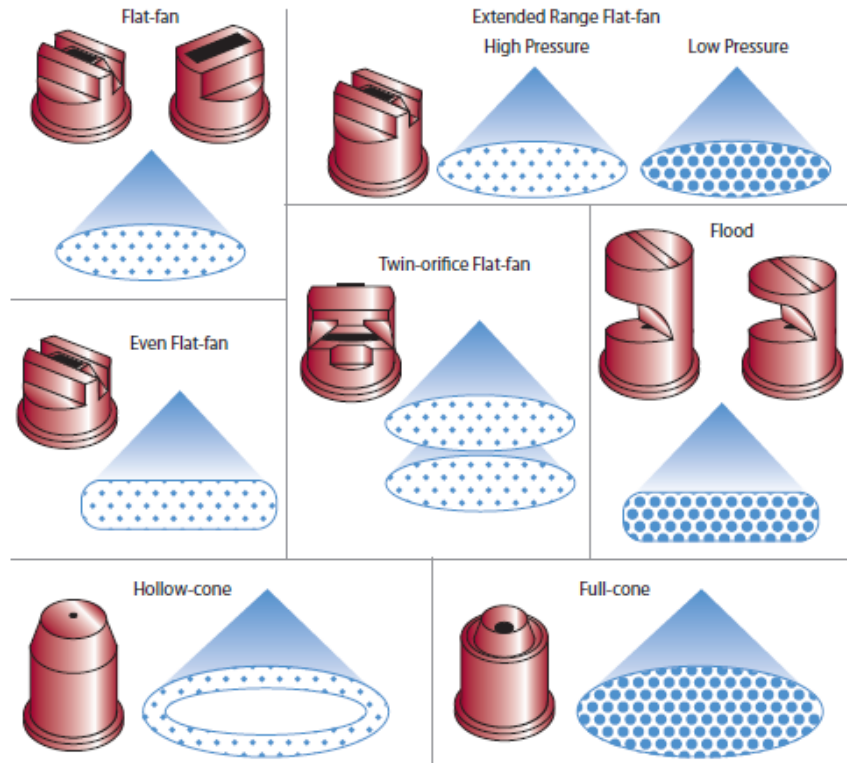


Figure 2. 6: Various types of droplet spray patterns

The droplet sizes are also strongly dependent on the nozzle type. Various nozzle types exist for different spray applications ranging from painting, fuel injection to agricultural uses. Figure 2.6 shows different types of spray nozzles creating various spray patterns. In the current study, two nozzles were initially considered: the hollow cone nozzle and the full cone nozzle. The hollow cone nozzle has finer atomization and an even droplet size distribution which can be used at low flow rates. The full cone nozzle covers the entire surface of the moving liquid front during the compression process and provides a higher mass loading. Even though the droplet size distribution for full cone nozzle is slightly higher than the hollow cone nozzle, it is estimated that its higher mass loading may contribute to improved heat transfer in the liquid piston compressor/expander. Therefore, a full cone nozzle is used in the experiments for spray cooling in the liquid piston compressor.

CHAPTER 3: Experimental Setup

In this chapter, the experimental setup of water spray cooling in a liquid piston compressor on a table-top setup is discussed. The objective is to observe its effect on temperature reduction during the compression process for a 2.5 compression ratio. The experiments are performed with and without any spray injection into the compression chamber. The experimental setup is similar to the one used by Kishore [26]. Figure 3.1 shows the experimental setup used for the investigations.

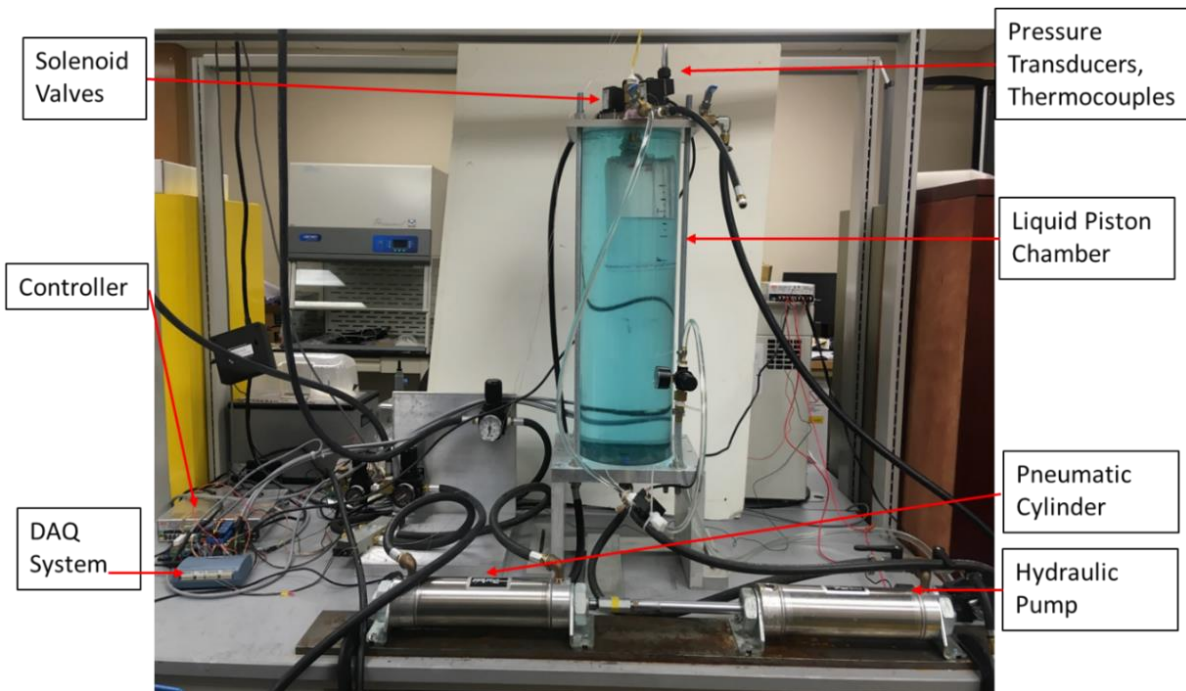


Figure 3. 1: A table-top setup of Liquid piston compressor with spray cooling

3.1 Liquid Piston Compressor Setup

The experimental setup built for the liquid piston compression process uses water as the medium and a polypropylene chamber for a compression vessel. The setup consists of a compression chamber, solenoid valves, intake and exhaust valves, pneumatic cylinder, hydraulic

pump, controller, Data Acquisition System (DAQ), and measurement instruments. The outer cylinder contains water acting as a surrounding environment for the compression chamber. This helps achieve a higher heat transfer rate between the chamber wall and the surrounding water during the compression process compared to air as the surrounding medium. Water from a hydraulic pump drives the liquid piston interface in the innermost chamber during the compression process which compresses the air and is retracted by a coupled pneumatic piston-hydraulic pump for the intake stroke. A cycle consists of the compression stroke followed by the exhaust of high-pressure air, ending in the intake stroke where atmospheric air fills the chamber to reach initial conditions. During the compression process, the liquid piston moves in the upward direction and continuously reduces the air volume while increasing the pressure and temperature. Each experimental test case is run for about 10-12 continuous cycles to confirm repeatability and evaluate the cyclic variability. The controller actuates the solenoid valves which regulates the intake and exhaust of air at the end of compression. The measurement devices are explained in the following sections. A LabVIEW program was used for the continuous operation of the liquid piston. A plastic container was used as the compression chamber with a diameter of 10.96 cm and the height of the initial air volume as 12 cm.

3.2 Spray Injection Setup

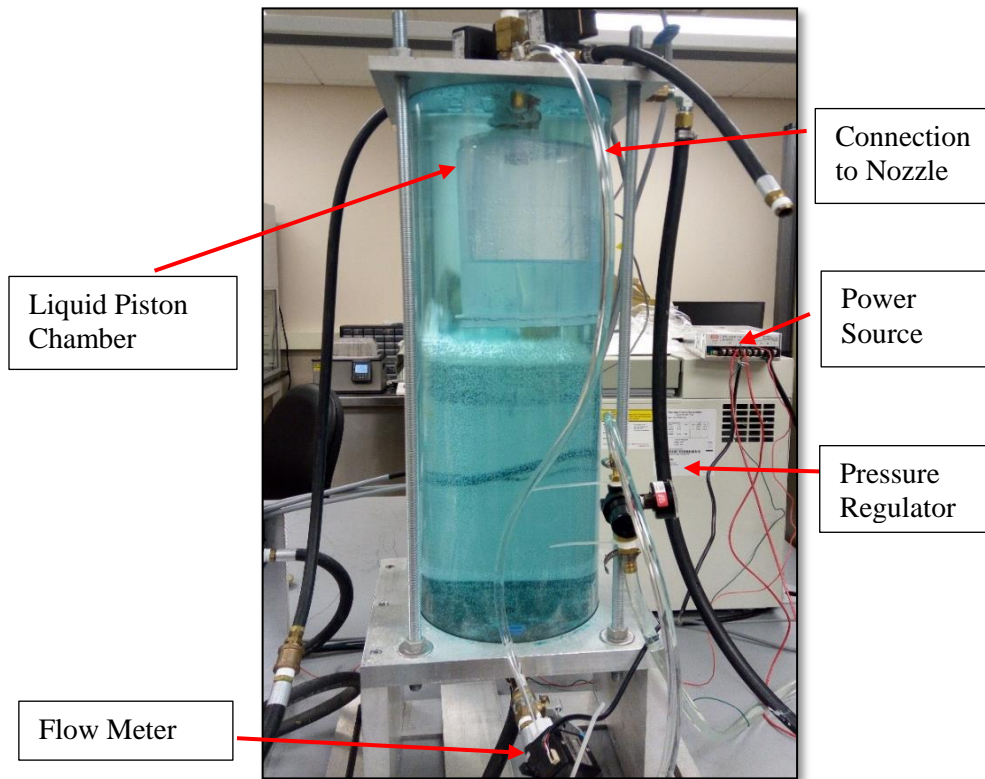


Figure 3. 2: Spray Injection Setup

The experiments for the water spray injection during the compression process are setup using an external closed loop. The schematic of the spray cooling setup is shown in figure 3.2 and the system consists of spray nozzles, pump, power source, pressure regulator, flow meter, and DAQ. A positive displacement pump set to a maximum pressure of 100 psi (689 kPa) is used to drive the water spray into the chamber. Using a closed loop, the exit of the outer cylinder is connected as an inlet to the pump. This ensured that the volume of air at the start of each compression cycle remained the same and no secondary drain was needed for the additional water from the spray. As the pump is switched on, the spray injection starts in the chamber and its injection pressure is controlled using a pressure regulator. To measure the flow rate of water during

the compression process, a flowmeter was connected after the pressure regulator. The flowmeter and pump are powered using a 12 VDC power supply, with the flowmeter readings being recorded by the DAQ. The spray nozzle is mounted on the top surface of the compression chamber and radially centered to generate a symmetric spray pattern on the liquid piston surface.

From previous experiments, it was observed that during compression cycles for cases without any spray injection, additional air volume seeped into the spray water line at the end of the compression stroke at high air pressures. To maintain a constant air volume between the compression cycles during spray injection and the compression cycles without spray injection, a ball valve was installed after the flowmeter.



Figure 3. 3: Full-cone nozzle (Bete WL ¼)

The design of the nozzle along with spray angle will affect the heat transfer characteristics during compression. The different spray patterns on the liquid piston surface and the angle determine the number of droplets that absorb the heat of compression against the number of droplets that collide with the wall surfaces. The spray nozzles can be selected based on the type of nozzle (spray pattern), droplet distribution, spray angle, the material of the nozzle, required

injection pressure and the pipe size. In these experiments, a low-flow full cone nozzle with 0.045 in (0.1143 cm) in diameter from BETE (WL nozzle) was selected shown in figure 3.3. As the compression chamber has a small air volume, a low flow-rate nozzle was required, with a medium to fine droplet distribution. The pipe size used was 1/8 in so that the injection water line could be placed in the confined space at the top of the compression chamber. A brass nozzle was selected as it has a high resistance to wear and tear from the continuous operation of the system. As mentioned in Chapter 2, various types of spray nozzles can be used and here a full cone nozzle was selected as it covered the maximum air volume during compression. The spray angle and the injection pressure were varied which will be discussed in a further section.

The current setup of the spray cooling apparatus on the table-top is installed in an add-on manner, such that it can be removed or modified further to incorporate other heat transfer enhancement techniques such as porous media, or hollow spheres.

3.3 Measurement Equipment

During the experiments, the chamber air pressure, air temperature, and the displacement of the pneumatic cylinder were recorded using a LabVIEW program. The displacement of the pneumatic cylinder was used in calculating the instantaneous air volume as the total volume of water driven by the hydraulic pump into the liquid piston was known (800 mL of water).

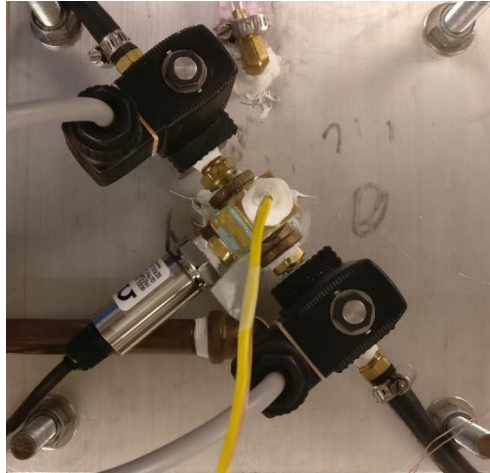


Figure 3. 4: Pressure Transducer and Solenoid Valves

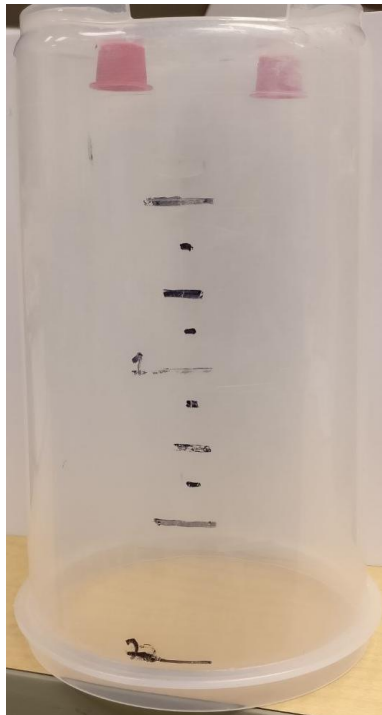


Figure 3. 5: Chamber used for liquid piston compression experiments

The air pressure is measured using a pressure transducer (OMEGA PX309 -100psi) mounted on the top plate of the outside cylinder along with the solenoid valves. The pressure transducer is a stainless steel transducer which uses a high accuracy silicon sensor. The pressure transducer used is shown in figure 3.4. Since the pressure is a homogenous gas property, the whole

air domain can be considered at the same pressure for measurement purposes. Two thermocouples are placed inside the compression chamber for measuring the temperatures. The thermocouples used are K-type 40 gauge diameter which are placed in radially opposite directions about 1 in from the center of the spray nozzle and 1/2 in below the top surface of the compression chamber. To prevent water droplets from continuously interacting with the thermocouples and affecting the temperature readings during the spray injection, the thermocouples were surrounded by a plastic casing which is shown in figure 3.5. This ensured that the droplets did not directly interact with the thermocouples, however, indirect collisions due to splashing and rebounding water droplets could not be avoided.

These measurement instruments are connected to the DAQ to measure the interior conditions during the compression and expansion process. The DAQ system converts the analog voltage signals from the transducer and thermocouples into digital signals to log into the computer. A programmable logic control was developed earlier by previous researchers in the lab to automate the compression process for multiple cycles using a LabVIEW program.

For the spray cooling data, the spray injection pressure is controlled using a pressure regulator (NORGREN R91W-2AK-NLN) and the flowmeter used is OMEGA flr-1012. Using a dial on the pressure regulator, the injection pressure is varied for the experiments. The measurement instruments and their uncertainties are mentioned in Table 3.1. Before starting the experiments, the measurement devices were calibrated repeatedly to obtain accurate results.

Table 3. 1: Measurement devices and corresponding uncertainties

| Measurement | Description | Accuracy |
|--------------------|---|-----------------|
| Temperature | K –Type Thermocouple | +/-2.2 °C |
| Pressure | Electronic Pressure Transducer 0-100psig (0-689 kPa) | +/-0.25% |
| Volume | Location Sensor | +/-0.001” |
| Flowmeter | Electronic Flowmeter 0.5-5 L/min | +/- 3% |

3.4 Range of Experiments

The parameters studied in the following experiments are the spray nozzle angle, spray water injection pressure, and the compression stroke timing. The spray nozzle angles investigated are 60°, 90°, and 120°. For a given chamber diameter and height the spray angle affected the spread of the water droplets. For each spray angle, the compression cycle stroke time is varied from around 3s (fast) to around 5s (slow). This variation in stroke time was done by adjusting the inlet source pressure of the pneumatic cylinder which dictated the speed of the hydraulic pump driving the liquid piston compressor. With each spray angle and compression stroke time, the water spray injection pressure was varied between 10-70 psi. The water line injection pressure was varied from 40-70 psi for 60° spray angle and it was observed that the temperature and pressure profiles were similar. Therefore to understand the critical pressure beyond which significant changes were not observed, the injection pressure was varied from 10-70 psi for 90° and 120° spray angles. For each spray angle with different stroke times of compression, the pressure, volume, temperature, and flow-rate are measured. Each case was run for at least 10-12 cycles of compression.

The LabVIEW program was created such that either the compression ratio reached about 2.5 or the hydraulic pump had reached the end of the stroke. All the compression experiments were performed until 800 mL of water from the liquid piston was added into the compression chamber.

3.5 Results

The results of the compression process with and without any spray injection are presented in this chapter. The first part of the section discusses the effect of the injection pressure for a given stroke time and nozzle spray angle. This is followed by the effect of the compression stroke time. The last section discusses the effect of the nozzle spray angle for a fixed compression stroke time and fixed spray injection pressure.

3.5.1 Effect of Injection Pressure

In this section, a case with 120° spray angle with around a 3s stroke time of compression is discussed. Other cases are reported in the appendix section.

Before spray injection during the compression process, a case without any spray injection is performed to compare with the spray injection cases. Figure 3.6 shows the continuous pressure-time plot for around 10 cycles. This was done to observe the cyclic variability in the compression cycles. It is observed that the pressure reaches higher than 2.5 bar for all the compression cycles and the first cycle reached a higher pressure than the other following cycles. This is because the 1st cycle starts from atmospheric pressure conditions while for the other cycles the pressure drops below 1 bar. This occurs after the exhaust stroke when the during the intake or expansion stroke

there is insufficient time for the chamber to fill up to atmospheric conditions and therefore the pressure is below 1 bar. However, the pressure ratio remained a constant for all the cycles.

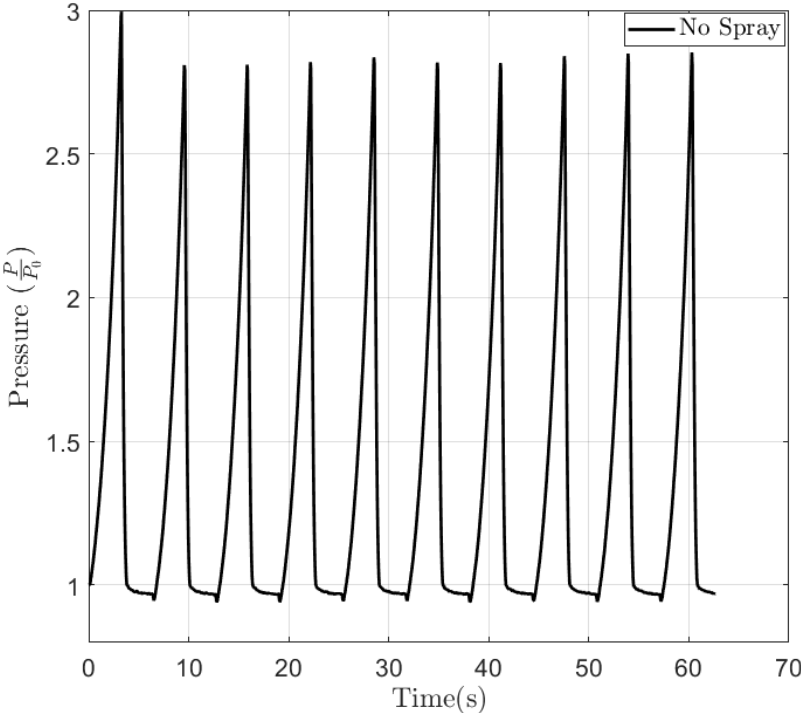


Figure 3. 6: Pressure-time plot without spray injection

Figure 3.7 shows the pressure-time plot for the different spray injection pressures from 10psi to 70 psi. Even though the pressure reached in the 1st cycle is higher than the other cycles the pressure ratio remained the same.

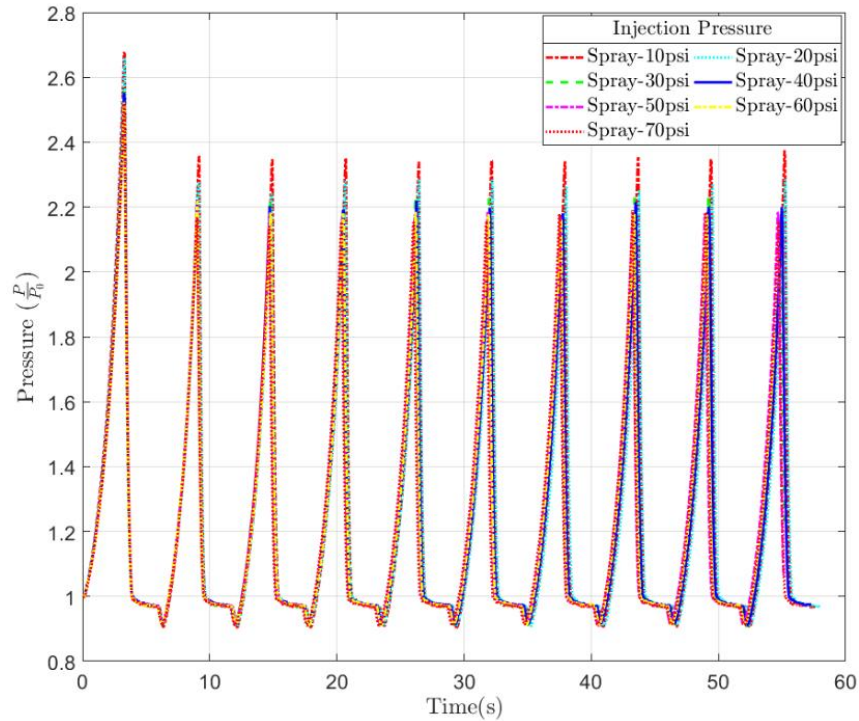


Figure 3. 7: Pressure time plot for different spray injection pressures

The pressure in the compression chamber for a single cycle with and without spray injection is shown in figure 3.8. The plot shows the compression and intake stroke. The maximum pressure at the end of the compression stroke was observed with the case of no spray injection. On injection of spray during compression, the final pressure reached was lower than that of without spray injection. The final pressure reached decreased with the increase of spray injection pressure and the pressure ratio dropped from 3 to around 2.5 when water spray is introduced. The lower pressure achieved with spray injection was due to the lower temperature reached at the end of the compression period.

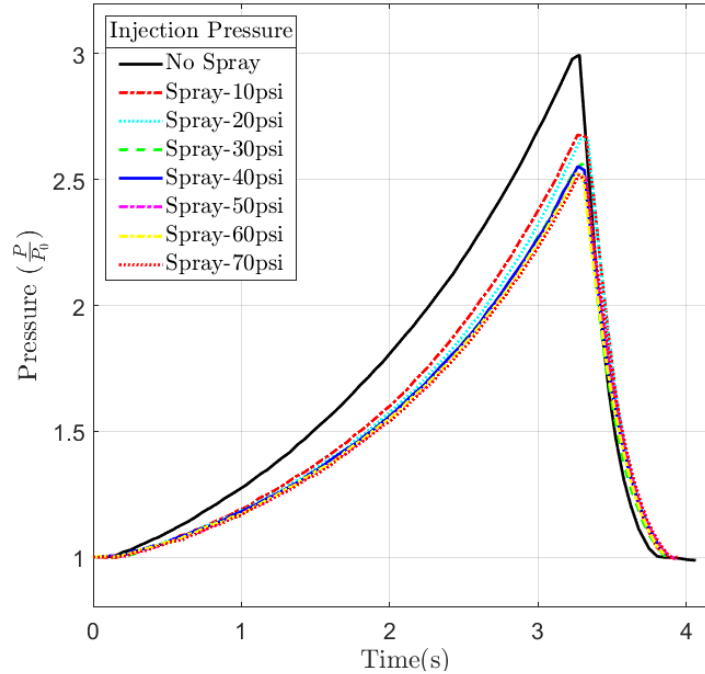


Figure 3. 8: Pressure-time plot for a single cycle

The effect of spray injection pressure is shown in the pressure-volume plots in figures 3.9 and 3.10. In these plots, a single cycle is depicted to discuss the effect of injection pressure. As injection of water spray during compression provides water droplets for heat transfer enhancement, this effect is observed through the compression work and the temperature reduction during the compression process. The water-droplets have a lower temperature than the air during the compression process and absorb the heat of compression thus reducing the air temperature. The polytropic compression curves along with the ideal isothermal and adiabatic polytropic curves are also plotted. The plots show that the injection of water spray during the compression shifts the polytropic curve towards the isothermal conditions compared to no spray being injected. A trend is observed in a zoomed view of the pressure-volume plot where on increasing the injection pressure towards 70 psi the curve shifts towards near-isothermal conditions. From the pressure-volume plot, the compression work can also be calculated as the area under the curve. With an

injection of water spray, the compression work required reduced compared to compression without any spray injection. However, this shift towards isothermal conditions costs additional pump work for higher injection pressures.

As lower compression work is required at near-isothermal conditions compared to adiabatic conditions, the pressure achieved is lower for the same final volume. From the pressure-volume plot, the polytropic index of compression can also be calculated and is reflected in the isothermal efficiency of compression. Increasing the spray injection pressure changes the polytropic index from 1.25 to 1.09-1.03 at higher injection pressures. This is further used in calculating the isothermal efficiency of compression and is discussed in further sections.

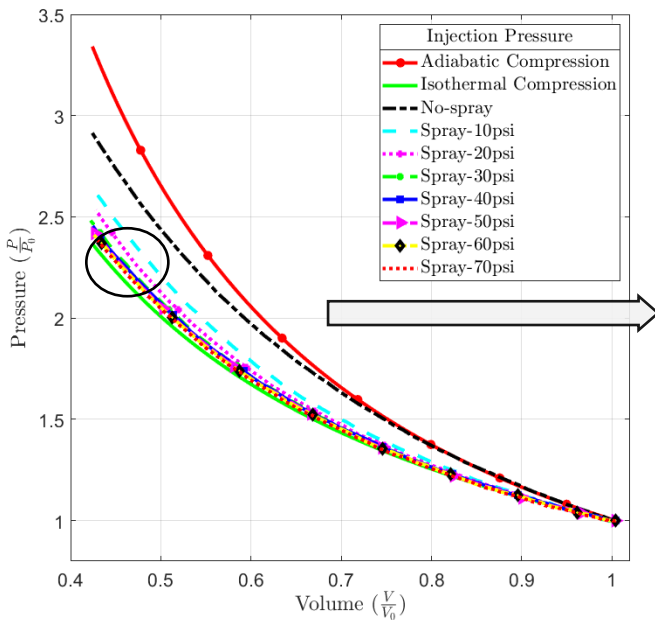


Figure 3.10: Pressure-volume plot

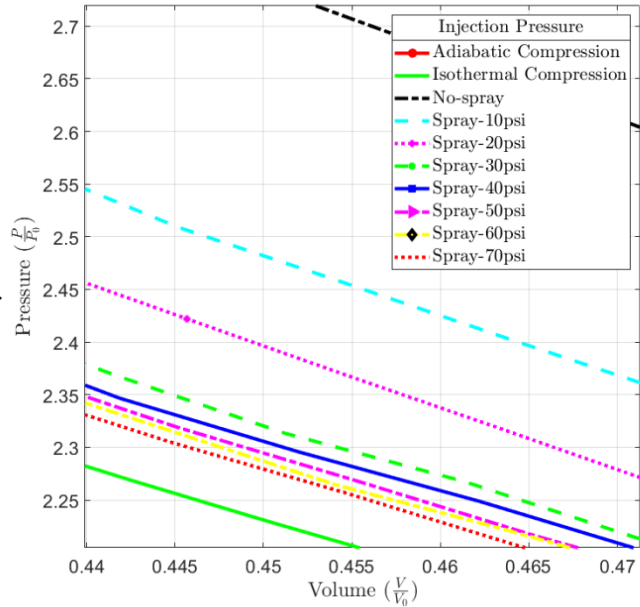


Figure 3.9: Zoomed view of Pressure- volume plot

From the pressure-volume plots, it is observed that increasing the injection pressure uniformly does not reflect a similar incremental shift in the polytropic curves. Beyond a spray injection pressure of 30 psi, a further increase in injection pressure does not show a lot of variation

since the curve already approaches a near-isothermal condition. This can also be noted from the temperature –time plot shown in figure 3.11 for a single compression cycle.

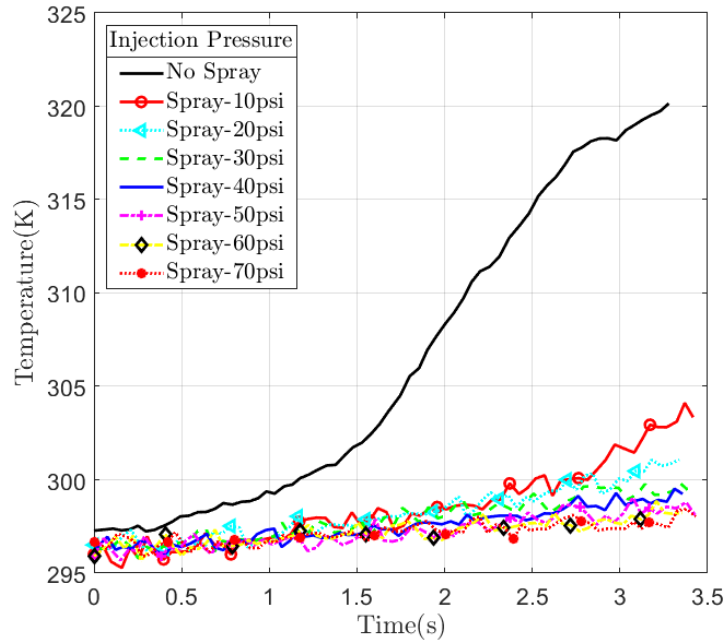


Figure 3. 11: Temperature – time plot for a single compression cycle

From figure 3.11, it is observed that the without any spray injection the temperature can reach around 320 K. On introduction of spray into the chamber, the temperature drops below 305 K and after 30 psi injection pressure, the temperature profiles remain around 298-300 K. A trend can also be observed of the temperature reduction where increasing injection pressure shifts the curve towards the initial temperature of 298 K to reach near-isothermal conditions.

Figure 3.12 shows temperature vs pressure plot with and without any spray injection. It is observed that the maximum temperature obtained is without any spray injection. With increasing pressure during the compression process, the temperature increased accordingly. The temperature reached without any spray injection is considerably higher than the temperatures reached with spray injection. On addition of spray of 10 psi injection pressure, the temperature at the end of compression is not as high during compression without any spray injection, however not as low as

with injection pressure from 30-70 psi. A temperature drop of 15-20K is observed from no spray injection to the injection of spray with varying injection pressures. Similar to the pressure-volume plot, a trend is observed with temperature decreasing consistently with increasing injection pressure. This increase in injection pressure increases the flow rate of spray which results in absorption of a larger amount of heat during compression. As a result of higher mass loading and finer droplets being injected, the heat transfer rate increases resulting in a higher temperature drop with higher injection pressure.

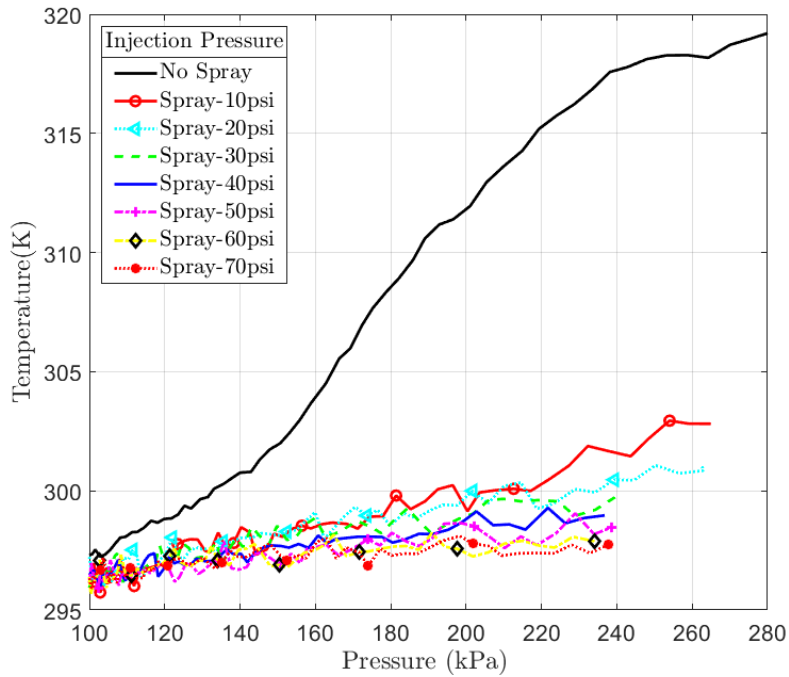


Figure 3. 12: Temperature-pressure plot during compression

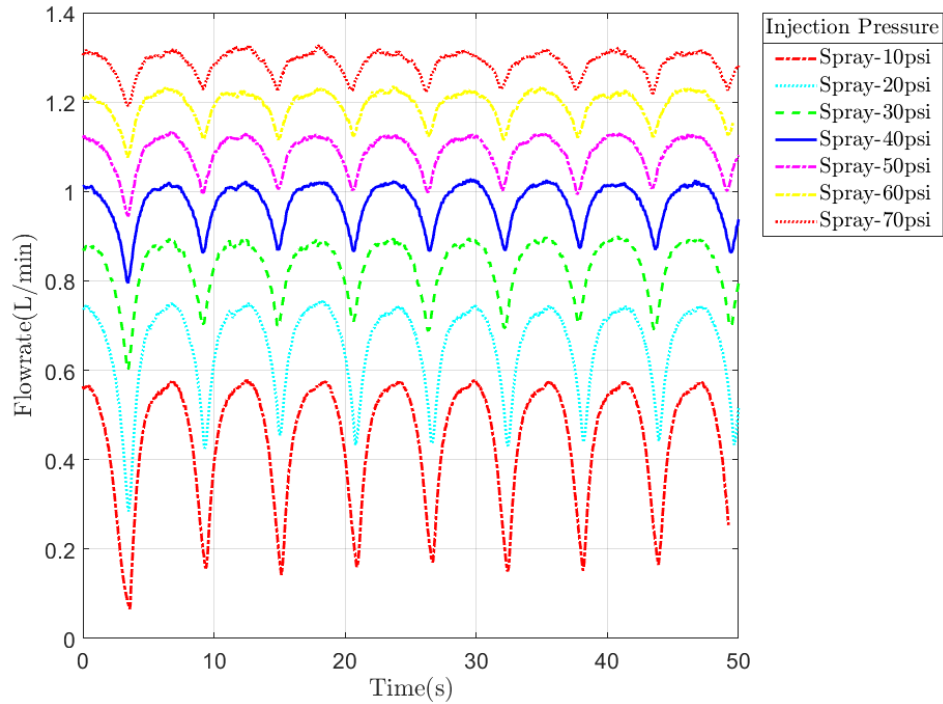


Figure 3. 13: Flow rate from spray nozzle during continuous cycle operation

The flow rate of the spray nozzle is reported in figure 3.13. The flow rate for higher spray injection pressures is higher and all the curves follow a similar profile. During each compression cycle, the flow-rate decreases and then increases before the start of the next compression cycle. The flow-rate varies from significantly at the lower injection pressures since it was affected to a greater extent by the air chamber pressure than observed at higher injection pressures.

This is explained by figure 3.14 showing the flow-rate for different spray injection pressures against the chamber air pressure during the compression stroke. During the compression process, the flow-rate decreases consistently for all the injection pressures. This is due to the backpressure created on the spray nozzle with the increasing pressure in the compression chamber. This leads to a compression similar to ones without spray injection towards the end of compression, particularly at lower injection pressures.

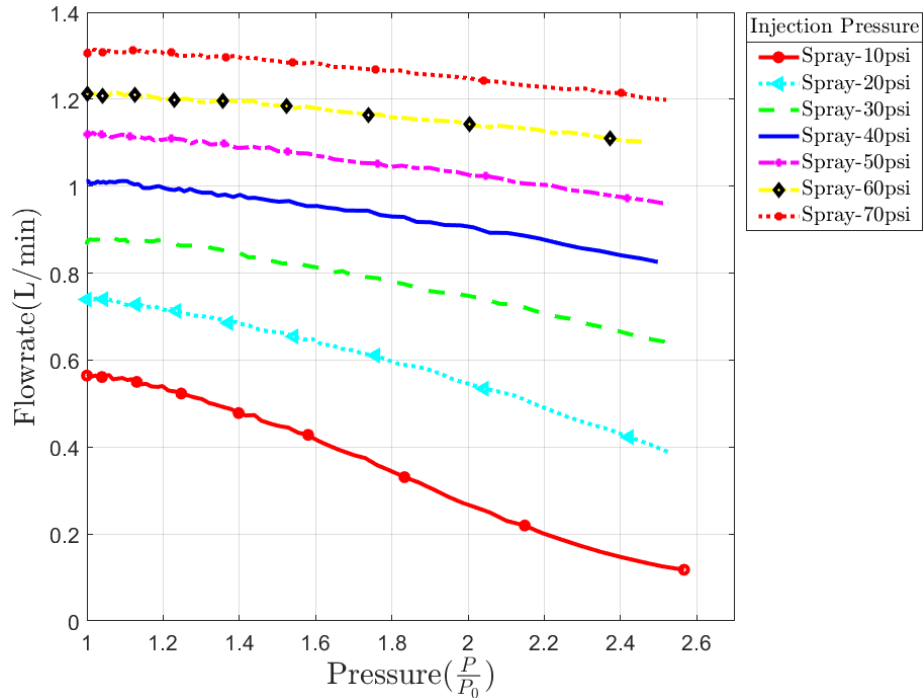


Figure 3. 14: Flow rate of spray water for different injection pressures during compression

Addition of spray to a compression process achieved a lower temperature at the end of compression compared to no spray injection. From the pressure-volume plot, the shift towards isothermal conditions and reduction of compression work is observed. The shift towards near-isothermal conditions is also observed from the temperature-pressure and temperature-time plots.

A combined parameter such as isothermal efficiency of compression can be used to explain the improvement in temperature reduction for air compressors. For a liquid piston compression process, Patil and Ro (2018) characterized the isothermal efficiency of compression given in equation 3.1.

$$\eta_c = \frac{\overbrace{\ln(P_r) + \frac{1}{P_r} - 1}^{\text{Energy Stored}}}{\underbrace{\frac{P_r^{n-1} - 1}{n-1}}_{\text{Compression Work}} + \underbrace{P_r^{-1} - 1 + (P_r - 1) \left(P_r^{-1} - \frac{1}{P_r} \right)}_{\text{Cooling Work}}} \quad 3.1$$

where P_r is the compression pressure ratio and n is the polytropic index of compression.

The isothermal efficiency of compression is given as the ratio of the stored energy to the input work. The stored energy is the amount of isothermal work extracted during expansion of compressed air to the atmosphere. The input work consists of the compression work, cooling work, and the frictional work. For liquid piston compression, the frictional work can be neglected. The cooling work is the work required to cool the system to initial temperature. Figure 3.15 shows the isothermal efficiency of compression. For each spray injection pressure, the efficiency is calculated using the respective compression ratio achieved. The liquid piston setup has an efficiency of 74-76% with liquid piston compression without any spray injection. It is observed that the increasing the injection pressure of spray increases the isothermal efficiency of compression. The isothermal efficiency reaches a maximum of 94-96 % for an injection pressure of 70 psi. The incremental improvement in efficiency decreases after injection pressure of 30 psi. However, a higher spray work is required with an increasing injection pressure of spray, which may affect the overall compression efficiency. Further investigations to evaluate and optimize the overall compression efficiency would be needed to find the optimum injection pressure of spray.

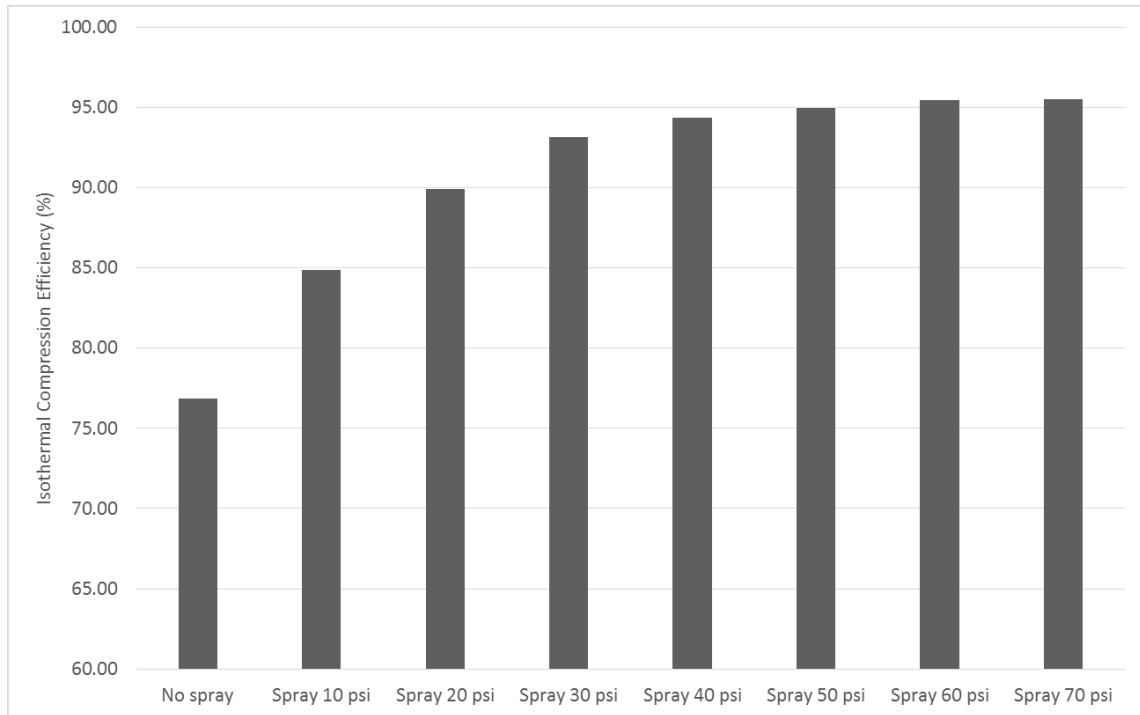


Figure 3. 15: Isothermal efficiency of compression for different spray injection pressures

Table 3.2 shows the polytropic indexes of compression and spray work during compression with different injection pressures of spray. It can be seen that the spray with higher injection pressures can achieve a polytropic index of compression less than 1.05 and increase of injection pressure shifts the process towards near-isothermal conditions. Therefore, spray cooling is highly effective in achieving near-isothermal compression.

Table 3. 2: Polytropic Index and Spray work with different injection pressure

| Process | Polytropic index (n) |
|-----------------|----------------------|
| Adiabatic | 1.4 |
| No Spray | 1.2545 |
| Spray (10psi) | 1.1423 |
| Spray (20psi) | 1.0892 |
| Spray (30psi) | 1.0574 |
| Spray(40 psi) | 1.0464 |
| Spray(50-70psi) | 1.041-1.036 |

However, increasing the injection pressure requires additional pump work for spray injection. With increasing injection pressure, the addition of spray cooling reduces the compression and cooling work compared to no spray injection. This also increases the spray work during compression. Hence, an optimum injection pressure where the reduced compression work or energy saved is higher than the additional spray work can be calculated. The spray work is calculated using the injection pressure and the flow rate. The reduced compression work is calculated as the difference between the input work without spray injection to the input work with spray injection. Figure 3.16 shows the comparison between the reduced compression work and the spray work for different injection pressures. It is observed that initially the energy saved is higher than the additional spray work. The spray work continuously increases with increase of spray injection pressure. An optimum injection pressure exists where the difference of the reduced compression work and the spray work is maximum. This lies between 40-50 psi for the current

spray angle of 120° with a fast compression process. It may vary slightly based on the nozzle angle and compression process speed. It is also seen that at higher injection pressures of 60 psi and 70 psi the spray work exceeds the energy saved even though the isothermal compression efficiency is higher at these pressures. It should also be noted that in the current set of experiments additional spray work is required, however, if some of the liquid piston flow is diverted to create the spray or the spray injection itself drives the liquid piston motion (described in future work, section 6.2), additional spray work may not be required in the compressor. This is an important parameter which requires further investigation to optimize the injection pressure and compression efficiency.

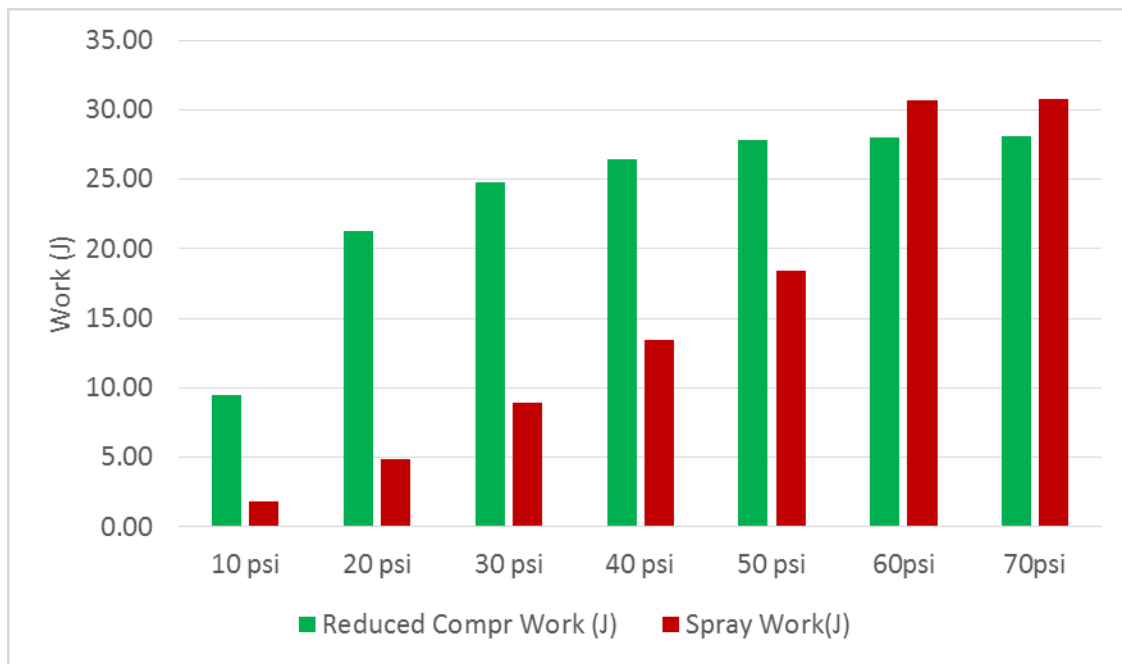


Figure 3. 16: Comparison of Reduced Work and Spray Work for different injection pressures

3.5.2 Effect of Stroke Time of Compression

Since the compression stroke time is varied between 3s – 5s (fast – slow compression), its effect on the air properties is studied. The spray angle of 90° with a spray injection pressure of 30 psi is reported in this discussion.

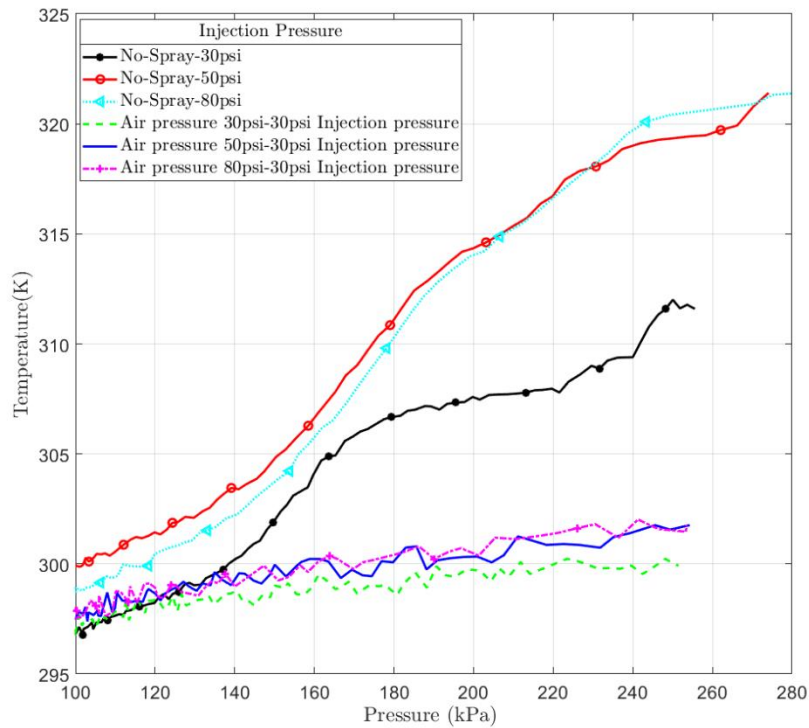


Figure 3. 17: Temperature-pressure plot for different compression stroke times

In figure 3.17, the air temperature is plotted against the air pressure for different compression stroke times with and without spray injection. Similar to figure 3.12, the temperature observed with spray injection during the compression process is lower than the temperature observed without any spray injection. For the 3s and 4s compression cycles (80 psi and 50 psi respectively), the temperature profiles are similar during the compression process. The 5s

compression process is relatively slower and hence the temperature observed is a bit lower. This difference is more prominent in the compression processes without spray injection than in with spray injection. With spray cooling, the temperature curves are very similar during the compression process and a near-isothermal compression can be achieved.

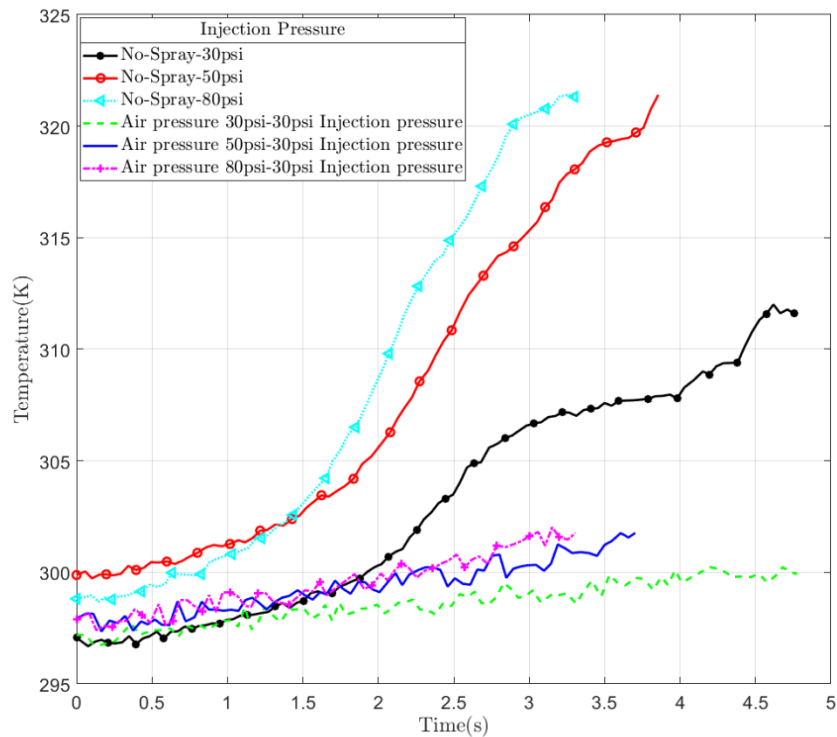


Figure 3. 18: Temperature –time plot for different compression stroke times

Figure 3.18 shows the temperature-time plot for different compression stroke times from around 3s to 5s with and without spray injection. All the temperature profiles with spray injection have an injection pressure of 30 psi. It can be observed that for the compression cases without any spray injection the temperature is higher than that observed with spray injection. The temperatures observed with spray injection are between 298 -305 K for all the stroke timings. Among the compression cycles of 3s, 3.6s, and 4.7s (80 psi, 50 psi, and 30 psi air source pressure), it is seen

that the rate of temperature rise is higher with the fastest compression stroke time of around 3s for both with and without any spray injection. With a spray injection pressure of 30 psi, the temperature at the end of compression differs by only 1-2 K for different stroke times. This shows that the compression stroke time does not have a strong influence on temperature when external water spray cooling is introduced in the liquid piston chamber for an injection pressure of 30 psi.

3.5.3 Effect of Spray Angle

The spray angle of the nozzle was varied between 60°, 90°, and 120° for the compression experiments. Theoretically, the nozzle angle and injection pressure determine the droplet characteristics. From the manufacturer's data on the droplet diameter, it is noted that increasing the spray angle for a constant injection pressure or increasing the injection pressure for a given spray angle decreased the mean droplet diameter. In the current set of experiments, the droplets from the 120° spray nozzle will hit the chamber walls earlier than the 60° and 90° spray nozzles during the compression process, which may affect the cooling.

The following discussion is for the spray angles 60°, 90°, and 120° for a compression time of around 3s and injection pressure of 80 psi. Figure 3.19 shows the pressure-time plots for the different spray angles. For the same injection pressure and compression stroke time, the pressure for the different angles follows the same pressure curve.

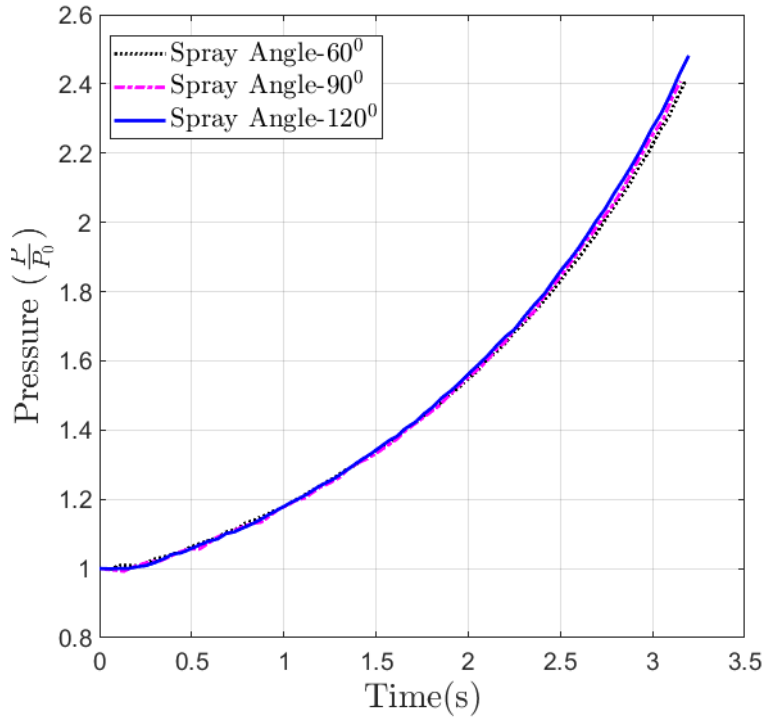


Figure 3. 19: Pressure-time plots for different spray angles

To observe the effect of the spray angle on the temperature reduction, the temperature–time curves are plotted in figure 3.20. It is observed that the temperature does not vary significantly during the compression process with spray cooling. Since the temperature values are within the standard deviation range of the thermocouple, a clear trend is not observed from these plots.

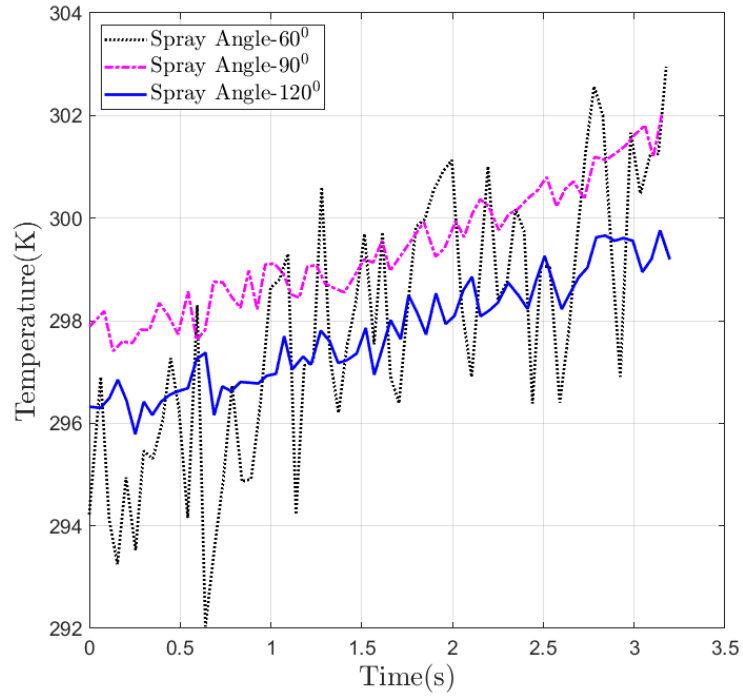


Figure 3. 20: Temperature-Pressure data for compression with different spray angles

The pressure-volume plot in figure 3.21 provides an alternate method to quantify the effect of the spray angle on the temperature reduction with the polytropic index. From figure 3.22, the zoomed view of the pressure-volume plot shows that 90° spray angle is closest to the isothermal curve and hence has the maximum temperature reduction.

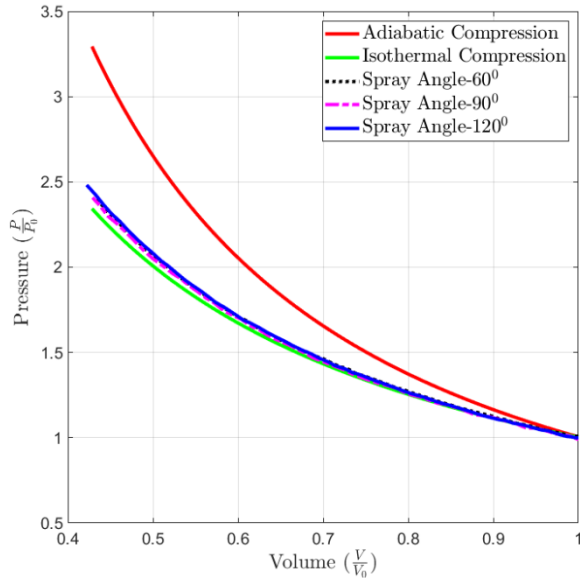


Figure 3. 21: Pressure- volume plot with different spray angles

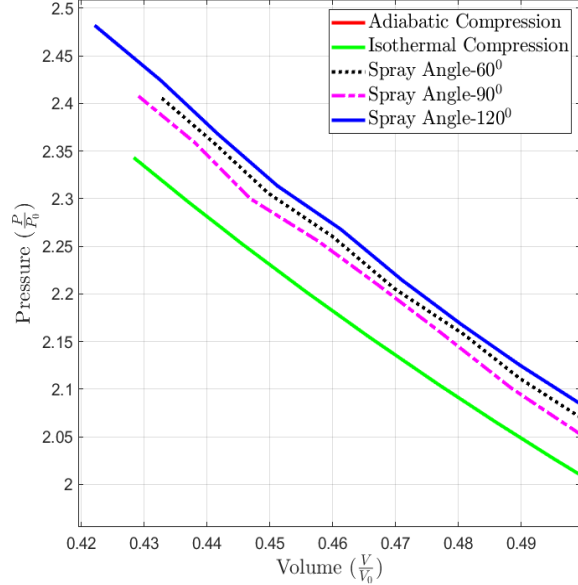


Figure 3. 22: Zoomed view of pressure- volume plot with different spray angles

The polytropic index for the compression processes with different spray angles are listed in Table 3.3. The polytropic index is lowest for the 90° spray angle followed by the 60° spray angle which suggests that the ideal spray angle for achieving maximum temperature reduction is between 60° and 90°. Since the chamber itself has a small volume compared to practical CAES units, and the droplets impact the walls in a short amount of time, the 120° angle may not be covering the entire air volume during the compression process. Hence, the 60°-90° angle range is observed to have lower polytropic index compared to the 120° spray angle.

Table 3. 3: Polytropic Index of Compression

| Process (Injection Pressure-30psi) | Polytropic index (n) |
|---|-----------------------------|
| Adiabatic | 1.4 |
| Spray Angle -60° | 1.0427 |
| Spray Angle -90° | 1.0418 |
| Spray Angle -120° | 1.0574 |
| Isothermal | 1 |

Even though the droplet diameter becomes finer with the 120° spray nozzle, since a higher percentage of those droplets impact the walls of the container than the 60° or 90° angle, the temperature reduction is not the same.

CHAPTER 4: Numerical Simulations

The liquid piston compression process is modeled using computational fluid dynamics simulations. A commercial package ANSYS Fluent was used for the simulations [36]. To start with the simulations, a 2 D model was created to simulate a liquid piston compression without any spray injection. Further, a 3D model was also simulated for the liquid piston compression process with and without any spray injection. This chapter describes the solution methods for the numerical simulations with the input parameters and models used in the setup of the simulation. For all the simulations of the liquid piston compression process, only the air domain was modeled as a reducing domain and the water driving the liquid piston was not modeled as it was not the subject of interest and was computationally expensive as well.

ANSYS Fluent solves the Navier-Stokes equation using a Finite Volume Method (FVM). In this method, the physical domain is discretized into multiple infinitesimal volumes using a computational mesh. Each volume describes the volume surrounding the node in the mesh. The partial differential equations are integrated over these finite volumes in a conservative form to generate algebraic equations. The equations for the discretized variables of pressure, temperature, velocity, and other conserved variables are solved in each control volume. The differential equations describing the volume integrals are converted into surface integrals using the divergence theorem. The Navier-Stokes and continuity equations are listed below from Eq. 4.1- 4.4:

$$\frac{\partial \rho}{\partial t} + \nabla \cdot (\rho V) = 0 \quad 4.1$$

$$\frac{\partial(\rho u)}{\partial t} + \nabla \cdot (\rho u V) = -\frac{\partial p}{\partial x} + \frac{\partial \tau_{xx}}{\partial x} + \frac{\partial \tau_{yx}}{\partial x} + \frac{\partial \tau_{zx}}{\partial x} + \rho f_x \quad 4.2$$

$$\frac{\partial(\rho v)}{\partial t} + \nabla \cdot (\rho v V) = -\frac{\partial p}{\partial y} + \frac{\partial \tau_{xy}}{\partial y} + \frac{\partial \tau_{yy}}{\partial y} + \frac{\partial \tau_{zy}}{\partial y} + \rho f_y \quad 4.3$$

$$\frac{\partial(\rho w)}{\partial t} + \nabla \cdot (\rho w V) = -\frac{\partial p}{\partial z} + \frac{\partial \tau_{xz}}{\partial z} + \frac{\partial \tau_{yz}}{\partial z} + \frac{\partial \tau_{zz}}{\partial z} + \rho f_z \quad 4.4$$

Along with the mass, momentum, and energy equations, the species equations are also solved to account for the evaporation of water droplets during the spray injection.

4.1 2D Simulation Setup

For the 2D simulations in Fluent without any spray injection, a transient pressure-based simulation was set up. The diameter of the chamber cylinder is 10.96 cm and the height of the air domain was 13.89 cm. The smaller diameter tube at the top of the chamber has a 1.76 cm diameter and 4.7 cm height. The mesh used for the 2D setup is shown in figure 4.1.

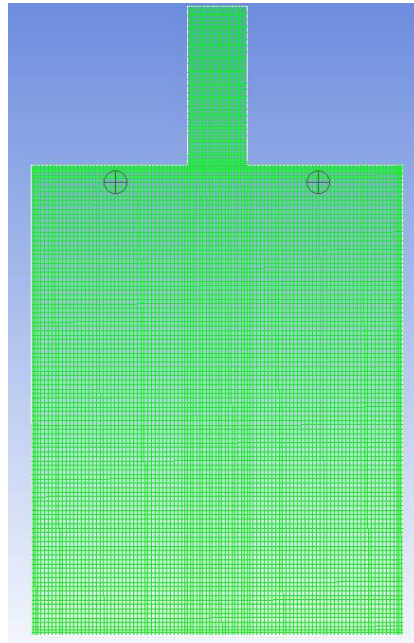


Figure 4. 1: Mesh of 2D Geometry

The volume of the air domain matches the experimental value of 1.32 L. For the viscous model, a realizable k-e model was used with standard wall functions. Air as a real gas with the Soave-Redlich-Kwong model was considered as the internal domain in the simulation. The moving water column is not considered for computational simulations as it is not the area of interest. All the boundary conditions are given as a wall boundary condition with a constant temperature of 298 K. The inlet boundary condition is a water interface while the walls were specified with the polycarbonate material properties. The air was initialized with an atmospheric pressure condition. Similar to previous literature modeling the liquid piston [22], a pressure-implicit splitting operator (PISO) was used for the pressure-velocity coupling. The transient formulation used a 1st-order implicit method. The spatial discretization for the density, momentum, and energy are discretized using a 2nd order upwind scheme. Gravity is enabled to act on the negative x-axis. The gradient terms are discretized using a Green-Gauss Node Based method. These methods used in Fluent are robust and approach stable solutions.

As the physical domain compresses due to the movement of the liquid piston, the mesh deforms. This movement of the liquid piston is accomplished by creating a dynamic mesh movement through a user-defined function (UDF) which specifies the velocity of the piston with flow-time. The dynamic mesh deforms using a layering technique where the moving boundary either collapses the layer or merges the adjacent layer with the next layer. As the simulation proceeds and the boundary moves from one position to another the height of the cell layers decreases based on a collapse factor α_c and the ideal cell height h_{ideal} . The computational mesh consists of 12000 tetrahedral cells. The 2D mesh showing the movement of the piston is shown in figure 4.2a and 4.2b for consecutive time-steps.

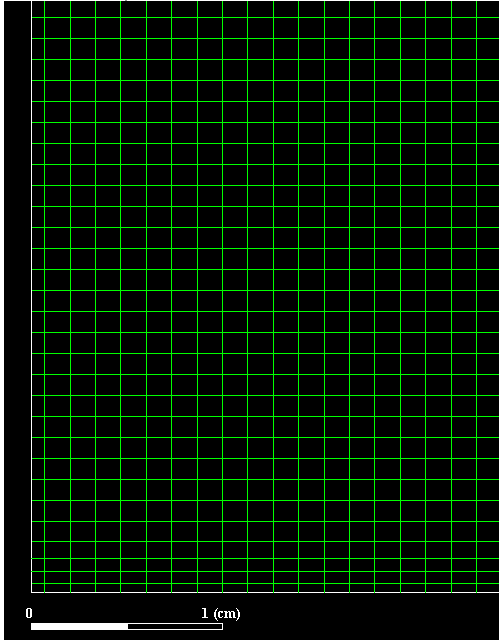


Figure 4. 2a: Mesh at Time $T=0.885s$

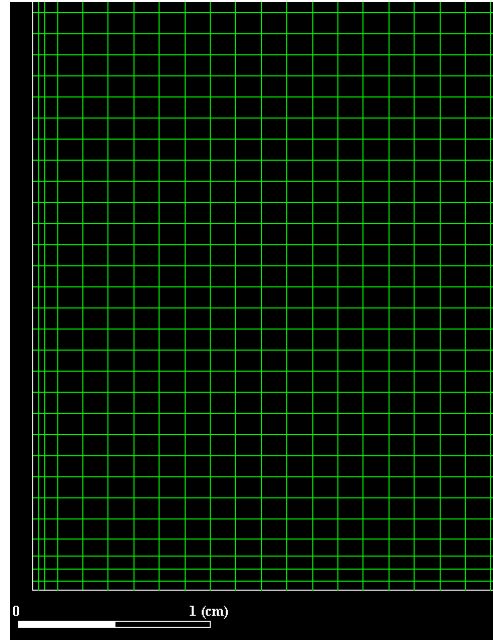


Figure 4. 2b: Mesh at Time $T=0.913s$

Since the compression time is varied from 3s – 5s, the velocity of the liquid piston differs for each case. From the experimental location values, and the volume of the water driven into the chamber, the velocity of the liquid piston is calculated. From these velocity values, using MATLAB the velocity profiles are obtained and further used in the UDF to move the liquid piston. Figures 4.3, 4.4, 4.5 depict the velocity profile for the compression stroke from 5s to 3s respectively.

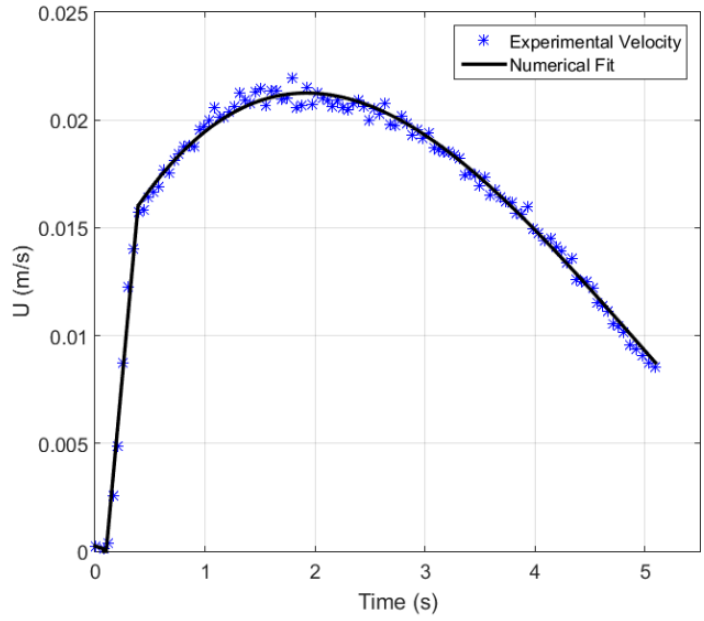


Figure 4. 3: Velocity Profile for 5s compression stroke time (30 psi air source pressure)

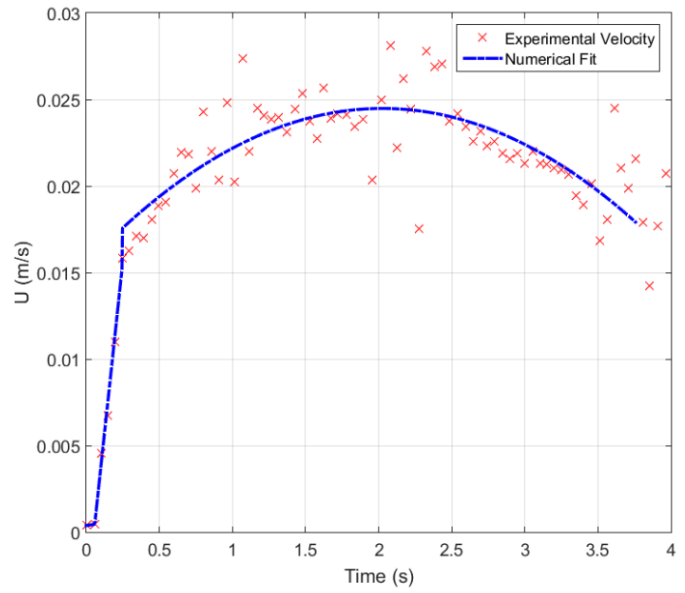


Figure 4. 4: Velocity Profile for 4s compression stroke time (50 psi air source pressure)

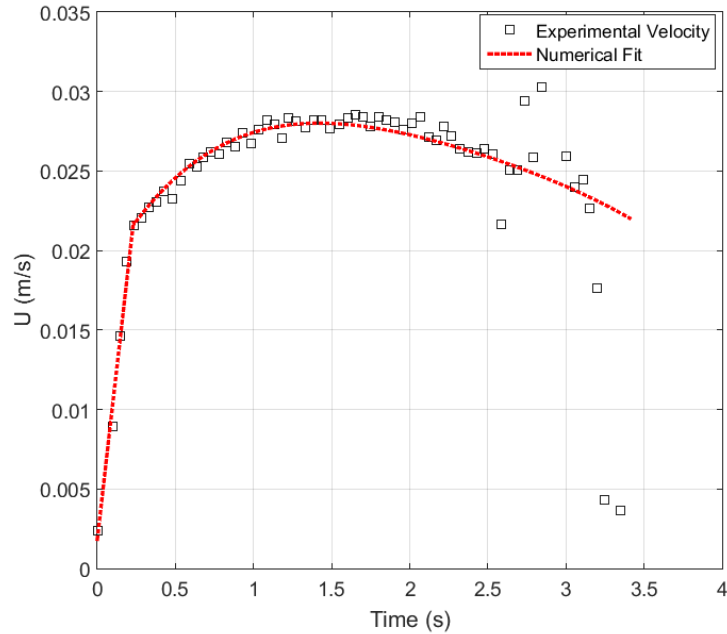


Figure 4. 5: Velocity Profile for 3s compression stroke time (80 psi air source pressure)

Previous studies have used both a constant velocity and a variable velocity for driving the liquid piston [33]. For the 3D simulations as well, the same velocity profiles corresponding to each compression time are used. To monitor the internal properties during the simulations, a volume-averaged pressure and volume-averaged temperature conditions are used. Since the domain is homogenous, a volume-averaged pressure gives an accurate representation of the pressure in the domain. As for the temperature, a volume-averaged value along with the point-location temperature is described in the following sections.

4.2 3D Simulation Setup

The 3D simulations have a similar setup for cases without any spray injection. The cylindrical geometry created in ANSYS ICEM-CFD is shown in figure 4.6, while figure 4.7 shows the geometry at the end of the compression stroke.

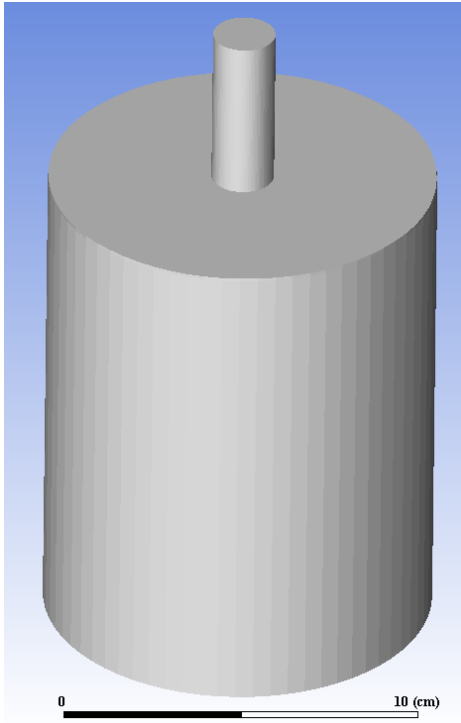


Figure 4.6: 3D Cylinder Geometry at the start of compression

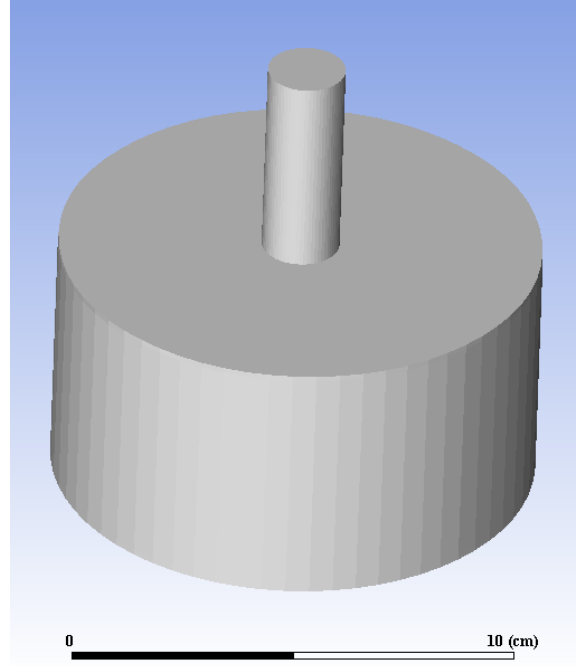


Figure 4.7: 3D Cylinder Geometry at the end of compression

The 3D setup was compared to the 2D setup for cases without spray injection and the results are presented in the further sections. To validate grid-independence of the mesh, coarser and finer meshes were also created. The mesh details are mentioned in table 4.1.

Table 4. 1: Mesh Specifications

| Mesh Type | No. of elements | Quality | Skewness |
|---------------|-----------------|---------|----------|
| Coarse Mesh | 148800 | 0.715 | 0.2846 |
| Moderate Mesh | 300696 | 0.711 | 0.2883 |
| Fine Mesh | 460785 | 0.715 | 0.2843 |

For the 3D simulations with spray injection, two additional models are used in the simulation. First, the species model is set up with the species transport equations for an air mixture comprising of Oxygen (O_2), Nitrogen (N_2), and water vapor (H_2O). Instead of the real gas equation used in the 2D simulations, an ideal gas equation was used for the air mixture. Numerical simulations of compression without spray injection for 2D and 3D geometries with ideal gas and real gas showed minimum variation, therefore ideal gas laws were used. Also, since the simulations with spray injection are computationally expensive, using ideal gas equations reduced the computation time for the simulations.

Next, the Discrete Phase Model (DPM) is used for injecting the droplets using a full-cone nozzle. The droplets are assumed as particles in the simulation and hence are simulated using a Lagrangian-Eulerian method. In this method, the continuous phase (air mixture) is solved using the Eulerian equations and the discrete phase (droplets) are treated as spherical particles and solved using Lagrangian equations. Since the droplets absorb the heat of compression and energy transfer occurs, a two-way interaction is enabled. A coupled heat-mass solution for droplets is used for the mass, momentum, and energy interaction. The injection properties from the dpm model in Fluent are shown in figure 4.8.

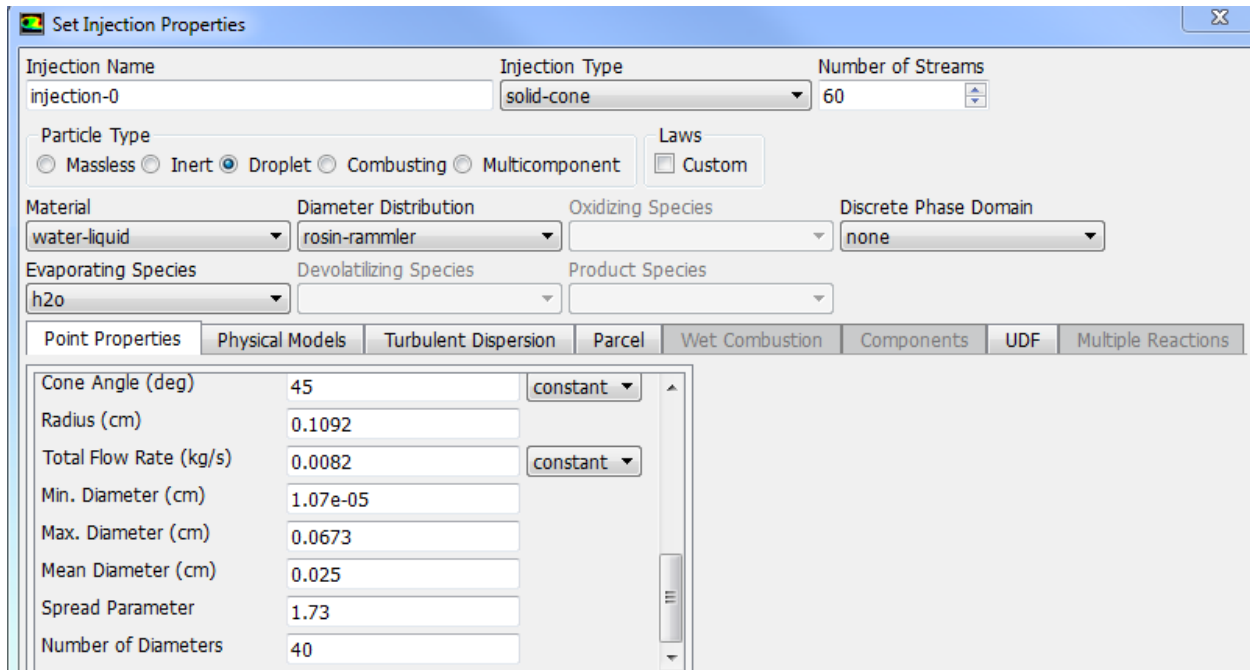


Figure 4. 6: Injection properties for DPM for 90° spray angle and 10 psi injection pressure

A solid cone model with Rosin-Rammler distribution is used with the position of injection, temperature, velocity, nozzle properties, and diameter distribution required as inputs. These point properties are obtained from the manufacturer dataset for the nozzles. The solution methods used in the 2D simulation are also used for the 3D simulations. However, the under-relaxation factors are reduced to achieve numerical stability. The DPM boundary conditions for the inlet and outlet is given as an escape boundary condition, while the wall is set up as a reflective surface. The species boundary condition is given as a zero diffusive flux for the outlet and the wall, and at the inlet, the water vapor mass fraction is specified as a constant value of zero. The droplet velocities for the different nozzle types studied are mentioned in table 4.2.

Table 4. 2: Droplet parameters for numerical simulations

| Nozzle Type | Injection Pressure (psi) | Nozzle Diameter (in) | Flowrate(Gpm) | Velocity(Q/A) (m/s) | DV0.5 (μm) | N – factor(dpm) |
|-------------|--------------------------|----------------------|---------------|---------------------|------------|-----------------|
| 90 Deg | 10 | 0.043 | 0.13 | 8.754 | 250 | 1.730 |
| 90 Deg | 30 | 0.043 | 0.218 | 14.680 | 170 | 1.909 |
| 90 Deg | 50 | 0.043 | 0.278 | 18.720 | 140 | 2.042 |
| 60 Deg | 30 | 0.043 | 0.218 | 14.680 | 190 | 1.966 |
| 120 Deg | 30 | 0.043 | 0.218 | 14.680 | 150 | 1.899 |

Few assumptions were used for the simulation of spray injection during the liquid piston compression process. As mentioned earlier, the droplets are assumed to be point spheres or particles in the dpm setup. From the experimental results, it was observed that the flow rate of spray injection reduced with the progress of the compression stroke, which consequently reduced the velocity of the spray injection. However, it is assumed that the velocity of spray injection is a constant. At higher pressures, the vaporization temperature of water varies along with the latent heat of vaporization. However, this phenomenon is not considered in the current cases. For simulation of liquid piston compression during spray injection, the inlet piston velocity was considered as a constant average value instead of a variable velocity. This was done to reduce the computational time of the simulation.

CHAPTER 5: CFD Validation and Results

In this chapter, the CFD simulations for a liquid piston compression process are validated. The 2D and 3D simulations for liquid piston compression without spray injection are compared with the experimental results from Chapter 3. Finally, the results for the liquid piston compression process with and without spray injection are described.

5.1 Liquid Piston Compression-Numerical Validation

To validate the CFD simulations for a liquid piston compressor, a reference simulation by Zhang et al. was simulated [22]. In this paper, they simulate a liquid piston compression process of air in a 2D axisymmetric computational domain. The computational domain is a long thin tube of a diameter of 0.0035 m and a length of 0.3 m shown in figure 5.1.

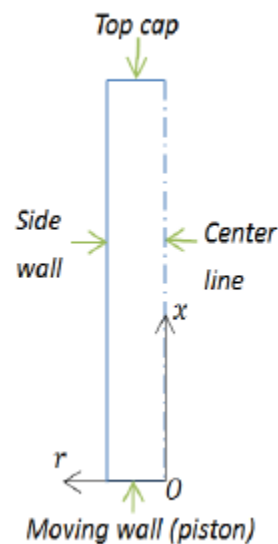


Figure 5. 1: Computational Domain for 2D Axisymmetric Mesh [22]

The walls are set at a constant temperature of 293 K and the initial pressure is set at atmospheric pressure. Since the domain is a 2D axisymmetric domain, the governing equations are set up in the cylindrical coordinate system in ANSYS Fluent. A transient simulation is set up using a 1st order implicit scheme. The domain is discretized using 400 elements over the length and 20 elements in the radial direction. The velocity of the liquid piston used is Vel5, that is 0.6 m/s and the air is compressed by a pressure ratio of 10. The Vel5 case is validated with the current results. To validate the numerical setup, the temperature-volume and heat flux-time plots are compared. The temperature and pressure values in the reference paper are volume-averaged parameters.

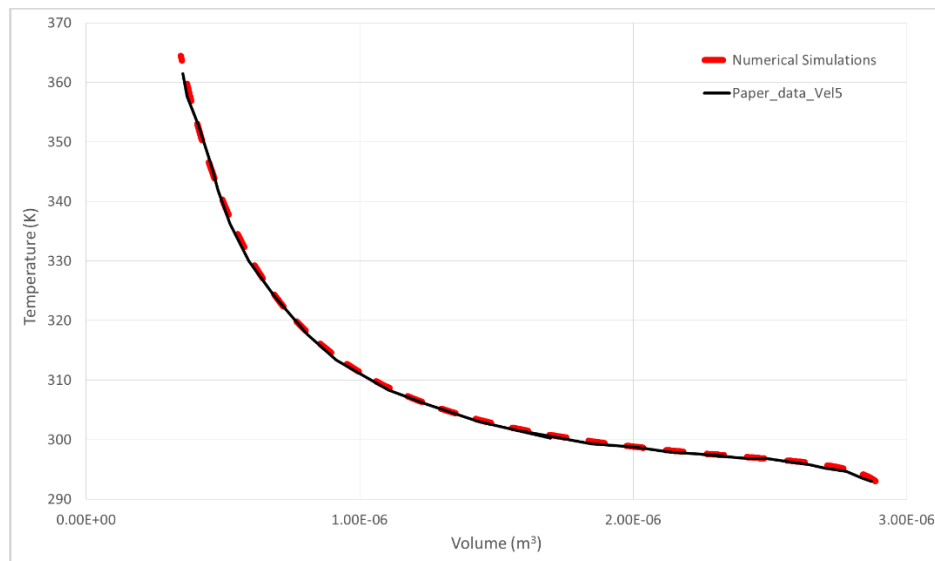


Figure 5. 2: Temperature - volume plot

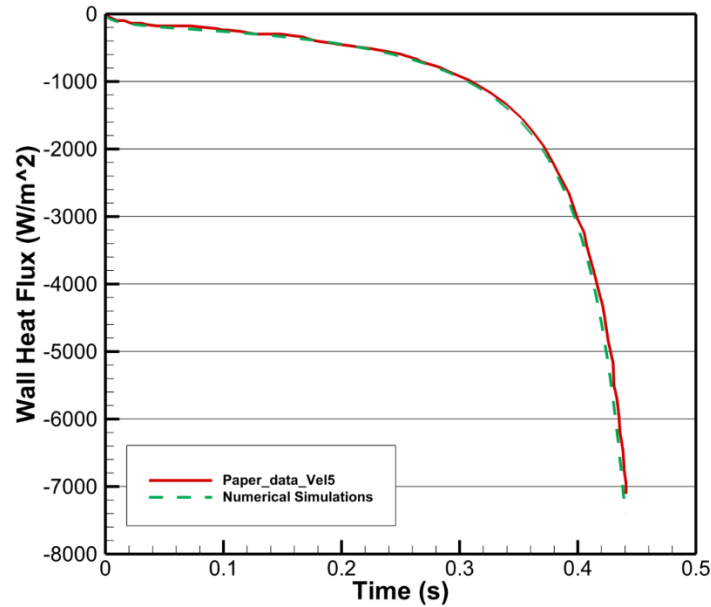


Figure 5. 3: Wall Heat Flux- time plot

The temperature vs volume plot is shown in figure 5.2 and the wall heat flux vs time plot is shown in figure 5.3. The temperature and heat flux plots have a perfect match which suggests that the Fluent setup is acceptable for further simulations.

5.2 Grid Independence Study of 3D Mesh

The numerical results for compression without spray injection are compared with the experimental results to validate the model. The compression cycles corresponding to 30, 50, 80 psi air source pressures are studied (5s-3s compression respectively). In all the simulations only a single compression cycle is studied instead of continuous compression cycles. The grid independence test is performed for the 5s compression stroke time and is presented along with the 2D comparison. The results are shown in the Pressure-time plot in figure 5.4. Pressure from the 3D simulation for the coarse, moderate, and fine mesh are plotted along with the 2D simulation

result. It can be observed that the pressure curve remains the same irrespective of the 3D mesh selected. The 3D simulations show a higher pressure than observed in the 2D setup.

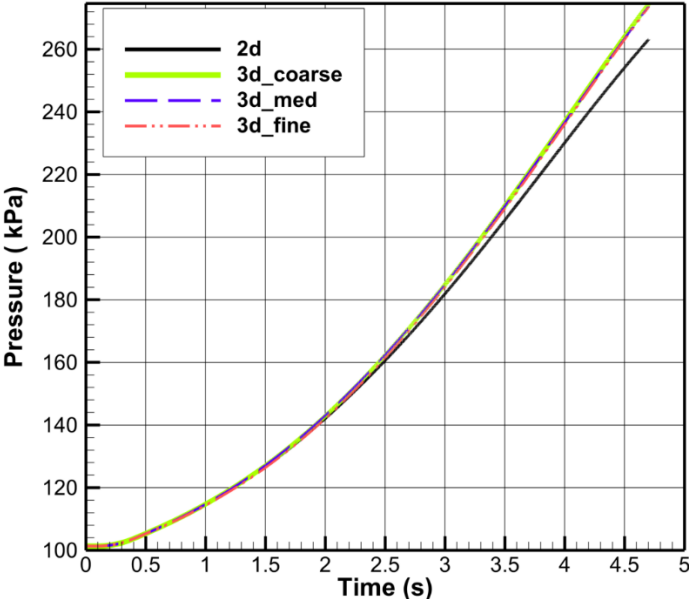


Figure 5. 4: Pressure - time plot for 2D and 3D simulations for 4.7 s compression

For comparing the temperature curves between the 2D and 3D simulations, the volume-averaged temperature and the vertex temperature corresponding to the thermocouple location in the experiment are plotted. Figure 5.5 shows the volume-averaged temperature vs time plot.

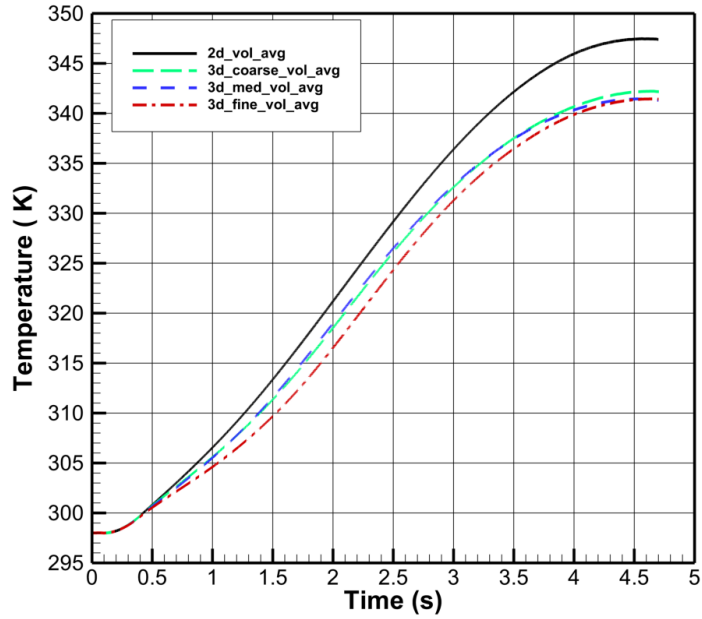


Figure 5. 5: Volume-averaged temperature– time plot for 2D and 3D simulations for 4.7 s compression

It is observed that the temperature for the 2D setup is around 5 K higher than the 3D simulation cases. The 3D simulations for the coarse, moderate, and fine mesh follow a similar curve profile during the compression and vary slightly during the process. The final temperatures reached at the end of compression for 3D cases differ less than 1 K. From the pressure and temperature plots, it can be observed that the simulations are grid-independent and hence, for the rest of the simulations, only a moderate 3D mesh is considered. This is to have accurate simulations while not being too computationally expensive.

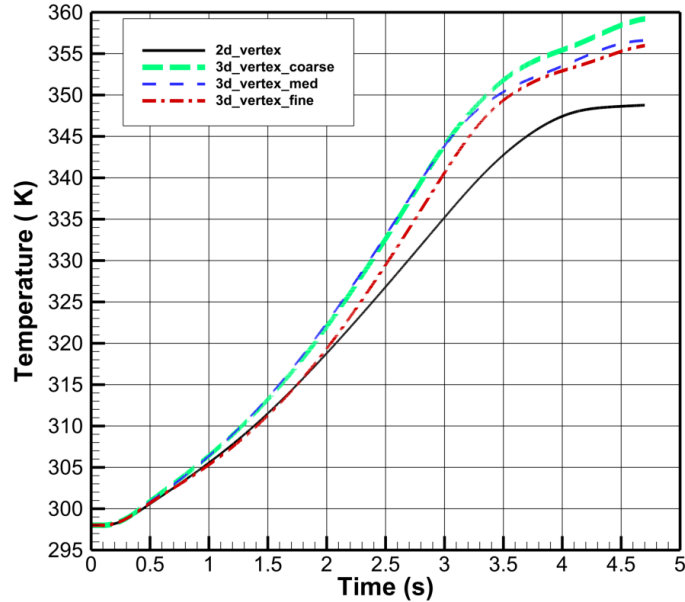


Figure 5. 6: Vertex-averaged temperature – time plot for 2D and 3D simulations for 4.7 s compression

The vertex temperature for the 2D and 3D simulations are plotted in figure 5.6. It can be observed that the vertex temperatures are higher than their corresponding volume-averaged temperatures. The 3D cases have a higher vertex temperature than the 2D simulation by around 8-10 K. Between the 3D cases themselves, a small variation is observed at the end of the compression stroke. Unlike the volume-averaged temperature results, where the 2D temperature was higher than the 3D simulation temperatures, for the vertex temperature, the trend is reversed for the vertex temperature, while the 3D simulations showed a higher temperature value than the 2D setup.

5.3 Comparison of 2D and 3D Simulations for Liquid Piston Compression

For the 3.6s compression process (50 psi air source pressure), the pressure and temperature plots are shown below. Figure 5.7 shows the pressure-time plot and figure 5.8 shows the temperature-time plot. Similar to the 5s compression stroke time, the 3D simulation predicted a

higher pressure at the end of compression compared to the 2D simulation. The temperature for the 3D case is lower than the 2D case by 5-6 K and reaches a maximum of 348 K.

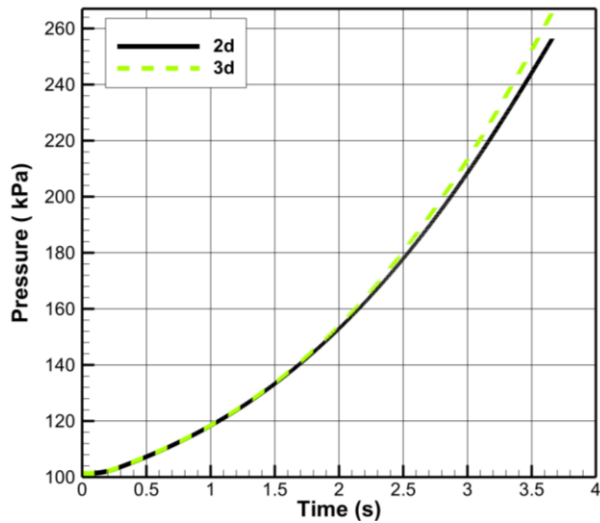


Figure 5. 8: Pressure-time plot for 3.6s compression for 2D and 3D simulations

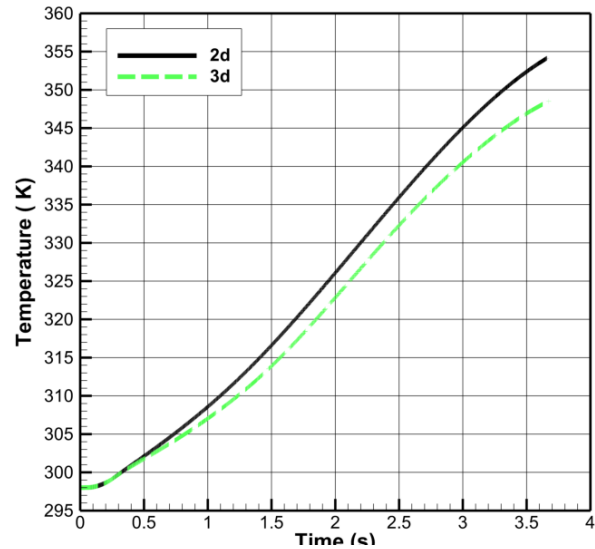


Figure 5. 7: Temperature-time plot for 3.6s compression for 2D and 3D simulations

The 3s compression stroke time shows similar results to the previous plots. The temperature-time and pressure-plot are shown in figure 5.9 and 5.10 respectively.

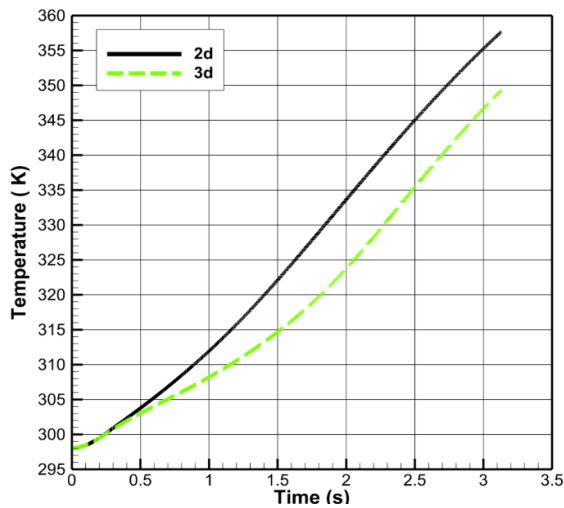


Figure 5. 9: Temperature-time plot for 3.1s compression for 2D and 3D simulations

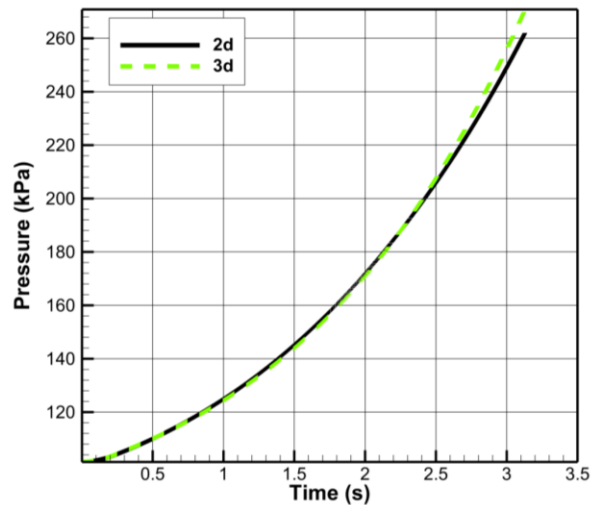


Figure 5. 10: Pressure-time plot for 3.1s compression for 2D and 3D simulations

5.4 Numerical Simulation Validation without Spray Injection

Next, the results are compared to the experimental observations for the compression process without any spray injection for a fast compression stroke time of 3.13s. Figures 5.11 and 5.12 compare the experimental data of pressure and temperature for a 120° spray angle without any spray injection to the 2D and 3D simulation results, respectively. The pressure curve in figure 5.11 closely follows the experimental data. This validates the pressure component in the numerical simulations. The figure also plots the 3D simulation results for a constant velocity which was used for simulations with the spray injection setup. In the simulations with spray injection, a constant velocity was used to reduce the computational load on the system. Though the trends are similar, towards the end of compression the constant average velocity is higher than the variable velocity values. This tends to increase the error at the end of compression.

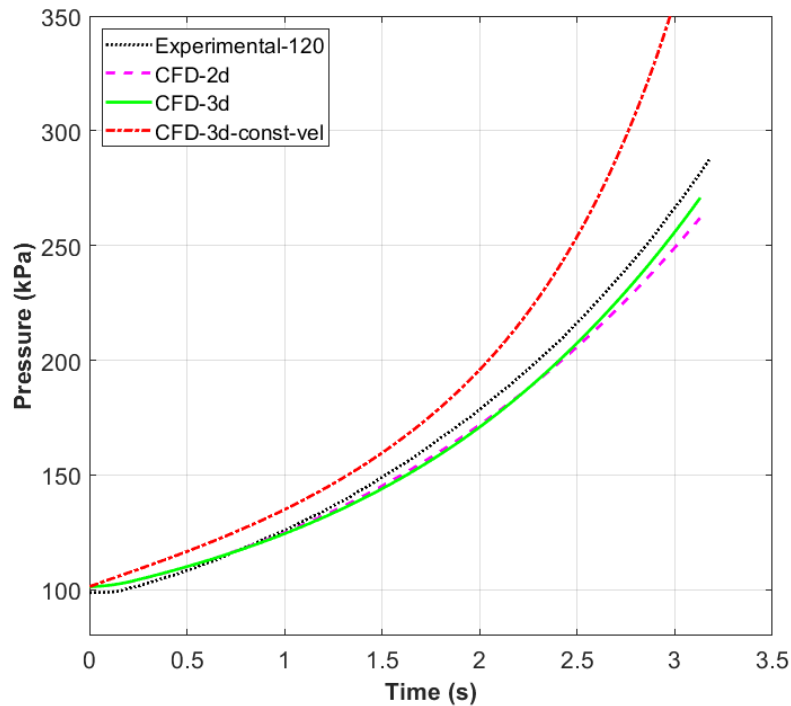


Figure 5. 11: Comparison of experimental and computational pressure results for a 3.13s (fast) compression cycle

The temperature comparison between the experimental and the numerical results are shown in figure 5.12. Compared to the experimental observations, the 2D and 3D temperature results over predict the data considerably. The 3D temperature results are within a 15 K difference of the experimental measurements during the compression process. In the above plots, it can be observed that while the pressure matched reasonably well with the experimental results, the temperature data does not match so accurately.

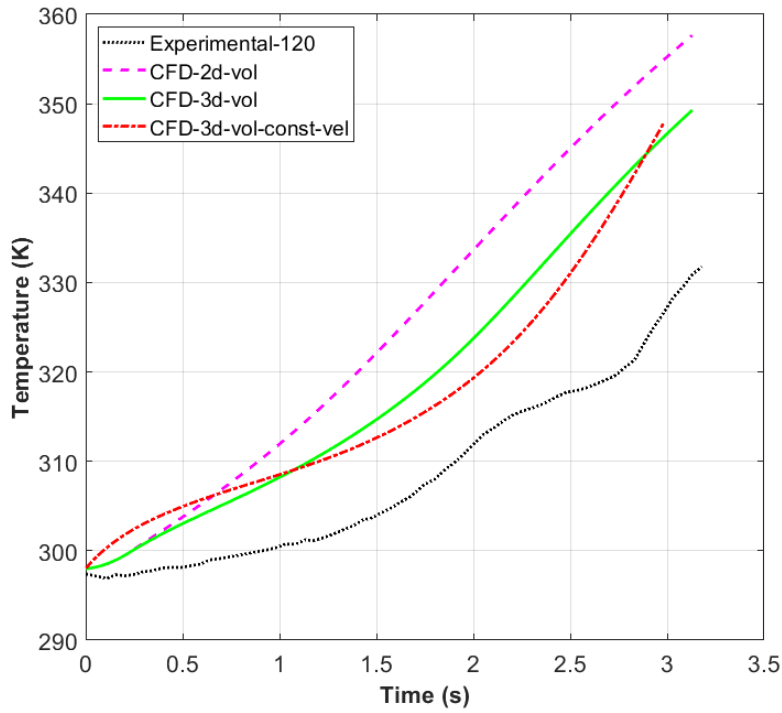


Figure 5. 12: Comparison of experimental and computational temperature results for a 3.13s (fast) compression cycle

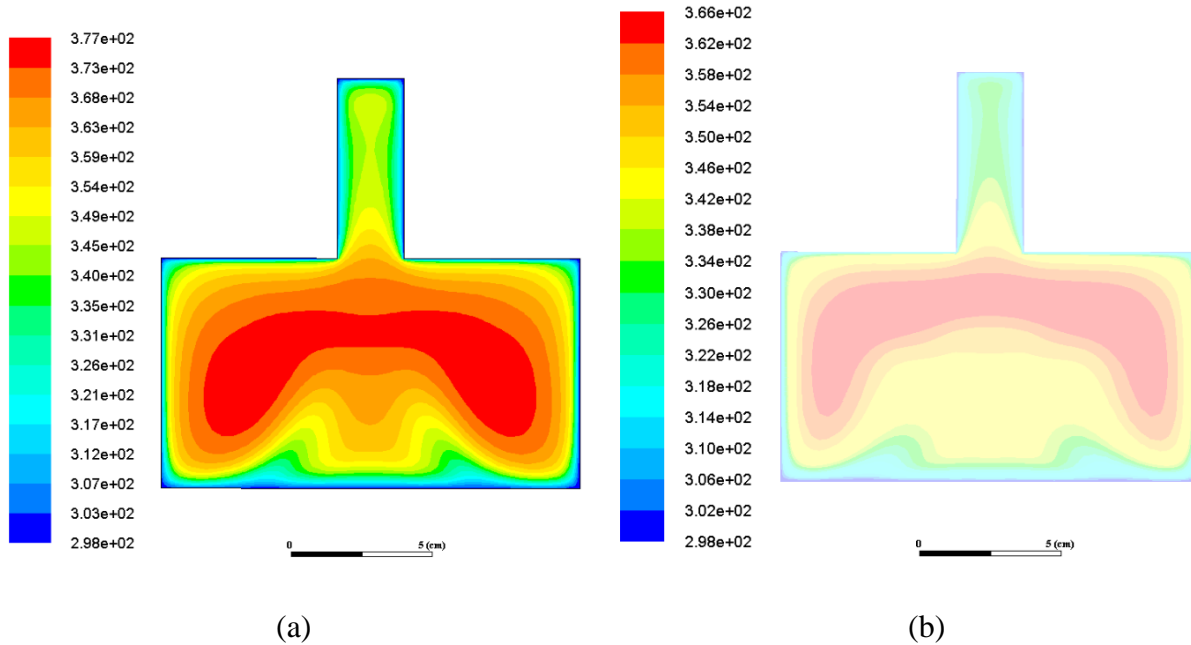


Figure 5. 13: Temperature contours for a 3.13s (fast) compression cycle in (a) 2D simulation and (b) 3D simulation

The temperature contours for the 2D and 3D simulations for a 3.13s compression are shown in figure 5.13a and figure 5.13b, respectively. For the 3D simulation, the mid-plane section was used for plotting the temperature contours. The temperature contours are similar for both the simulations, however, the maximum temperature in the 2D simulation is higher than in the 3D simulations. The 2D simulations take approximately 4-5 hours to run on a parallel system while the 3D simulations take around 24-30 hours with the same parallel system. Even though from a computational cost perspective, the 2D simulations are faster, the 3D simulations are more accurate than the 2D simulations for the liquid piston compression.

It may be noted that the volume-averaged temperature has been used in the above plots. This discrepancy between experimental and numerical results may be due to several factors combined. First, in the experimental setup, the thermocouples are covered by a protective covering to avoid direct interaction with the spray nozzle. This may also create a wall effect and the

thermocouples may not accurately read the actual temperature. Lekić performed numerical and experimental research on heat transfer in helium gas springs and observed that the gas temperature readings depended on the operating rate of the piston. It was observed that on increasing the speed of the piston the amplitude of the gas temperature dampened out while the mean gas temperature increased and observed that the gas temperature readings depended on the operating rate of the piston. It was observed that on increasing the speed of the piston the amplitude of the gas temperature dampened out while the mean gas temperature increased. This was attributed to the effect of the sensor's thermal constant which leads to the measured signal not following the actual gas temperatures [34].

Another possible reason could be the incorrect volume of the air domain for the numerical modeling. The additional air volume in the pressure transducer volume and the solenoid valves are accounted for the model, however, their accuracy may affect the volume-averaged temperature in the simulation. It may also be possible that, since the thermocouples are designed to operate at atmospheric conditions and not for high-pressure applications, a repeated cyclic operation might have damaged the thermocouple sensor and its accuracy. The heat transfer models in the numerical setup could also be improved to carefully account for the heat transfer in the compression chamber.

5.5 Computational Results for Liquid Piston Compression with Spray Injection

In this section, numerical results are presented for a fast compression process (3s) with a 90° spray nozzle and a 10 psi injection pressure. Table 5.1 lists the droplet parameters for this injection process.

Table 5. 1: Droplet Properties for Fluent Simulation

| Droplet Temperature (K) | Droplet Velocity (m/s) | Half-cone Angle (°) | Min. Diameter (cm) | Max. Diameter (cm) | Mean Diameter (cm) | Spread Parameter (n) |
|-------------------------|------------------------|---------------------|--------------------|--------------------|--------------------|----------------------|
| 298 | 8.754 | 45 | 0.000107 | 0.0673 | 0.025 | 1.73 |

These parameters are used in the Discrete Phase Model of the Fluent simulation. The droplet velocity was calculated using the flow rate through the nozzle and the nozzle cross-section area. The diameter distribution was obtained from the manufacturer’s droplet distribution data and the spread parameter (n) was calculated using this distribution. To resolve the fine droplets, the mesh density was increased to 386988 elements. The volume-averaged pressure is compared with the experimental pressure measurement and is shown in figure 5.14. In figure 5.14, the CFD model over-predicts the pressure during the compression process. This deviation reaches a maximum value of 16% near the end of the compression stroke. Primarily this variation is due to the constant velocity profile used for the liquid piston movement. This variation in the pressure value may also be due to the smaller volume of the numerical domain which results in a larger pressure value. Numerical instability and poor convergence may also be responsible for the error near the end of the compression cycle. Since the error begins at the start of the compression, this error propagates during the simulation process.

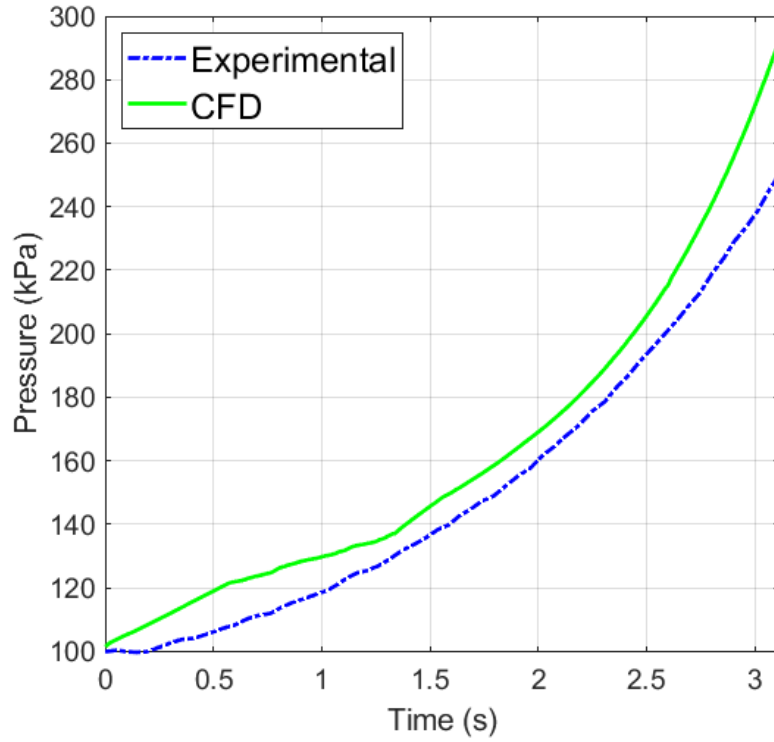


Figure 5. 14: Comparison of experimental and computational pressure results for a fast (3s) compression cycle

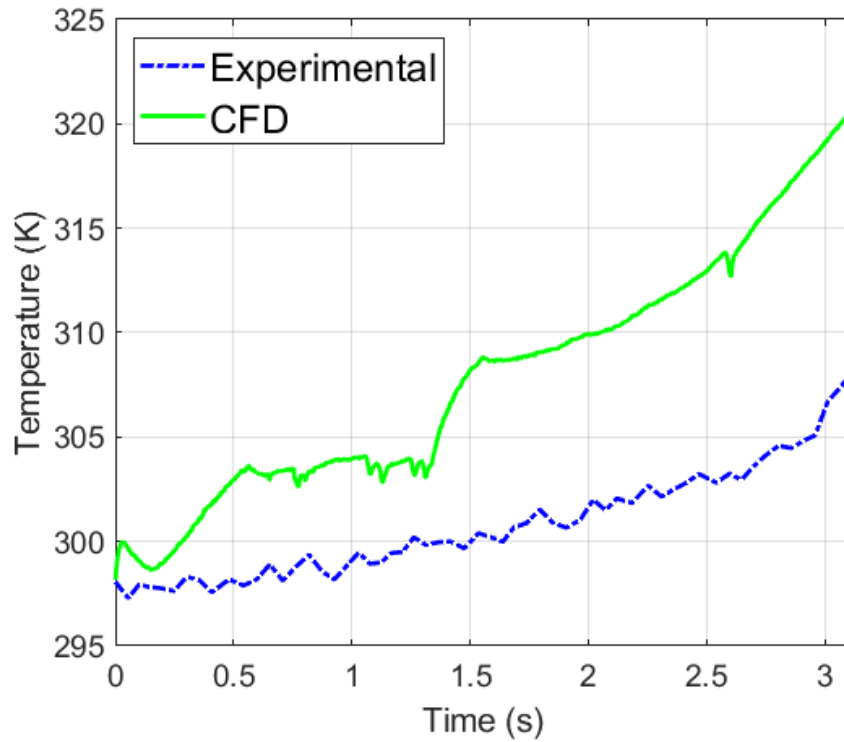


Figure 5. 15: Comparison of experimental and computational temperature results for a fast (3s) compression cycle

Figure 5.15 compares the temperature-time plot for the experimental and CFD simulation. The CFD simulation curve is a curve-fit model from the numerical temperature values. Even though the temperature profiles do not match properly, the temperature values for the experimental and numerical simulations during the compression process are within 10-12 K of each other. The trends for the temperature profiles are similar in the experimental and numerical cases.

The injected particles have a high inlet velocity of 8.754 m/s during the compression process due to which the droplets reach the liquid piston surface in the order of milliseconds. Figure 5.16 shows the droplet residence time in the compression chamber at end of compression. The mid-plane of the compression chamber is shown for reference with the location of the tip of the nozzle. The droplets are sized by their diameter and colored according to the particle residence time. The heavier particles do not deviate from their motion and fall onto the water surface while maintaining the full-cone structure. Few droplets which are smaller in diameter and are reflected by the wall (in red) remain in the compression domain for a longer period.

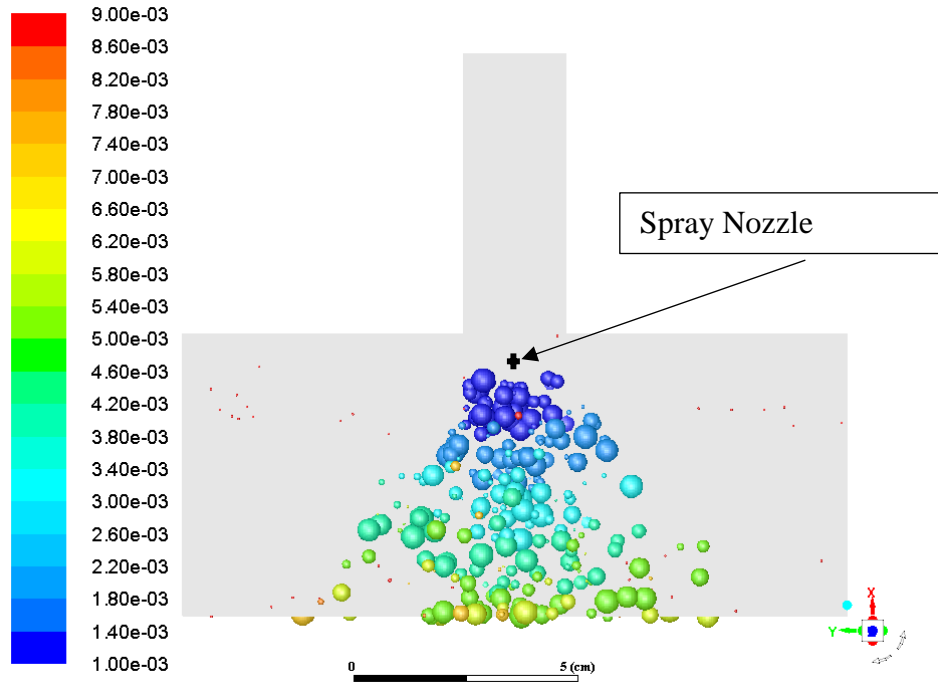


Figure 5. 16: Residence time of droplets in the chamber at the end of compression

Figure 5.17 shows the droplet temperature at the end of the compression period in the computational domain. The droplets are given a fixed temperature of 298 K at the injection point, however, some of the droplets absorb the heat during the compression process which increases the range of the temperature to 305 K. In figures 5.16 and 5.17, the droplets are scaled 5-6 times their actual size for visual representation. All the droplet diameters are scaled uniformly in the domain.

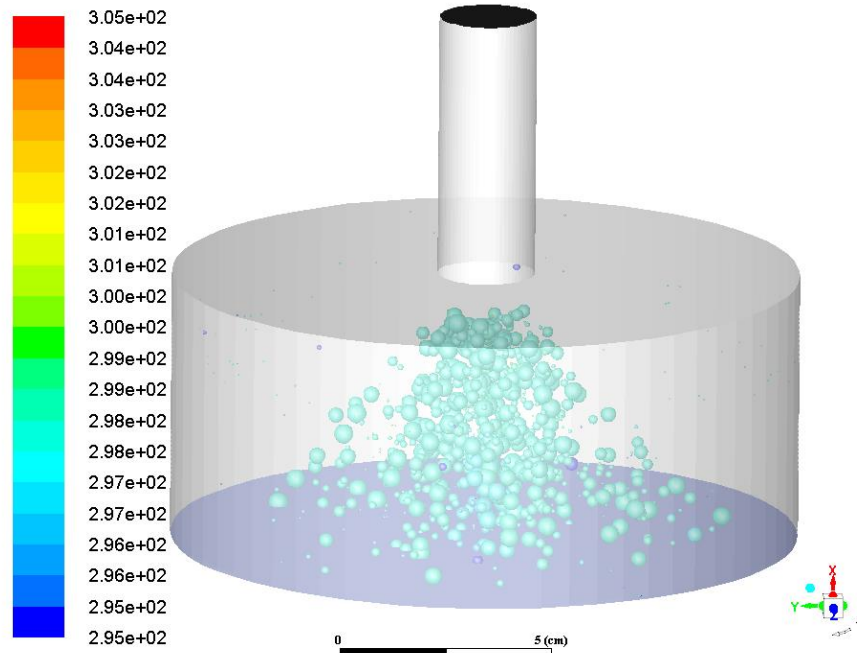


Figure 5. 17: Droplet temperature (K) in the liquid piston chamber at the end of compression

During the compression process, the droplets can either hit the water surface (inlet piston surface) or the walls or escape through the outlet at the top. They may also evaporate during the compression process. Table 5.2 lists a summary of the droplets fate at the end of compression. Most of the droplets hit the water surface and escape through the liquid piston surface. A very small percentage of the droplets remain in the domain after the compression process (around 0.0014 %) while around 1.13% of the droplets evaporate.

Table 5. 2: Droplet Summary at end of compression process (3.1s)

| Fate Mass (kg) | Initial | Final | Change |
|----------------------------|-----------|-----------|------------|
| Incomplete | 3.481e-07 | 2.452e-07 | -1.029e-07 |
| Evaporated | 2.870e-04 | 0.000e+00 | -2.870e-04 |
| Escaped - Zone 9 (Inlet) | 2.511e-02 | 2.499e-02 | -1.219e-04 |
| Escaped - Zone 10 (Outlet) | 6.372e-08 | 6.324e-08 | -4.730e-10 |
| Net | 2.540e-02 | 2.499e-02 | -4.091e-04 |

CHAPTER 6: Numerical Simulation Results and Discussion

Different sets of numerical simulations were performed to observe the flow-field and droplet characteristics. The effect of injection pressure was studied for a 90° spray angle and a fast compression process of around 3s. Different injection pressure of 10 psi, 30 psi, and 50 psi were studied. Increasing the injection pressure makes the spray finer and decreases the mean droplet diameter. The velocity of spray injection increases as well.

Figure 6.1 shows the wall heat flux for different injection pressures during the compression process.

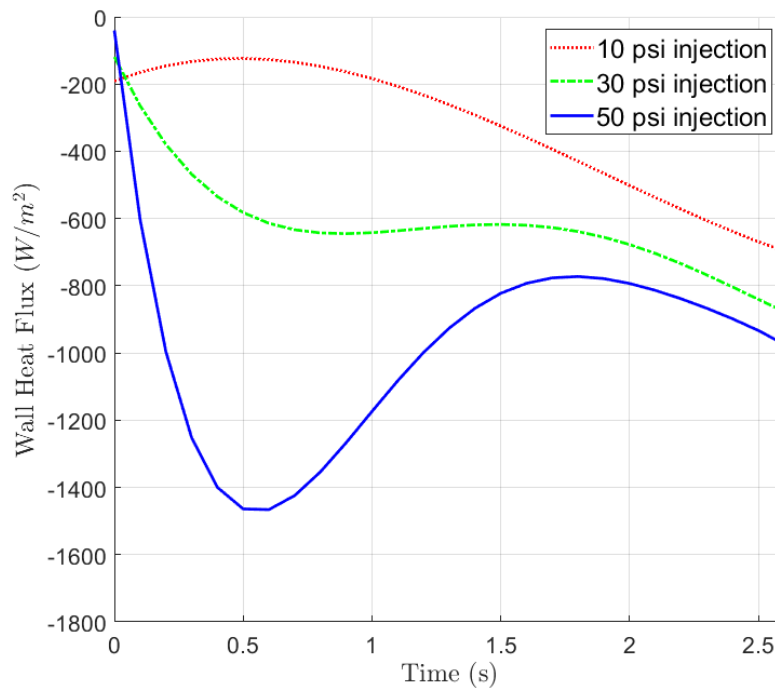


Figure 6. 1: Wall heat flux for different injection pressures

It is observed that the wall heat flux has a negative value for all the injection cases. This is simply due to the direction of heat flow being out of the wall. At the start of compression, the 50 psi injection pressure has the maximum wall heat flux which indicates a higher spray cooling

effect. A trend is observed such that with increase of injection pressure the wall heat flux increases as well. With the progress of the compression stroke, the heat flux for the different injection pressures converge to around a constant value between 700-1000 W/m². This shows that towards the end of the compression stroke, the effect of the injection pressure diminishes. As the compression chamber is saturated with the water droplets, the maximum heat flux or critical heat flux (CHF) is reached for the all the different cases.

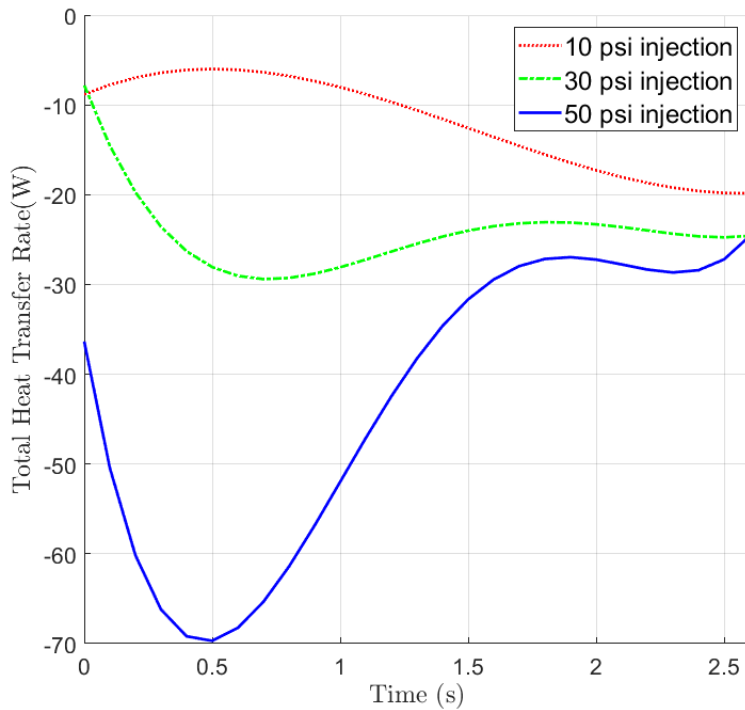


Figure 6. 2: Total heat transfer rate for different injection pressures

A similar trend was observed with the total heat transfer rate from the wall as shown in figure 6.2. The maximum heat transfer is with 50 psi spray injection pressure. For the 10 psi injection pressure, the heat transfer rate increases during the compression process while for the 50 psi injection pressure, the heat transferred decreases. However, they all converge to approximately the same value.

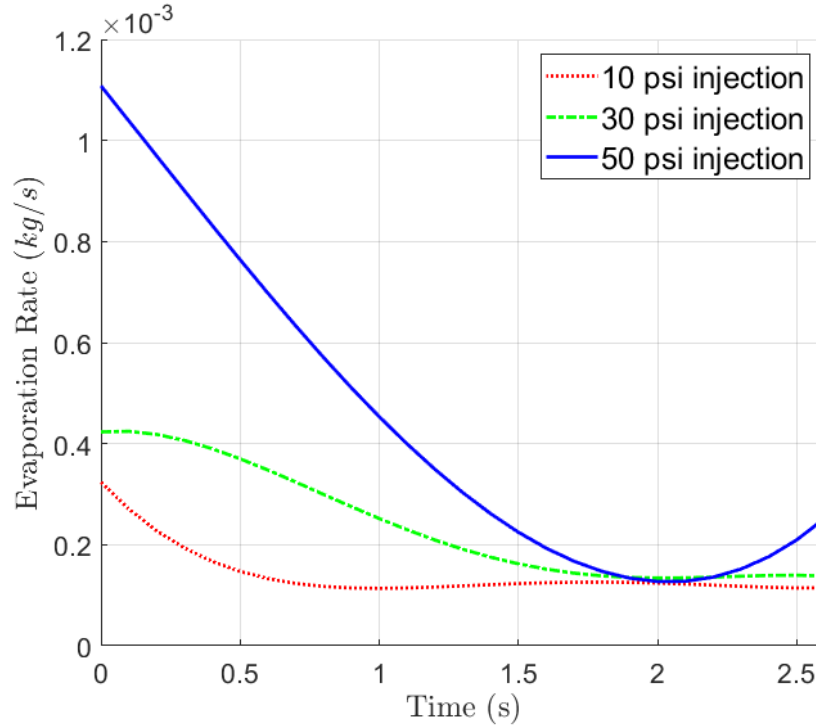


Figure 6. 3: Evaporation rate during compression process for different injection pressures

The evaporation rate is shown in figure 6.3 for different spray injection pressures. The evaporation rate is highest with 50 psi injection pressure. Increasing the injection pressure leads to a finer droplet diameter and a higher mass loading. However, the evaporation rate converges to a constant value after a certain time.

From the above plots, it is observed that a higher injection pressure is beneficial at the start of the compression process, however towards the end of compression, the injection pressure does not play a major role in improving the heat transfer. From the experimental results, the increase in injection pressure shifted the polytropic curve towards a near-isothermal condition, though the polytropic index varied marginally at higher injection pressures. It should be noted that for the simulations, a constant flow rate was given instead of a variable flow rate as used in the experimental setup. This may affect the heat transfer rate and the temperature reduction towards

the end of compression as the flow rate actually reduces during the experimental investigations. The wall flux and heat transfer rate may not converge to a certain value, however, it is expected that the trends would remain the same.

Since each numerical simulation with spray injection in the liquid piston compressor takes around 15-20 days depending upon the number of droplets injected per time-step, velocity of droplets, and mesh resolution, only the effect of injection pressure was studied for the numerical simulations.

CHAPTER 7: Conclusions and Future Work

7.1 Conclusions

The objective of this thesis was to study the temperature reduction occurring during the liquid piston compression process with the use of spray injection as a heat transfer enhancement technique. The effect of different parameters such as compression stroke time, spray injection pressure, and spray nozzle angle were considered in the experimental study. Further numerical simulations were performed to understand the droplet characteristics. Numerical simulations were performed with and without any spray injection during the compression process.

From the experimental study, spray cooling was observed to be effective in temperature reduction during the compression process. The experiments were performed for a compression ratio of 2.5. The effect of the injection pressure on the temperature reduction was studied. It was observed that with increasing spray injection pressure the temperature reduction increased and the polytropic compression process shifted towards near-isothermal conditions. This was reflected in the isothermal efficiency of compression and the polytropic index of compression. Injection of spray even at a low injection pressure of 10 psi resulted in the improvement of isothermal efficiency of compression to 84-86%. Further, higher injection pressures resulted in higher isothermal efficiencies. This incremental improvement in injection reaches a maximum at 94-96%. The polytropic index also shifted from 1.25 without any spray injection to around 1.03-1.05 with spray injection. However, this shift towards near-isothermal conditions and improvement in efficiency comes at the expense of additional spray work. The compression stroke time was also varied from 3s to 5s by varying the air source pressure to the pneumatic cylinder. It was observed that irrespective of the compression stroke time, the temperature with injection of spray remained

around 295-305 K. However, the temperature reduction is higher at a faster compression stroke time since without spray injection a faster compression process reaches a higher temperature.

The experimental investigations were performed for different nozzle angles of 60°, 90°, and 120°. For a given compression stroke time of around 3s and spray injection pressure of 30 psi, increasing the nozzle angle resulted in a lower mean droplet diameter. Though the temperature observed during these experiments were within a 2-3 K difference, the 60°-90° range for spray injection resulted in a lower polytropic index.

Numerical simulations were performed without spray injection for different compression stroke times and the results were compared to the experimental observations. Different compression stroke times were simulated and the results for the pressure and temperature in the domain were within a 15 % error margin. With spray injection, the temperature remained around 305K-310 K, which was observed in the CFD simulations, however the temperature curves did not fit with the experimental results. The effect of the injection pressure was studied numerically for a 90° spray angle and a fast compression process. The wall heat flux and the evaporation rate is higher for 50 psi injection pressure compared to the 30 psi and 10 psi injection pressures. However, towards the end of compression, the evaporation rate reaches a constant value of 0.001 kg/s. Due to this, the wall heat flux also converges within a certain range as no further incremental heat transfer can occur.

Spray Injection was found to be an effective method for temperature abatement during the compression process with higher efficiency obtained with finer droplet diameters and higher injection pressures. The polytropic index of compression and isothermal efficiency of compression were used to quantitatively describe the shift in the polytropic curve to near-isothermal conditions.

Further investigations can be explored for optimization of spray characteristics which are reported in the following section.

7.2 Future Work

To optimize spray cooling in a liquid piston compressor, various parameters can be investigated further. In this thesis, only the compression efficiency was considered instead of the overall end-to-end efficiency of the OCAES system. The following points describe further research that can be considered:

- To generate spray in the compression chamber, an additional pump was used in the experiments along with the hydraulic pump for driving the liquid piston. This accounted for extra pump work. Instead, water can be injected from the top of the compression chamber in the form of a high-pressure spray to achieve the liquid piston movement. The chamber can be sealed at the bottom during the compression cycle so that water from the spray accumulates in the compression chamber leading to a reduction of the air volume. This method could be investigated to study its effectiveness in reducing the additional spray work.
- Nozzle parameters such as diameter of the nozzle and different types of nozzle patterns can be investigated to design an optimized nozzle for spray cooling in a liquid piston compressor. In the current set of experiments, the injection pressure was varied from 10-70 psi. This range could be varied depending on the compression ratio of the compressed air. Higher compression ratios and operating pressures can also be investigated for different spray injection pressures. The angle of the nozzle is also an important parameter which

affects the droplet characteristics and can be investigated further. For a larger compressor unit multi-nozzle spray setups may also be explored.

- The numerical simulations have a lot of assumptions which can be improved to obtain accurate simulations. The simulations assume that the droplets are non-deforming particles, without any droplet breakup or coalescence. Changing this to a deforming droplet model will be a more accurate representation of the actual process. The droplets are injected at a constant velocity instead of a variable velocity corresponding to the actual flow rate. At a high pressure, the vaporization temperature of water changes along with the latent heat of vaporization.
- The numerical simulations could also be performed to achieve a high pressure compression process. In this simulation, even though the number of mesh elements is high and around 600-800 droplets are injected at every time-step, for further accuracy a robust mesh is required with higher number of droplets to simulate the injection process accurately.

REFERENCES

- [1] M. Budt, D. Wolf, R. Span, and J. Yan, "A review on compressed air energy storage: Basic principles, past milestones and recent developments," *Appl. Energy*, vol. 170, pp. 250–268, 2016.
- [2] F. Crotogino, K.-U. Mohmeyer, and R. Scharf, "Huntorf CAES: More than 20 Years of Successful Operation," *Solut. Min. Res. Inst. Spring Meet.*, no. April, pp. 351–357, 2001.
- [3] D. R. Hounslow, W. Grindley, R. M. Loughlin, and J. Daly, "The Development of a Combustion System for a 110 MW CAES Plant," *J. Eng. Gas Turbines Power*, vol. 120, no. 4, pp. 875–883, 1998.
- [4] S. D. Lim, A. P. Mazzoleni, J. Park, P. I. Ro, and B. Quinlan, "Conceptual design of ocean compressed air energy storage system," *Ocean. 2012*, pp. 1–8, 2012.
- [5] C. Qin, E. Loth, P. Li, T. Simon, and J. Van De Ven, "Spray-cooling concept for wind-based compressed air energy storage," *J. Renew. Sustain. Energy*, vol. 6, no. 4, 2014.
- [6] Y. M. Kim, J. H. Lee, S. J. Kim, and D. Favrat, "Potential and evolution of compressed air energy storage: Energy and exergy analyses," *Entropy*, vol. 14, no. 8, pp. 1501–1521, 2012.
- [7] V. C. Patil and P. I. Ro, "Energy and Exergy Analysis of Ocean Compressed Air Energy Storage Concepts," *J. Eng.*, vol. 2018, pp. 1–14, 2018.
- [8] S. Succar and R. Williams, "Princeton Environmental Institute PRINCETON UNIVERSITY Energy Systems Analysis Group Compressed Air Energy Storage : Theory , Resources , And Applications For Wind Power Acknowledgments," *Princet. Environ. Inst. Rep.*, vol. 8, no. April, p. 81, 2008.
- [9] S.-I. Inage, "Prospects for Large-Scale Energy Storage in Decarbonised Power Grids," *Int.*

- Energy Agency*, p. 90, 2009.
- [10] D. Zhou *et al.*, “Technology Roadmap,” *SpringerReference*, vol. 92, no. January, p. 24, 2013.
- [11] C. Zhang, P. Y. Li, J. D. Van De Ven, and T. W. Simon, “Design analysis of a liquid-piston compression chamber with application to compressed air energy storage,” *Appl. Therm. Eng.*, vol. 101, pp. 704–709, 2016.
- [12] R. P. Klüppel and J. M. Gurgel, “Thermodynamic cycle of a liquid piston pump,” *Renew. Energy*, vol. 13, no. 2, pp. 261–268, 1998.
- [13] J. D. Van de Ven and P. Y. Li, “Liquid piston gas compression,” *Appl. Energy*, vol. 86, no. 10, pp. 2183–2191, 2009.
- [14] C. Qin and E. Loth, “Liquid piston compression efficiency with droplet heat transfer,” *Appl. Energy*, vol. 114, pp. 539–550, 2014.
- [15] B. Yan, J. Wieberdink, F. Shirazi, P. Y. Li, T. W. Simon, and J. D. Van de Ven, “Experimental study of heat transfer enhancement in a liquid piston compressor/expander using porous media inserts,” *Appl. Energy*, vol. 154, pp. 40–50, 2015.
- [16] M. Saadat, P. Y. Li, and T. W. Simon, “Optimal trajectories for a liquid piston compressor/expander in a Compressed Air Energy Storage system with consideration of heat transfer and friction,” *Proc. Am. Control Conf.*, pp. 1800–1805, 2012.
- [17] S. Mousavi, S. Kara, and B. Kornfeld, “Energy efficiency of compressed air systems,” *Procedia CIRP*, vol. 15, pp. 313–318, 2014.
- [18] M. W. Coney, P. Stephenson, A. Malmgren, C. Linnemann, and R. E. Morgan, “Development Of A Reciprocating Compressor Using Water Injection To Achieve Quasi-Isothermal Compression,” 2002.

- [19] M. Heidari, S. Lemofouet, and A. Rufer, “On The Strategies Towards Isothermal Gas Compression And Expansion * Corresponding Author 2 . FROM ADIABATIC TO ISOTHERMAL COMPRESSION,” pp. 1–14, 2014.
- [20] M. Heidari and A. Rufer, “Fluid Flow Analysis of a New Finned Piston Reciprocating Compressor Using Pneumatic Analogy,” vol. 2, no. 4, pp. 297–301, 2014.
- [21] J. D. Van de Ven and P. Y. Li, “Liquid piston gas compression,” *Appl. Energy*, vol. 86, no. 10, pp. 2183–2191, 2009.
- [22] C. Zhang, M. Saadat, P. Y. Li, and T. W. Simon, “Heat Transfer in a Long, Thin Tube Section of an Air Compressor: An Empirical Correlation From CFD and a Thermodynamic Modeling,” no. 45233. pp. 1601–1607, 2012.
- [23] N. Arjomand Kermani and M. Rokni, “Heat transfer analysis of liquid piston compressor for hydrogen applications,” *Int. J. Hydrogen Energy*, vol. 40, no. 35, pp. 11522–11529, 2015.
- [24] A. Srivatsa and P. Y. Li, “How moisture content affects the performance of a liquid piston air compressor/expander,” *J. Energy Storage*, vol. 18, no. April, pp. 121–132, 2018.
- [25] C. Zhang *et al.*, “Thermal analysis of a compressor for application to Compressed Air Energy Storage,” *Appl. Therm. Eng.*, vol. 73, no. 2, pp. 1402–1411, 2014.
- [26] K. R. Ramakrishnan, P. I. Ro, and V. C. Patil, “Temperature abatement using hollow spheres in liquid piston compressor for Ocean Compressed Air Energy Storage system,” *Ocean. 2016 MTS/IEEE Monterey, OCE 2016*, no. 2, pp. 1–5, 2016.
- [27] W. Jia and H. H. Qiu, “Experimental investigation of droplet dynamics and heat transfer in spray cooling,” *Exp. Therm. Fluid Sci.*, vol. 27, no. 7, pp. 829–838, 2003.
- [28] R. Sureshkumar, S. R. Kale, and P. L. Dhar, “Heat and mass transfer processes between a

- water spray and ambient air – II . Simulations,” vol. 28, pp. 361–371, 2008.
- [29] R. Sureshkumar, S. R. Kale, and P. L. Dhar, “Heat and mass transfer processes between a water spray and ambient air - I. Experimental data,” *Appl. Therm. Eng.*, vol. 28, no. 5–6, pp. 349–360, 2008.
- [30] W. M. Grissom and F. A. Wierum, “Liquid spray cooling of a heated surface,” *Int. J. Heat Mass Transf.*, vol. 24, no. 2, pp. 261–271, 1981.
- [31] J. Jia, Y. Guo, W. Wang, and S. Zhou, “Modeling and experimental research on spray cooling,” in *Semiconductor Thermal Measurement and Management Symposium, 2008. Semi-Therm 2008. Twenty-fourth Annual IEEE*, 2008, pp. 118–123.
- [32] H. Montazeri, B. Blocken, and J. L. M. Hensen, “Evaporative cooling by water spray systems: CFD simulation, experimental validation and sensitivity analysis,” *Build. Environ.*, vol. 83, pp. 129–141, 2015.
- [33] M. Mutlu and M. Kiliç, “Effects of piston speed, compression ratio and cylinder geometry on system performance of a liquid piston,” *Therm. Sci.*, vol. 2014, no. 6, pp. 1953–1961, 2014.
- [34] U. Lekic, “Fluid flow and heat transfer in a helium gas spring. Computational fluid dynamics and experiments,” 2011.
- [35] X. Luo, J. Wang, M. Dooner, and J. Clarke, “Overview of current development in electrical energy storage technologies and the application potential in power system operation,” *Appl. Energy*, vol. 137, pp. 511–536, 2015.
- [36] ANSYS Fluent Guide.

APPENDIX

Appendix A

In this section, the experimental observations for the 120°, 90°, and 60° spray nozzles are presented apart from the 120° spray angle for 3s compression stroke time which is reported in Chapter 3.

A.1. 120° Spray Angle with 5s compression stroke time

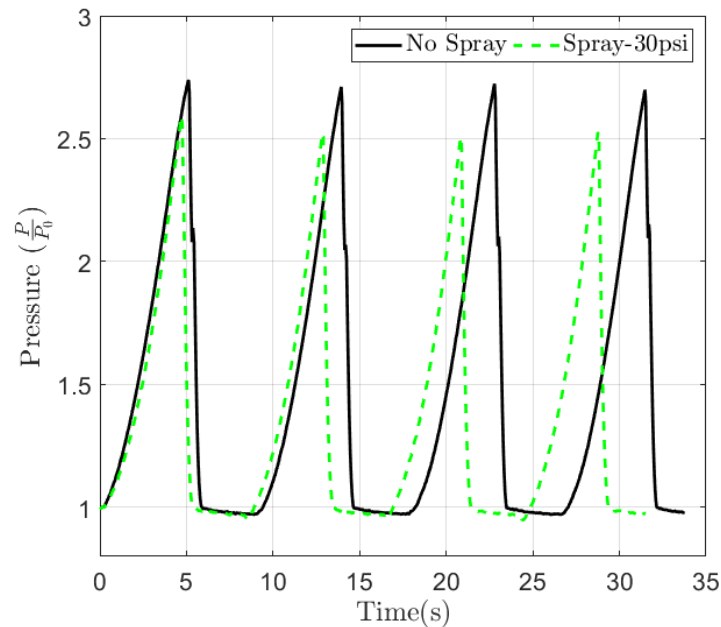


Figure A.1.1: Continuous pressure ratio–time plots with and without spray injection

The pressure-time variation for continuous compression and expansion cycles is shown in figure A.1.1. Instead of plotting all the injection pressure cycles, only the 30 psi injection pressure cycle is shown along with the compression cycle without any spray injection. For the compression cycles with 30 psi injection, the curve shifts compared to the compression cycles without any spray injection. Since, with spray injection, the compression and expansion time is slightly less than the corresponding compression and expansion time without spray injection, the plot shifts over time. The compression time during spray injection is slightly less compared to compression without

spray injection since the pressure and temperature achieved is lower with spray injection. With spray cooling, the time taken to achieve the lower pressure reduces which gradually shifts the curve.

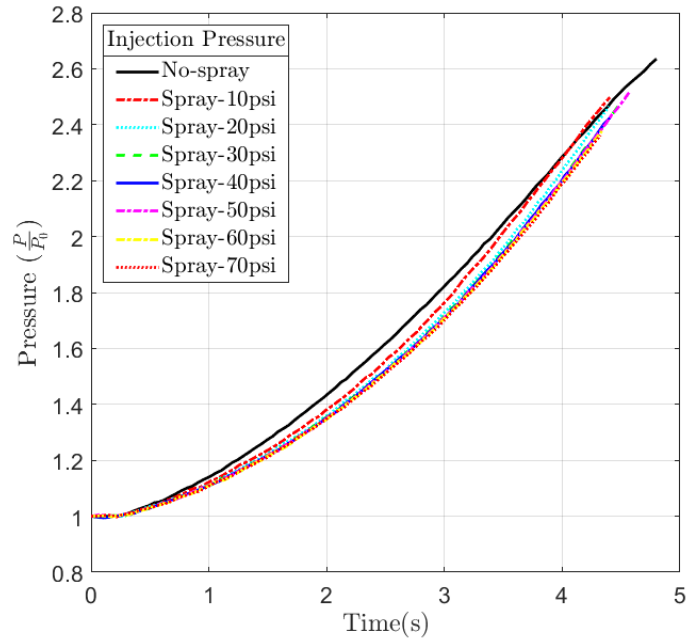


Figure A.1.2: Pressure ratio–time plots for different spray injection pressures for one compression cycle

Figure A.1.2 shows the pressure ratio –time plots for different injection pressure for a single compression cycle. The continuous temperature-time plots with and without any spray injection are shown in figure A.1.3. The temperature with spray injection during the expansion cycles decreases to around 290 K.

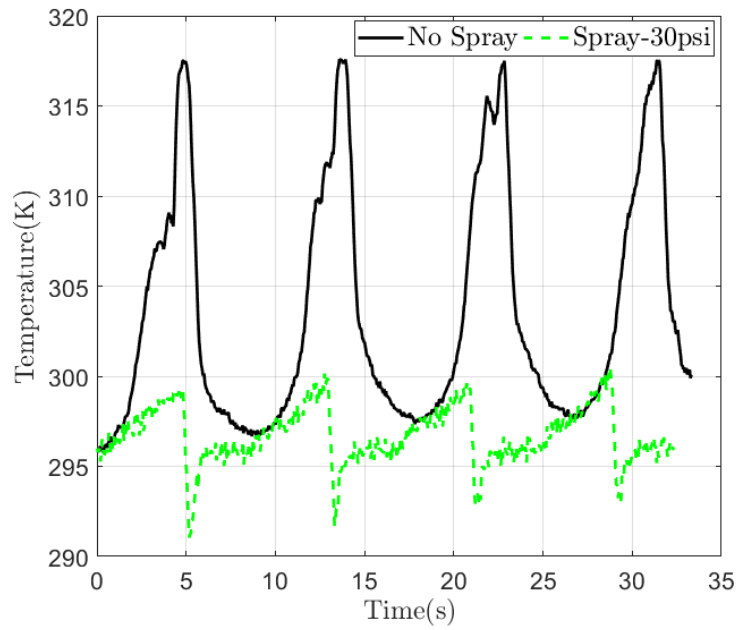


Figure A.1.3: Continuous temperature–time plots with and without spray injection

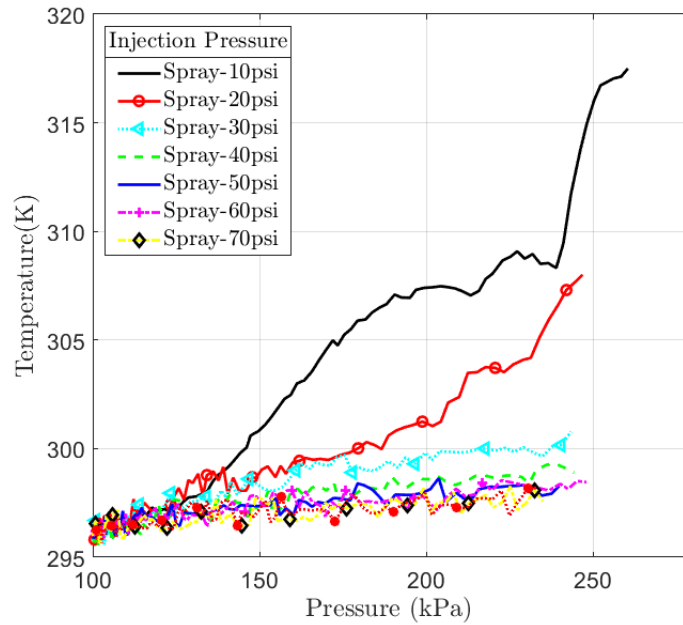


Figure A.1.4: Temperature–pressure plots for different spray injection pressures for one compression cycle

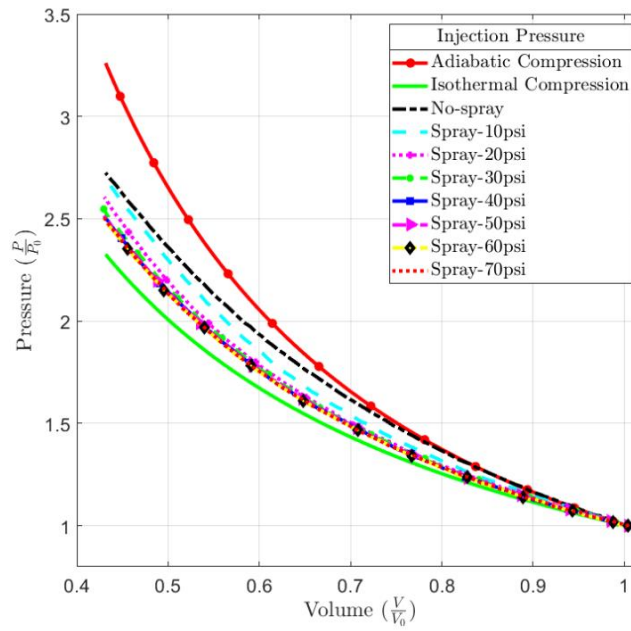


Figure A.1.5 Pressure-volume plots for different spray injection pressures during compression

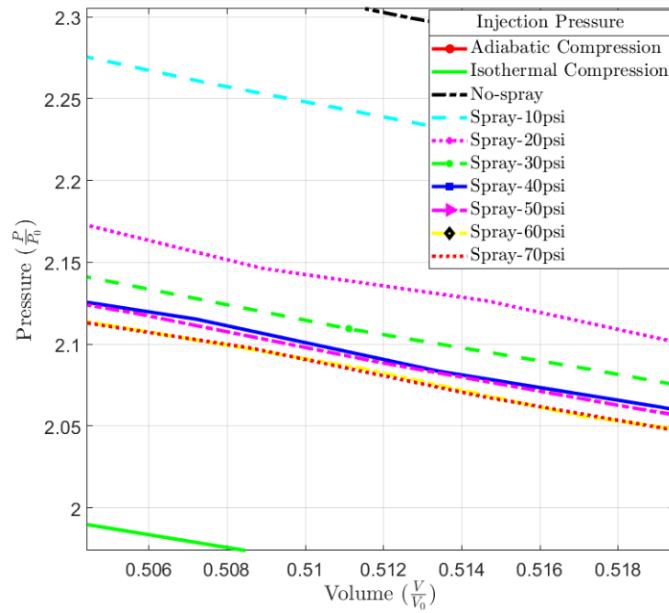


Figure A.1.6: Zoomed view of pressure-volume plots for different spray injection pressures

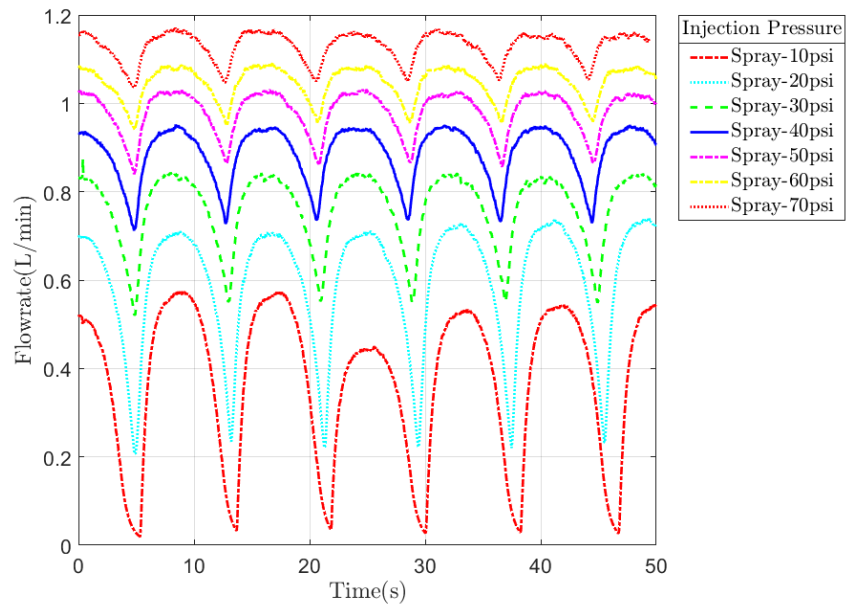


Figure A.1.7: Flow rate from spray nozzle during continuous cycle operation

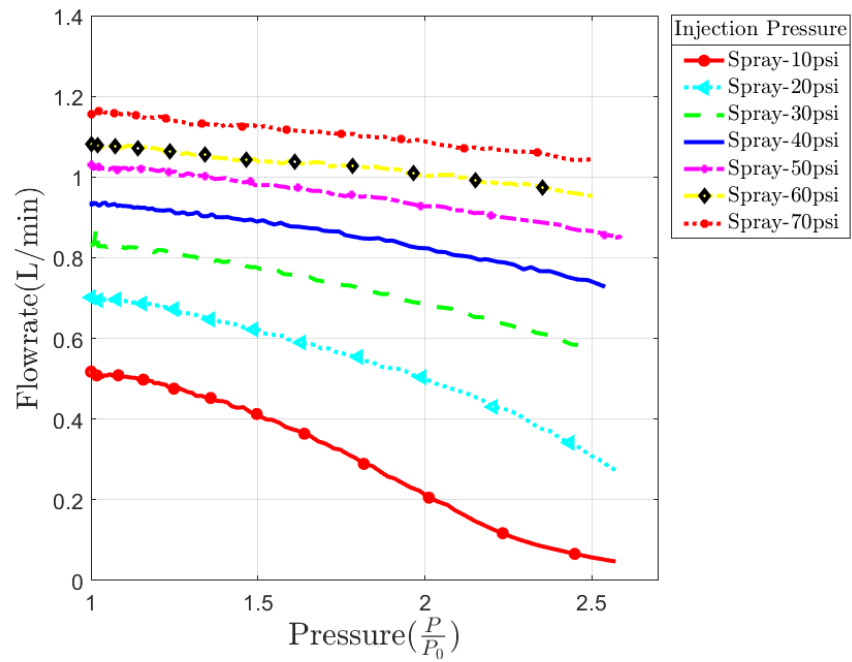


Figure A.1.8: Flowrate of spray water for different injection pressures during compression

A.2 90° Spray Angle with 5s compression stroke time

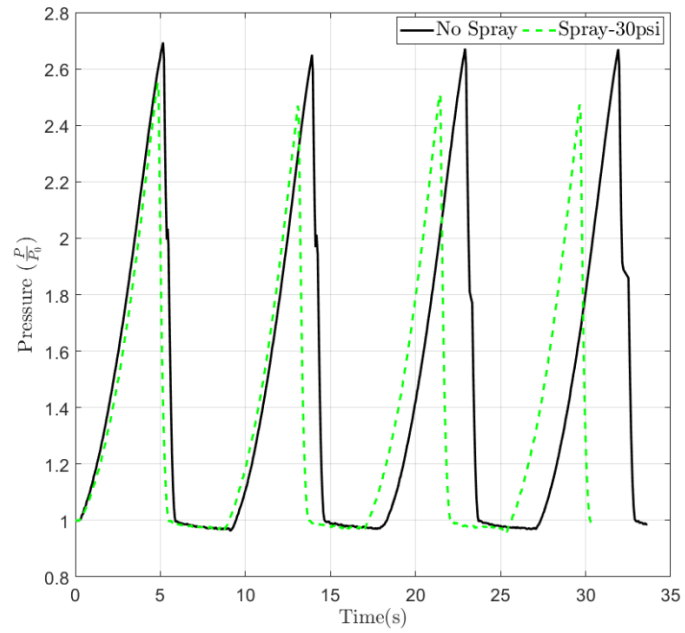


Figure A.2.1: Continuous pressure ratio–time plots with and without spray injection

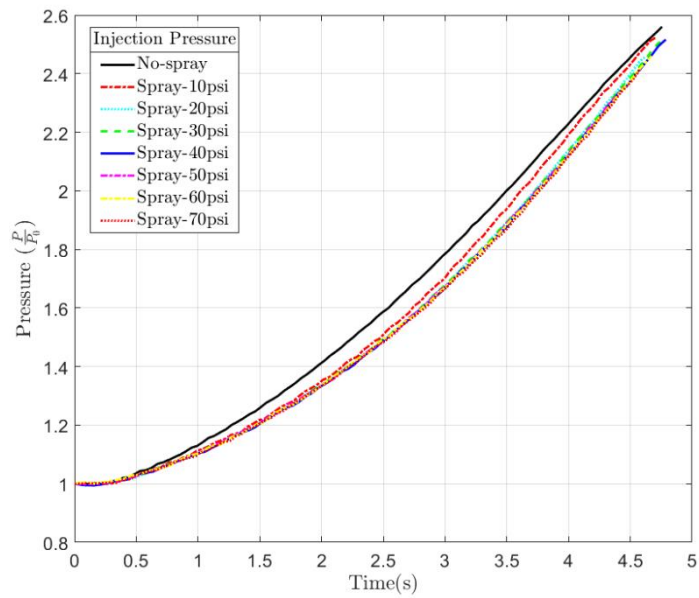


Figure A.2.2: Pressure ratio–time plots for different spray injection pressures for one compression cycle

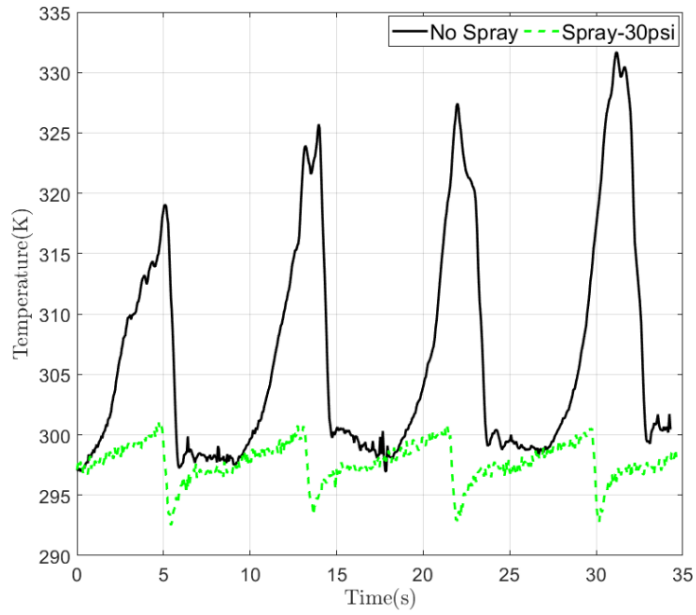


Figure A.2.3: Continuous temperature–time plots with and without spray injection

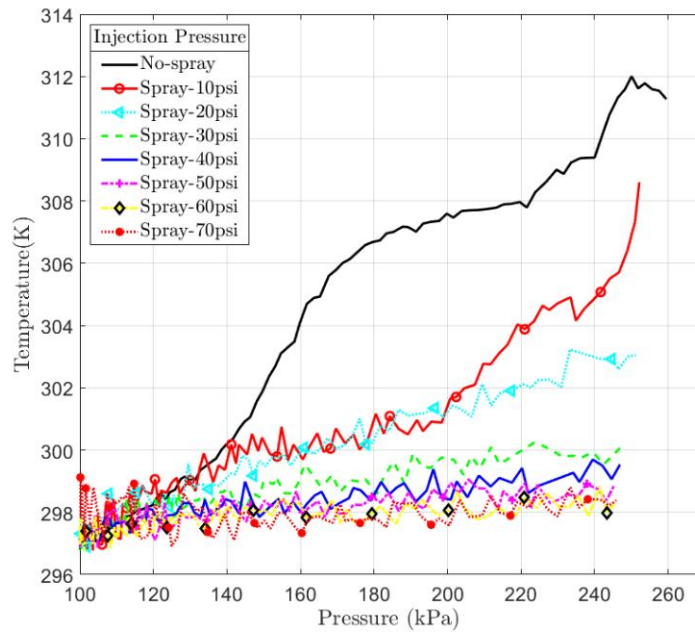


Figure A.2.4: Temperature–pressure plots for different spray injection pressures for one compression cycle

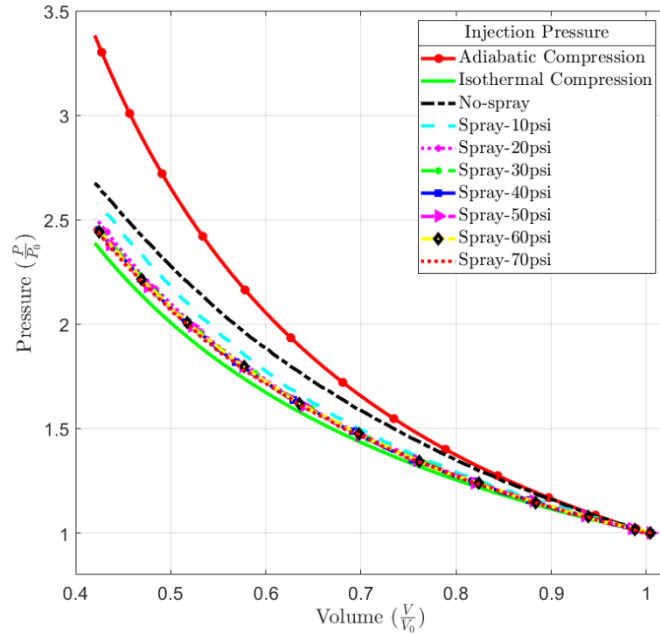


Figure A.2.5 Pressure-volume plots for different spray injection pressures during compression

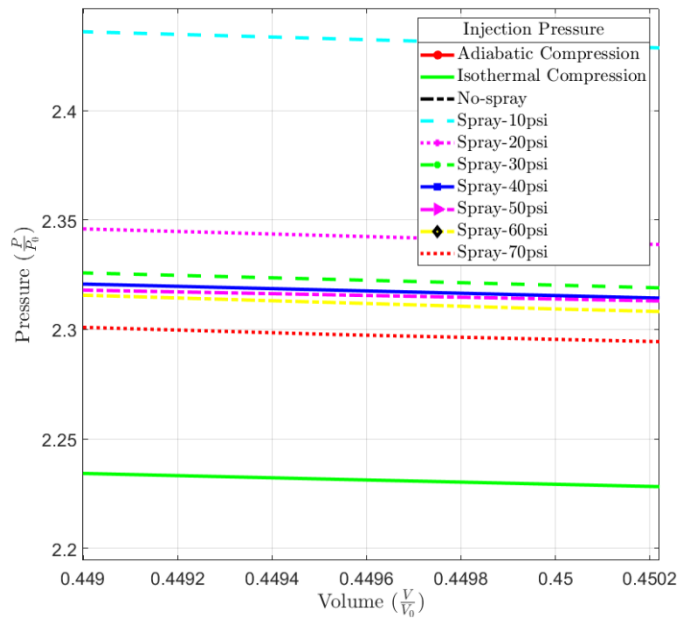


Figure A.2.6: Zoomed view of pressure-volume plots for different spray injection pressures

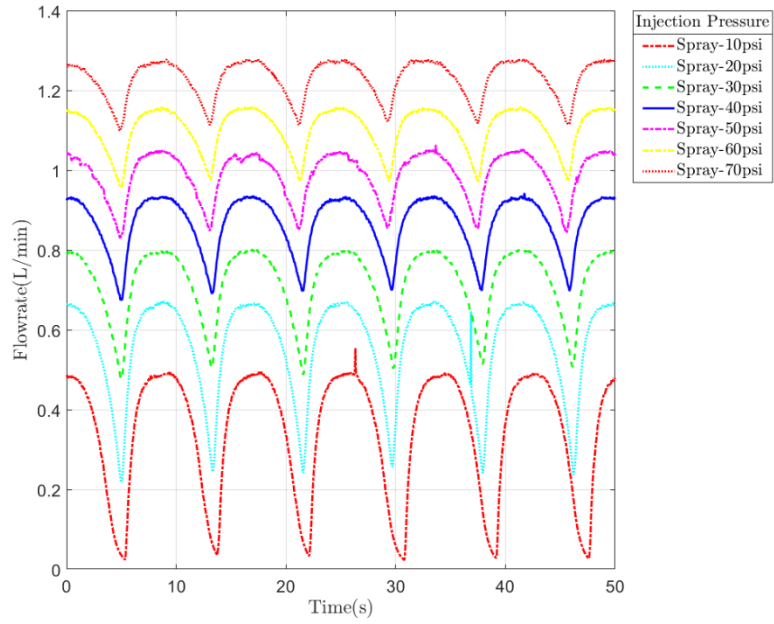


Figure A.2.7: Flow rate from spray nozzle during continuous cycle operation

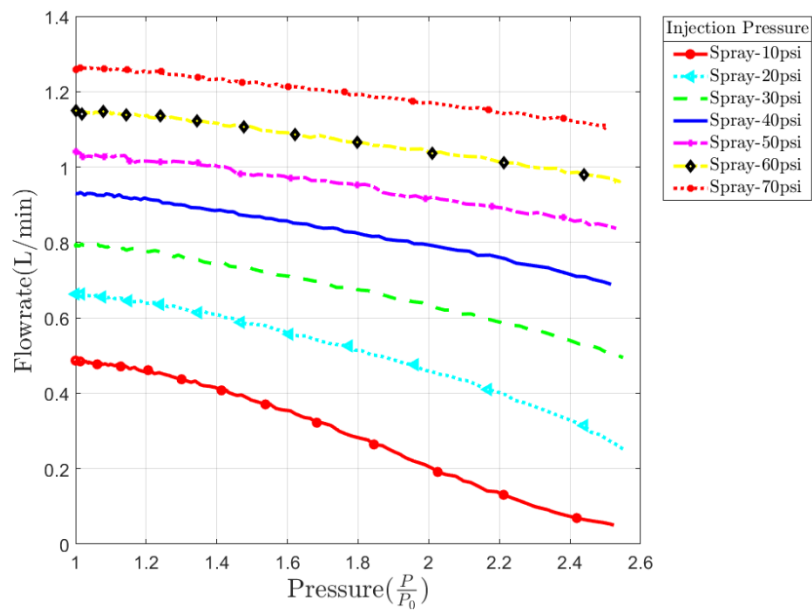


Figure A.2.8: Flowrate of spray water for different injection pressures during compression

A.3 60° Spray Angle with 5s compression stroke time

The 60° spray angle was the first set of experiments performed for investigating the effects of spray injection during the liquid piston compression process. Initially, the injection pressure range varied from 30-70 psi instead of 10-70 psi. To understand the effect of back-pressure generated due to the increase in the chamber air pressure, for the 90° and 120° spray nozzles, 10 psi and 20 psi injection pressure were also studied.

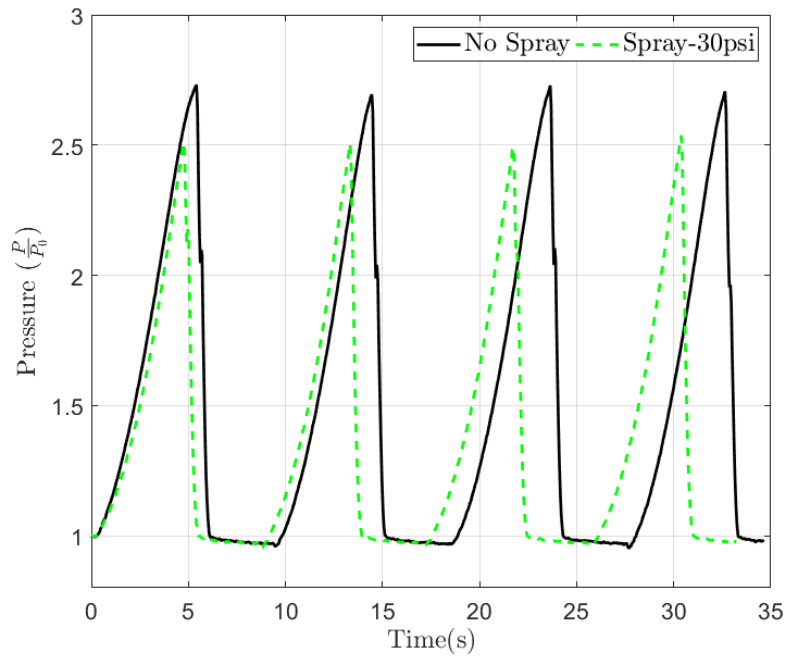


Figure A.3.1: Continuous pressure ratio–time plots with and without spray injection

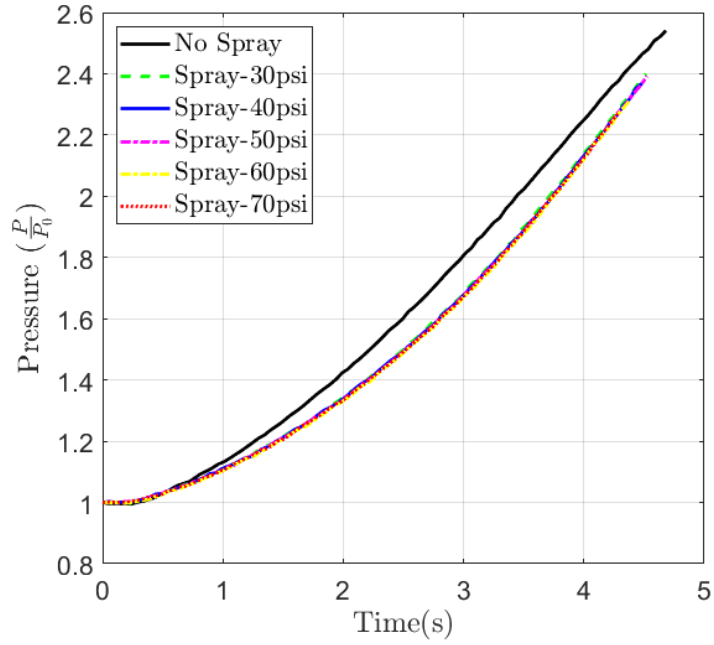


Figure A.3.2: Pressure ratio–time plots for different spray injection pressures for one compression cycle

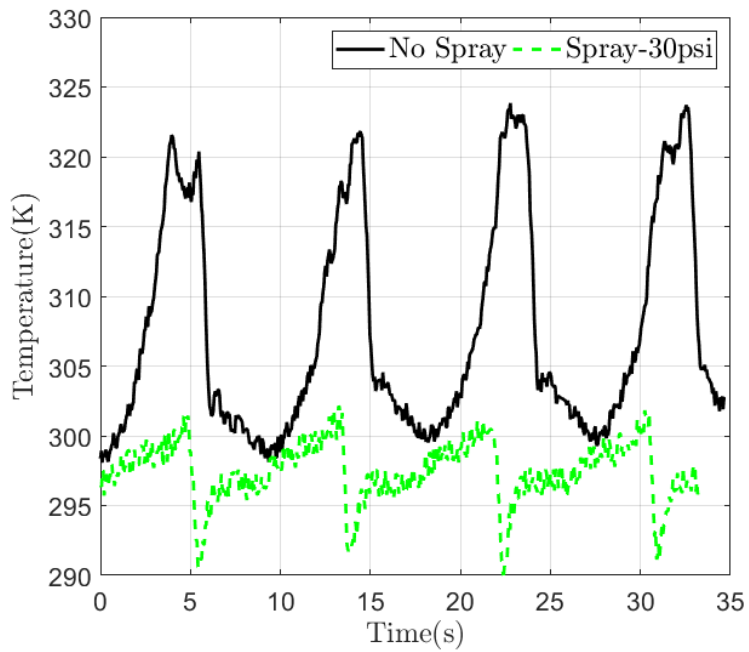


Figure A.3.3: Continuous temperature–time plots with and without spray injection

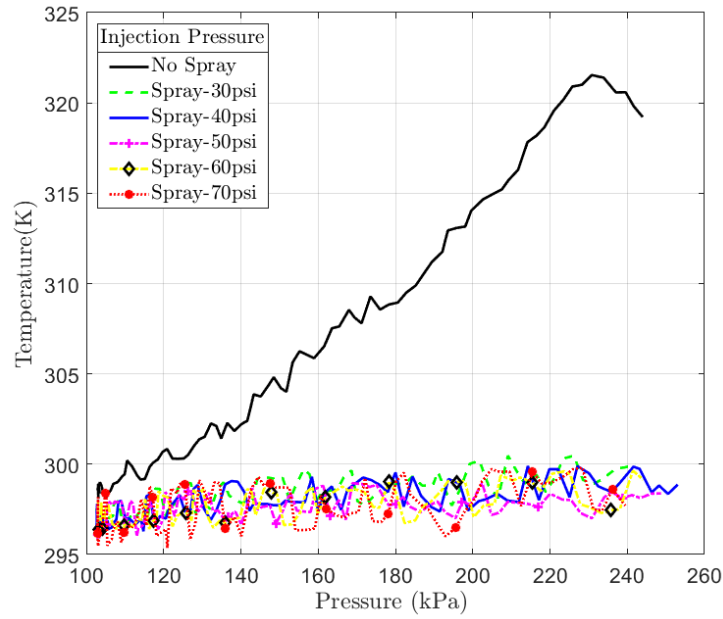


Figure A.3.4: Temperature–pressure plots for different spray injection pressures for one compression cycle

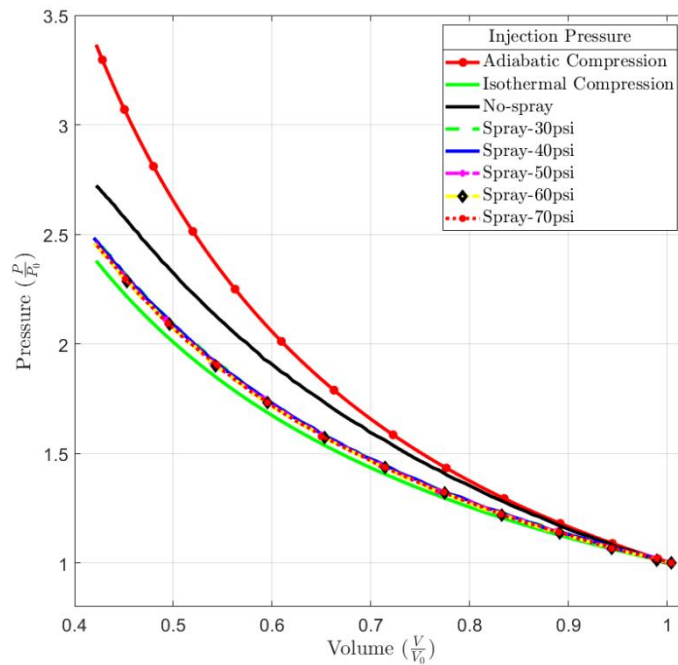


Figure A.3.5 Pressure-volume plots for different spray injection pressures during compression

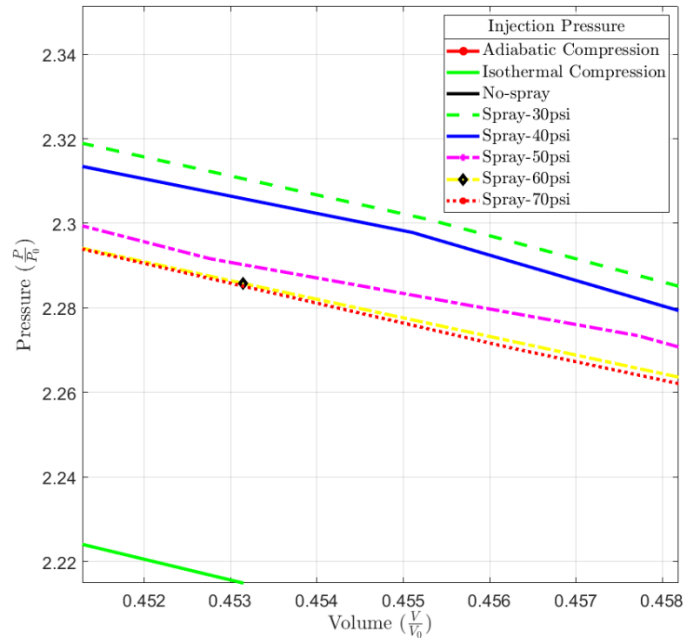


Figure A.3.6: Zoomed view of pressure-volume plots for different spray injection pressures

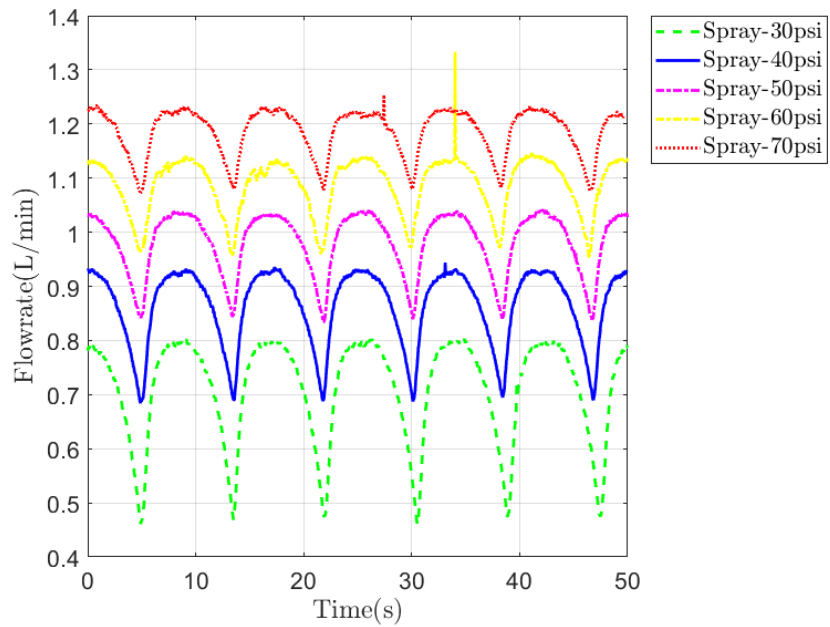


Figure A.3.7: Flow rate from spray nozzle during continuous cycle operation

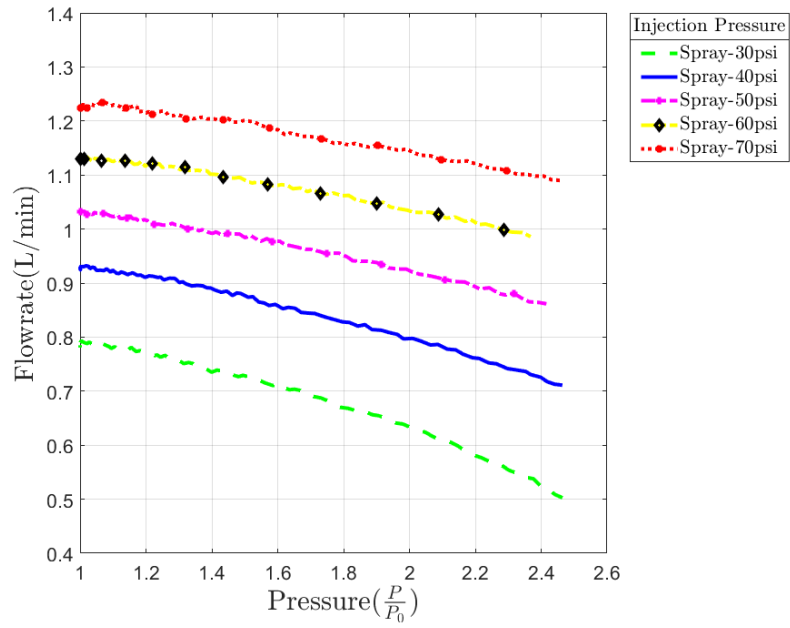


Figure A.3.8: Flowrate of spray water for different injection pressures during compression